Resonant double core-hole spectroscopy of ultrafast decay dynamics in Fe complexes

Dissertation zur Erlangung des Doktorgrades
an der Fakultät für Mathematik, Informatik und Naturwissenschaften
Fachbereich Physik
der Universität Hamburg

vorgelegt von
Julius Christoph Schwarz

Hamburg
2024

Resonant double core-hole spectroscopy of ultrafast decay dynamics in Fe complexes

Abstract

Resonant double core-hole (DCH) spectroscopy allows observation of ultrafast dynamic processes in small $3d$-metal compounds in the gas phase. Using the intense X-Ray pulses of the European XFEL, electron and ion spectroscopy was used to reveal the signature of iron $2p^2$ resonant DCH excitation in iron pentacarbonyl and ferrocene. Comparing the experimental results to theoretical calculations reconstructs single core-hole (SCH) and DCH photon-matter interactions in the two targets. The DCH Auger-Meitner electron signals offer insight into the electron dynamics during the core-hole lifetime and their dependence on the chemical environment. The product ions show evidence for DCH processes in multiply charged iron cations.

Zusammenfassung

Resonante Doppel-Kern-Loch Spektroskopie erlaubt das Beobachten von dynamischen Prozessen im einstelligen Femtosekundenbereich. Mit Hilfe von Röntgenpulsen des European XFELs wurde diese Technik an kleinen $3d$-Metalkomplexen angewandt, um die $2p^2$ resonante Doppel-Kern-Loch Anregungssignatur in Eisenpentakarbonyl und Ferrocen zu messen. Der Vergleich der experimentellen Resultate mit den Ergebnissen von Cowan-Code Rechnungen für isolierte Eisenatome ermöglicht die Rekonstruktion von Ein-Kern-Loch- und Zwei-Kern-Loch Interaktionen in beiden Proben. Die Spektren der Produktionen zeigen Spuren von Doppel-Kern-Loch Prozessen in höher geladenen Eisenkationen. Das Zwei-Kern-Loch Auger-Meitner Elektronensignal ermöglicht zusätzlich einen Einblick in die Elektronendynamiken während der Lebensdauer des Kernlochs.

Contents

1 Introduction

Chemical reactions are the basis for all life. They are the driving force behind any process in living organisms, such as the oxygen transport and oxidation reactions (which are, microscopically, an electron transfer) that keep humans alive while they breathe. Chemical reactions are dynamic processes that occur on many different natural time scales, most of them faster than what can be perceived by the human eye. Understanding chemical reactions in detail promises control and the ability to innovate improvements for nearly every aspect of life. However, such understanding requires precise knowledge of the exact state of all reactants involved at any given point in time. Therein lies the crux of these studies, as even the slowest chemical reactions are usually started (and influenced significantly) by charge processes within the reactants, which occur on very short natural time scales.

Access to these ultrafast timescales is of utmost importance in the study of chemical reactions. For example, the timescale associated with cationic processes in such reactions can occur on natural timescales of 100 fs and electron transfer can occur even faster on a time scale in the attosecond regime, up to 10 fs, as discussed by Kraus et al. on some of the major achievements in the study of nuclear and electronic dynamics with X-Ray pulses produced by high-harmonic, free-electron-laser (FEL) and synchrotron sources [46]. For the relaxation processes, such as photo fluorescence and direct- or shake-off- ionization, which follow molecular excitation, time scales can be even shorter than this. Among the relaxation processes involving the electronic system of an excited molecule, the subsequent Auger-Meitner process, which is of particular importance in core-excited molecules, is similarly short. The estimated time scale for this process is given as 3 fs to 8 fs by Piancastelli [73]. Access to these timescales is an enormous experimental challenge, that has previously led to some groundbreaking science in the field of chemistry and physics:

First results in this field of study were reported by Ahmed Zewail and resulted in the formation of the field of femtochemistry. In his Nobel Lecture, he reinforced the strive for the study of phenomena on ever shorter timescales [103]. This work usually requires a combination of short X-Ray pulses and precise X-Ray wavelengths in order to resolve the investigated phenomena in time and prepare as well as probe the electronic system of the sample. Such conditions are provided by large-scale facilities, such as synchrotrons or free-electron lasers, enabling photon-matter interactions using short X-Ray pulses of low bandwidth. Spectroscopy methods detect the resulting fragment particles, cations and electrons, of such an experiment and draw conclusions about the sample. Core-hole spectroscopy uses the advantage of X-Ray photon sources with low bandwidth and controllable wavelength: their element- and orbit- specificity. This serves to probe sub-valence core electrons at a specific atomic site of a molecule. The excited state created in such an X-Ray photon-matter interaction can relax via the Auger-Meitner process, emitting one or multiple Auger-Meitner electrons in the process. A second photon interacting with the molecule after a well defined time in a "pump-probe" experiment can probe the relaxation processes following the excitation. At large-scale facilities, such as synchrotrons or free-electron lasers, this kind of study on ionic processes and charge migration has previously yielded promising results, as can be seen in Ueda's work on X-Ray free-electron lasers [93] and the references found within and in the corresponding special issue of the same name. Accessing the lifetime of an Auger-Meitner state, however, is chal-

lenging, even for femtochemistry experiments. One avenue to resolve such short timescales on the order of a few femtoseconds was pioneered by Pierre Agostini, Ferenc Krausz and Anne L'Huillier, moving away from the use of large-scale facilities. This approach favors the use of ultrashort lasers for the study of attosecond processes instead. Krausz [47] heralded this as the coming of the era of attosecond physics. Pierre Agostini, Ferenc Krausz and Anne L'Huillier's individual work was awarded with the Nobel prize in 2023, a little over two decades after Ahmed Zewail received it.

At large-scale facilities and with the advent of the new generation of X-Ray free-electron lasers, another avenue to access processes that occur on the lifetime of the Auger-Meitner decay can be used; Double core-hole (DCH) spectroscopy. Similarly to single core-hole (SCH) spectroscopy, the starting point of a DCH experiment is a photon with a specific wavelength interacting with a sub-valence electron of an atom or molecule, creating an excited state. If, however, a second photon excited a core electron in the already excited molecule before the completion of the subsequent relaxation via the Auger-Meitner process, a double core-hole state is created. These states were first predicted by Cederbaum et al. [17]. This process probes the molecular dynamics on a timescale that, while not as well defined as conventional pump-probe experiments, has an upper limit of the Auger-Meitner lifetime, as is made clear in the work of Fang et al. [28] on the creation of double K-shell holes in N_2 molecules. Spectroscopy can be conducted in various ways on double core-hole states, chief among them photoelectron-spectroscopy as well as Auger-Meitner electron spectroscopy, with some studies also conducting spectroscopy on the fragment ions of molecules in a DCH states. Double core-hole spectroscopy has become a valuable technique to study ultrashort processes, with resources being dedicated to the techniques' improvement and use by major large-scale facilities. This was made clear by Young et al. [102] in their roadmap for ultrafast X-Ray atomic and molecular physics.

For an adequate signal-to-noise ratio, the DCH spectroscopy technique is entirely dependent on a sufficient number of double core-hole excitations in the sample. The cross-section of a secondary photon-matter interaction in an already core-hole excited target decreases significantly, requiring particularly short photon pulses with a high number of photons per pulse to be used for DCH spectroscopy. An often-chosen site in DCH spectrosocopy investigation of atoms and molecules is the K-shell. The advantages of this site are its low electron count, which eases the detection of photoelectrons, as well as the close proximity to the core, which provides information both, if the two core-holes are located on the same atomic site within the molecule and if the two sites are created on different atomic sites. L-shell DCH spectroscopy has been previously conducted with synchrotron radiation on S containing molecules by Linusson et al. [52]. As far as known at the time of this work, L-shell DCH spectroscopy has not been conducted on Fe containing molecules so far, nor have results of L-shell DCH spectroscopy using the radiation from X-Ray free-electron lasers been published. As the possibility to conduct two-photon absorption DCH spectroscopy at FEL facilities has only become more available in the last decade, with experiment ambitions scaling with the increase in photon pulse energy provided, this lack off previously published results is not surprising. Nevertheless, L-shell DCH spectroscopy offers not only a new sub-valence region of electron dynamics to study, but can also help in studying more complex molecules. Over the course of this work, this is shown by conducting L-shell DCH spectroscopy on the $3d$ metal complexes

iron pentacarbonyl and ferrocene.

$3d$ metal complexes play important roles in biological processes, such as iron in the Heme molecule and manganese in several proteins (see *Bioinorganic Chemistry* for more information [39]). The $3d$ metal complexes, as a step towards more complex molecules, are of great interest for understanding oxygen transport and electron transfer (i.e., oxidation–reduction) reactions. The $3d$ metals are of such high relevance as they can exist in various oxidation states. This enables the metal centres to store and exchange charge with the chemical environment by changing their oxidation state without detrimental radical formation. This has been previously investigated by Kubin et al. [48] in their work on the oxidation states of transition metal complexes. Ferrocene and iron pentacarbonyl serve as model systems for these processes. Their different molecular geometries, one spherical, one cylindrical, as well as their chemical environment of the metal center differing by the oxygen ligands, implies both to relax differently after interaction with an X-Ray pulse targeting their metal center.

The two molecules also represent a significant increase in complexity and size over some of the previous targets for DCH spectroscopy, such as Mazza et al.'s work on Ne [60] or the above mentioned N_2 [28], and are comparable to the studies conducted on 4-aminophenol by Zhaunerchyk et al. [105]. This increase in size and complexity demands a well-founded choice in what aspects of the photon-matter interaction are considered during the experiments.

The approach chosen in this thesis to illuminate the DCH timescales in $3d$ metal complexes involves studying the results of such high pulse energy interactions on the cation products of the interaction. In detecting the various cationic fragments that are produced in such a high-energy interaction and the molecular relaxation processes following it, differences in the molecule's response to the photon pulse can be discovered. Additionally, knowledge of the fragmentation behavior at high pulse energies provides information on the makeup of the interaction zone during the photon-matter interaction. This can be used in the study of the electron products of the interaction to differentiate between contributions of SCH states and DCH states.

In studying the product electrons from DCH states of ferrocene and iron pentacarbonyl, produced by a photon-matter interaction of the samples with intense X-Ray pulses, differentiation between photoelectrons and Auger-Meitner electrons can be made. Photoelectrons are immediately excited in the interaction and coincidence studies were previously able to identify both emitted electrons from a two-photon absorption. For example, the work of Mucke et al. [68] uses covariance mapping to reveal two-photon double core-hole states in C_2H_2 and C_2H_6.

In this work, particular focus will be given to the identification of the Auger-Meitner electrons, which are emitted in the relaxation processes following the double core-hole excitation. They represent access to the metal centers relaxation and electron dynamics upon the two-photon ionization. Information on the relaxation processes in $3d$ metal complexes on such small timescales is of high interest for a precise understanding of the molecules special role in some of the most important biochemical reactions occurring in the human body.

2 Basics of Photon-Matter Interaction

In this section, the underlying processes following the interaction of X-Rays with atoms or molecules which are relevant for this thesis are described. An introduction to these topics will be given along the lines of previous theses on similar topics (see [65, 72] and state of the art publications. Along with these details, the fundamentals of measurement techniques used in this thesis will be explained. Ultimately, this section will provide the groundwork for the detailed analysis of the experiments conducted in this thesis.

2.1 Core-Hole Ionization Processes following X-Ray-matter Interaction

In this thesis, the processes in ionized states induced by the absorption of X-Rays are investigated. The physical processes following such a photon-matter interaction are described here, namely single core-ionization, double core-ionization and the consequent relaxation processes such as the Auger-Meitner effect and radiative decay. Note that this thesis employs the definition of a core-hole to encompass not merely the *K*-shell electrons of any given target atom or molecule, but also the *L*-shell electrons of targets involving atoms of sufficiently high nuclear charge number *Z* as potential sites to create core-holes.

2.1.1 Single Core-Hole Ionization and Single Core-Hole Resonant Excitation
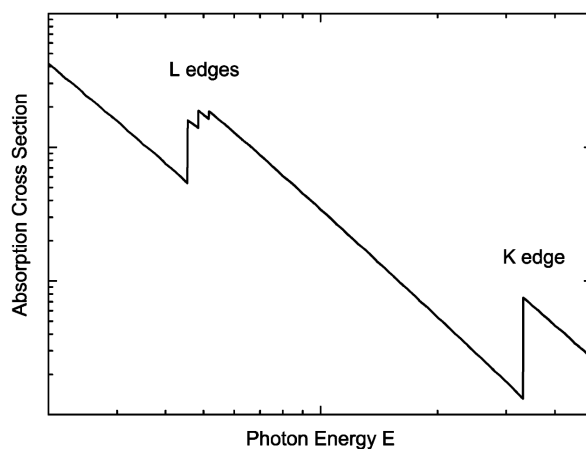
Figure 1: An illustration of the variation in linear absorption coefficient as a function of incident photon energy. Core edges for *L*- and *K*-shells depend on the target. Figure adapted from [14].

Upon spatial overlap of an X-Ray photon with a target molecule or atom, there exists an absorption cross-section specific to the target which governs the likelihood of X-Ray absorption for the combination of occupied orbitals within the target and fixed photon energy of the X-Ray photon. FIG. 1 shows the principal features of the atomic absorption cross-section: Firstly, a decreasing trend prevails for the absorption cross-section with increasing incident

photon energy. Secondly, a sharp rise in absorption at discrete photon energies marks edges in the cross-section. These absorption edges are unique to a target and occur near the ionization of a core shell electron. They contain spectral features for transitions between the core electron and the continuum or the core electron and an unoccupied valence orbital or Rydberg state. For more information, see *Ultrafast X-ray Absorption Spectroscopy* by Bressler and Chergui [14].

SCH ionization occurs whenever a molecule is irradiated with an X-Ray photon of a fixed energy above the molecules' ionization potential of a core-hole electron on one of the edges shown in FIG. 1. The transferred energy causes the electron to be removed from the molecule, splitting it into a photoelectron and the remaining cation. In general, a higher initial energy of the X-Ray photon allows the ionization of deeper and more tightly bound electrons. Energy exceeding the binding energy of the electron is conserved as kinetic energy after removal from the atom or molecule. The signifier 'core-hole'-ionization implies such a high-energy, sub-valence process.
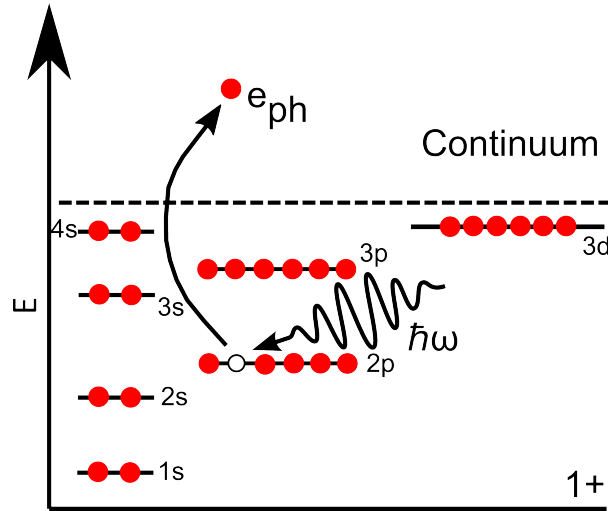
Figure 2: A schematic of a single photon excitation. The Fe $2p$ site was chosen for this example. Following the interaction of a Fe $2p$ electron with an X-Ray photon $\frac{\hbar c}{\lambda}$ of suitable wavelength, the electron is emitted as a photoelectron. This figure and all subsequent illustrations of this type depict electrons sorted by their angular quantum number as a guide for the eye.

FIG. 2 illustrates this ionization process for the Fe atom. Formally, one can write this X-Ray - matter interaction as:

$$Fe + \hbar\omega \longrightarrow [\text{Fe}(L^{-1})]^+ + e_{ph} \tag{1}$$

In this equation, the $[\text{Fe}(L^{-1})]^+$ expression denotes an SCH state, while e_{ph} signifies the photoelectron. For an X-Ray-matter interaction with low photon flux, SCH ionization, as the most likely process, is going to dominate the product fragment signal. Given a sufficient number of targets in the interaction region, ionization rate depends linearly on the X-Ray pulse intensity.

Another possible process, that is akin to this ionization interaction, is a resonant excitation. Resonant excitation implies the electron not leaving the atom or molecule, but occupying a higher molecular or atomic orbital or a Rydberg state. As a consequence, no photoelectron is emitted into the continuum to be detected. The resonantly excited molecule relaxes however, which leads to photon emission, or the emission of an Auger-Meitner electron.

2.1.2 Auger-Meitner Effect and Radiative Decay

Figure 3: A schematic of an Auger-Meitner effect. The previously created $2p$ hole (FIG. 2) in the Fe atom is occupied by an electron in a higher orbital. Excess energy is emitted in an Auger-Meitner electron. The Auger-Meitner effect is autoionizing.

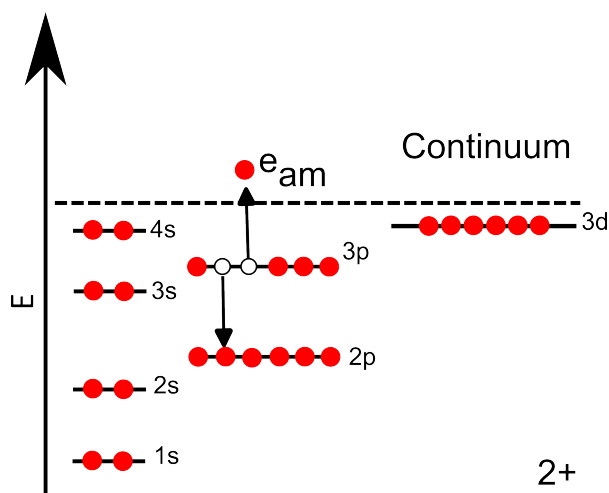Upon ionization or excitation of an atom or molecule, relaxation processes occur in the cation or excited state. The core-hole enforces a rearrangement in the entire electronic configuration of the target atom or molecule. The electronic orbitals tighten around the perceived additional positive charge due to the decrease in charge screening introduced by the core-hole. The principal relaxation pathway in most cases, for such a scenario, is the Auger-Meitner effect, which was independently discovered by Auger, Meitner and Robinson in the 1920s (see [5, 64, 74]).

In this process, energy exceeding the binding energy is transferred from an electron in an atomic or molecular orbital of higher energy than the previously created hole state to an Auger-Meitner electron via a Coulomb interaction. The Auger-Meitner electron is consequently emitted and enters the continuum, while the remaining partner electron in the process fills the previously unoccupied hole. The Auger-Meitner effect is always a self-ionizing process. An Auger-Meitner electron's energy is determined by the emitting electron's energy in relation to the hole state and not by the photon energy of the photon that originally created the hole state via ionization or excitation. This is of high relevance for this work. FIG. 3 illustrates the Auger-Meitner decay in the previous example of an Fe SCH state at the $2p$ site. Note the similarity between the emitted energy vector and the energy difference in orbitals in this illustration. Returning to Eq. 1, the Auger-Meitner effect in this scenario could be written as:

$$[Fe(L^{-1}M^{14})]^+ \longrightarrow [Fe(M^{12})]^{++} + e_A \qquad (2)$$

Eq. 2 implies the energy of the Auger-Meitner electron as a difference of the SCH state energy and the final energy of the $[Fe(M^{12})]^{++}$ state. This is true, as long as other energy loss effects in the atomic or molecular environment as well as lifetime broadening are ignored. It is important to note that successive filling of hole states created by the Auger-Meitner effect with more relaxation processes can occur following the initial ionization and that it is not uncommon to encounter Auger-Meitner cascades following an initial ionizing X-Ray pulse. Such a cascade ends only when the energy of the Auger-Meitner state at $N-1$ electrons is larger than that of the N state, as no more relaxation pathways remain.

The timescales of the Auger-Meitner effect is intrinsically coupled to the lifetime of the hole. In atoms and molecules, such lifetimes are typically on the order of a few femtoseconds. In their work on DCH spectroscopy in molecules at the K-shell, Piancastelli [73] estimates the lifetime of the molecular Auger-Meitner state before the core-hole decay to be on the order of approximately 4 fs to 8 fs. Approximations for the lifetime of the Fe atomic Auger-Meitner state, stemming from the Cowan code calculations that will be discussed in the next chapter, yield a lower limit of 0.29 fs to an upper limit of 2.1 fs.

A special, ultrafast, case of the Auger-Meitner effect occurs when the hole created by an ionization process is filled by an electron from a subshell of the same main shell. Named after the scientists who reported such a transition in 1935, such a process is called a Coster-Kronig transition [19]. If the emitted electron also occupies the same shell, the resulting Super-Coster-Kronig (SCK) transition counts among the fastest relaxation processes. For iron, Nyholm et al. investigated the effect of Coster-Kronig and Super-Coster-Kronig on the $2p$ and $3p$ Auger-Meitner widths and reported a broadening of the $3p_{1/2}$ levels, due to an $M_2M_3M_{45}$ SCK transition channel [71].

Another relaxation pathway that needs to be mentioned here for completeness sake is radiative decay. Radiative decay processes emit the energy difference of the higher energetic state and the lower energetic state as a photon with corresponding wavelength. The energy of the emitted photon, just as the energy of the Auger-Meitner electron, does not depend on the photon energy of the initial ionizing X-Ray pulse, but mainly on the energy difference of the hole state and the final state. Due to the manner of experiments conducted and the samples investigated, radiative decay will not play a major role in this thesis. This is due to the insignificant fluorescence yield of core-hole states in relatively "light" atoms such as iron [9, 63]. Further details on this relaxation process can be found in other theses on similar subjects (see [72]).

2.1.3 Multi-Photon Processes

In a photon-matter interaction with high irradiance, in which a large number of photons in the ionizing X-Ray pulse are present in the interaction zone during a short time-frame, more than one photon can be absorbed. This absorption can occur both simultaneous in direct multi-photon absorption, or sequentially over a period of time in sequential multi-photon processes [89]. Both multiple ionization, as well as multiple excitation are possible. In sequential photo-ionization, the molecule or atom, including the still present SCH state, serves as target for a

second ionization process, generating a higher charge state in the process. In a direct multi-photon ionization, multiple photons are absorbed simultaneously and higher charge states are generated.

Multi-photon proccesses were investigated as early as the 1920's, with Dirac publishing some of the theoretical groundwork in his works on quantum theory (see [23–25] and the citations contained therein for details). Bonch-Bruevich and Khodovoi later published a review of the main ideas of multi-photon processes [12]. Gerken et al. [31] showed in their work on multi-photon ionization of Xe atoms that according to the general power law of low-order perturbation theory, one can write the rate of simultaneous n-photon processes as:

$$\dot{N}^{(n)} = N_0 \sigma^n \left(\frac{E}{\hbar\omega} \right)^n = N_0 \sigma^n \left(\frac{H}{\tau\hbar\omega} \right)^n \tag{3}$$

In this equation, N_0 denotes the number of targets within the interaction volume, $\sigma^{(n)}$ the respective generalized n-photon ionization cross-section, $\hbar\omega$ the photon energy, H the radiant exposure and $E = \frac{H}{\tau}$ the peak irradiance. Eq. 3 shows that simultaneous mutiphoton processes rise with shorter pulse duration τ, as well as larger radiant exposure H and consequently also with larger peak irradiance E. Furthermore, the relation between the rate of simultaneous multi-photon processes and these quantities is of a non-linear nature. A two-photon process, for example, would follow a quadratic relation. Gerken et al. further contrasted sequential multi-photon processes to this phenomenon, as sequential multi-photon ionization does not explicitly depend on the pulse duration in cases where relaxation processes do not play a significant role [31].

In photon-matter interactions, single and multi-photon absorption are competing processes. Pulse duration and pulse intensity are primary points of reference to gauge the ionization rate according to both processes. Generally, interactions below a certain pulse intensity and above a certain pulse duration are firmly within the 'linear' regime, implying single photon processes to be the predominant source of ionizations.

2.1.4 Double Core-Hole Ionization and Resonant Double Core-Hole Excitation

Double core-hole ionization is a special case of multi-photon processes, in which two core-holes are created within the same target atom or molecule. Santra et al. [79] illustrate the process rather intuitively: Assume a photon-matter interaction in which the X-Ray photon energy is chosen to be much higher than the SCH ionization threshold. Assume further that during any given X-Ray pulse the molecule does absorb an X-Ray photon and an SCH state is formed. With an intensity in the 'non-linear' regime, meaning high enough, a second X-Ray photon may be absorbed before the end of the X-Ray pulse. If the pulse duration τ is short in comparison to the decay life time of the SCH state, then the absorption of a second photon by the SCH state prepared by the first photon becomes ever more likely.

DCH states were first predicted by the work of Cederbaum et al. [17] on double vacancies in the core. They also predicted that the specific energy and site within the target molecule of the first core-hole would, to a large part, determine the energy required to create a second one. In a molecule, double core-holes can be created either on the same site (the same atom and orbital), or on two differing sites (different atoms and/or orbitals). In the context of this

work, only single site double core-holes are considered. Similarly, there are two ways to produce and investigate these states, primarily determined by the photon density provided by the large scale facility in use. In Piancastelli's [73] work on double core-holes in the K-shell, differentiation is made between synchrotron facilities, which study double core-hole creation due to single photon absorption and electron-electron interaction in a shakeoff process or knockoff collision, and X-Ray free-electron laser facilities, which use the high intensity of their X-Ray pulses to create double core-holes via multi-photon absorption. In the context of this work, double core-holes from sequential two photon absorption were studied.
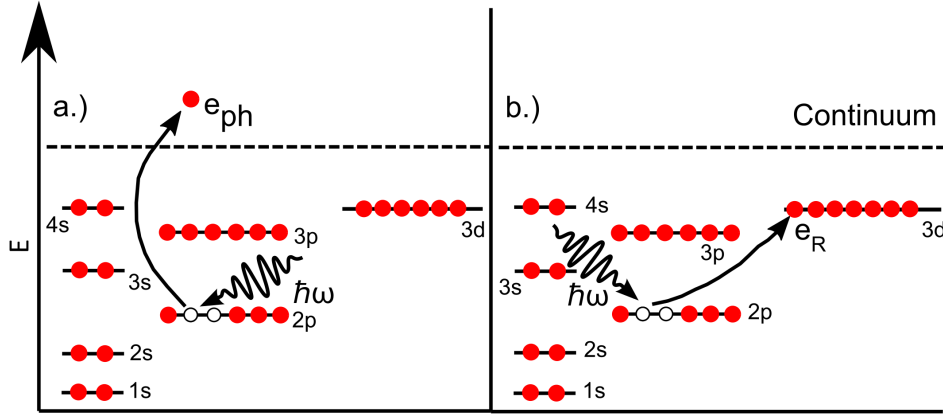

Figure 4: A schematic of a DCH ionization in a.) and a resonant DCH excitation in b.). The Fe $2p^2$ site was chosen for this example. Following the ionization of a first Fe $2p$ electron, a second X-Ray photon $\hbar\omega$ of suitable wavelength interacts with the remaining $2p$ electron and the second electron is also emitted as a photoelectron in a.). In b.), the electron is excited to an unoccupied orbital, or a Rydberg state. Both of these two interactions are limited to occur within the lifetime of the $2p$ core-hole.

The emphasis on the pulse energy and the pulse duration in the description by Santra et al. can be interpreted as a direct reference to Eq. 3 and the nonlinear dependence of the multi-photon process rate on theses two variables. For such a double core-hole to be created, the absorption of the second photon described by Santra et al. is temporally limited by the life time of the SCH state. This lifetime is determined by the competing radiative and non-radiative relaxation processes, as this equation from the dissertation of Solène Oberli [72] shows:

$$\Gamma_{SCH} = \frac{\hbar}{\tau_{SCH}} = \Gamma_{Rad} + \Gamma_{A-M} \tag{4}$$

For a double core-hole to be created, the second electron does not necessarily need to be emitted as a photoelectron. Thus, similarly to the single core-hole processes described in subsection 2.1.1, DCH processes can be separated into DCH ionization and resonant DCH excitation.

A sketch of a DCH ionization in Fe is shown in FIG. 4 a.). Fe is chosen as an example, as the samples investigated in this work both feature an Fe center. A second core electron is emitted as a photoelectron within the lifetime of the Auger-Meitner decay within the Fe atom

and can consequently be detected. In FIG. 4 b.), the second electron is not emitted into the continuum, but rather resonantly excited to an unoccupied orbital, or a Rydberg state that is stable within the timescale associated with the lifetime of the electronic processes that follow. To achieve this excitation, the energy of the exciting photon must be tuned along discrete resonances that correspond to the energy level distribution of the chosen target and site. The excited electron e_R will not be detectable as it is still bound, yet the relaxation processes that follow are sensitive to the DCH vacancy. In this case, the observable to investigate is the DCH Auger-Meitner electron emitted during the first relaxation process. Its energy is directly influenced by the presence of the DCH vacancy.

Further complexity is introduced into the processes involving double core-holes when a molecular target with multiple possible excitation sites is introduced as a target. Cederbaum et al. [17] describe in their work on the samples CH_4, C_2H_2, C_2H_4 and C_2H_6 the energies needed to create double core-holes both at the same C site, as well as different ones. Their analysis implies an increase in chemical sensitivity for the study of DCH vacancies, particularly for two-site excitations. Nevertheless, single-site DCH states are also rich in information. In their work on the formation of single-site K-shell DCH-ionized states and DCH resonantly excited states, Koulentianos et al. emphasize the difference in angular distribution of resonantly excited DCH states compared to conventional SCH states, both resonantly excited and ionized [44].

2.2 X-Ray Photoion Spectroscopy

X-Ray photo-ion spectroscopy is one of the major techniques to study the charged product particles of the SCH and DCH photon-matter interactions considered in this work. Applying this technique in modern experiment setups, with a well defined starting point and fine-tuned fields, allows for the accurate resolution of the cationic (and anionic) fragments, which are produced in the above discussed relaxation processes. Using ion time-of-flight (iToF) spectroscopy for this purpose can be traced back to the publication by Wolff and Stephens on a pulsed spectrometer with time dispersion [99]. Today, ion spectroscopy is a favored method to study the fragmentation and charge transfer following an excitation in countless samples and experiments.

An iToF spectrometer detects the charged cation fragments of photon-matter interactions from pulsed X-Ray sources, or continuous X-Ray sources that provide a time zero for a time-of-flight measurement by some other means. The mass-over-charge ratios of the detected fragments can be extracted when accelerating them into a drift region with a well-defined length and potential. Depending on the length of the spectrometer, the parameters of the photons and the target molecules, as well as the potentials applied at various stages of the fragment's path toward the detector, the resulting velocities of each fragment can differ vastly from each other. This can be used to produce separation of cationic particles in the arrival time, the time-of-flight from time zero, on a detector. From the spectrum of cations arriving at a characteristic time-of-flight, the associated mass-over-charge ratio of each detected fragment can be extracted. The equation describing the time-of-flight in such an ion time-of-flight setup can be written using E_{kin} as kinetic energy, q as charge, U as potential, m as the cationic mass,

16

s as distance traveled and *t* as time-of-flight:

$$E_{kin} = qU = \frac{ms^2}{2t^2}$$
$$t = \sqrt{\frac{ms^2}{2qU}}$$

(5)

It is important to mention that Eq. 5 is only applicable, when a well defined time zero is accounted for in the experimental conditions, either in form of a trigger pulse, a photon peak, or an otherwise well defined pulsed light source. The equation also applies only to the most basic instrument design and does not account for important improvements to the scheme that were introduced at later points. For example, the design of most modern iToF spectrometers is based on the design originally proposed by Wiley and McLaren in 1955 [98], which adds some modifications to the experiment. This design differed from previous setups by employing a two-stage extraction field for cations, which compensates for the arrival time dispersion caused by cations distributed in a finite volume. The sort of iToF spectrometer used in this thesis operates by extracting the cationic fragments from a photon-matter interaction volume via the application of an electric field to accelerate the cations through the aperture of a series of electrodes that allow for the retardation of the accelerated cations. Signal detection occurs at the end of a well defined flight distance on an anode behind a stack of signal amplifying micro channel plates (MCPs).

The advantages of this method of detection are outlined in the review on advances in instrumental approaches to time-of-flight mass spectrometry by Brais et al. [13] as high mass-resolution, a theoretically open-ended mass-scale towards high masses, high compatibility with other methods of selection and easy design, mounting and use in a variety of experimental setups. For this work, the last outlined benefit is particularly important, as it is used to perform iToF spectroscopy with an experimental setup that was designed to detect electrons, rather than ions. More details on the specific design of the iToF spectrometer in use during this experiment are given in Section 4.

2.3 X-Ray Photoelectron and Auger-Meitner Electron Spectroscopy

Similar to ion spectroscopy, electron spectroscopy is a method of studying the products of photon-matter-interactions. It has been used for decades to study the product electrons of such experiments, as exemplified by the 1985 review article on the method by Kai Siegbahn [84]. Electron time-of-flight (eToF) spectroscopy differs from such setups in that the electrons are dispersed in time, rather than space. Such a setup can be realized, for example, by fitting an MCP with a delay-line anode. A variety of spectrometers are currently in operation at synchrotron and FEL facilities around the world, such as magnetic bottle electron spectrometers, which were, for example, previously used in the context of the SFB 925 by Mertens [65], or hemispherical analyzers, which are known for their high energy resolution [69].

In an eToF spectrometer, such as they are employed at modern FEL facilities, the electrons resulting from the interaction of sample and X-Ray photon pulse are focused and retarded by a collection of electric and/or magnetic fields, before being detected by an anode after signal

amplification by an MCP stack. This is altogether similar to the process in iToF spectrometry. The differences in iToF and eToF setup in the context of this work are described in the work on the commissioning of high resolution eToF spectrometers for the European XFEL by De Fanis et al. [22] and the citations contained therein. They will be further elaborated on in Section 4.

Both iToF spectroscopy, as well as eToF spectroscopy, when operating in counting mode, yield a signal of counts associated with a certain time-of-flight. For cations, this allows the determination of a mass-over-charge ratio, which in turn gives insight into the fragmentation process in the interaction region. For electrons, this allows for an association of time-of-flight to kinetic energy, which allows for the reconstruction of the electron's origin within the electronic makeup of the sample in question. Specifically, eToF spectroscopy is able to extract kinetic energy from the measured time-of-flight for an electron and, as electron mass is constant, provides the means to trace each detected product electron to the site and emission process of origin within the sample molecule by using energy calculations involving the known binding energies of the electronic orbitals in the sample. For a photoelectron, such a calculation compares the detected kinetic energy to the photon energy of the arriving photon pulse to draw conclusions about the binding energies of the electron's orbital of origin. For Auger-Meitner electrons, the detected kinetic energy of the electron corresponds to the binding energy of its corresponding electronic orbital. This gathered information is used to draw conclusions about the nature of relaxation processes occurring within the sample following irradiation. In the context of this experiment, differentiating between SCH Auger-Meitner electrons and DCH Auger-Meitner electrons lies at the heart of the work of showing DCH Auger-Meitner electron detection in $3d$ metal complexes.

Having discussed the underlying mechanisms of DCH excitation and the succeeding relaxation processes that can occur in $3d$ metal complexes, the next chapter will focus on using theoretical calculations to establish regions of interest in both photon energies as well as kinetic energies in which detection of DCH signatures is likely.

3 Cowan Code Spectra of Isolated Iron Atoms

Having completed the groundwork, calculations of SCH cross-sections and DCH cross-sections will be compared in this section and the region of interest for the study of resonant DCH processes will be defined for the samples studied in this thesis. Furthermore, SCH Auger-Meitner electron spectra of increasing charge states for the isolated Fe atom will be presented.

Experimental detection of non-linear processes such as DCH states in $3d$ metal complexes with an Fe center requires precise knowledge of the expected SCH and DCH cross-sections in relation to the photon energy range of the experiment. Such experiments are complex, as several factors, e.g. the presence of multiply ionized iron cations in the interaction region, can contribute cation- and electron-signals that obfuscate the signal of interest. Knowing the relevant photon energies in which to expect SCH and DCH processes to occur in the sample molecules is therefore quite essential to limit the regions of interest. Furthermore, as SCH and DCH states are competing processes in high intensity X-Ray photon-matter interactions, an understanding of the expected signal for SCH Auger-Meitner electron spectra is similarly indispensable. In order to gain this information, calculations of electronic transitions for isolated Fe cations at different charge states were conducted and will be discussed in this chapter. The calculation of these transitions was conducted with code based on the widely known work of Robert D. Cowan [20].

3.1 The Hartree-Fock Method and the Cowan Code

In employing a variation of the Cowan code, implicit use of the Hartree-Fock method, or Self-Consistent-Field (SCF) method is made, as the code uses a relativistic Hartree-Fock approach to approximate the electronic wavefunctions for the cationic Fe energy orbitals. The Hartree-Fock method [35, 88], has been previously explained in several other works, such as the lecture notes of David Sherrill [83] and the review published by Bartlett and Stanton [7]. The framework will be only briefly explained here, before being expanded on in the context of this work and the modifications carried out on the Cowan code for the goal of approximating X-Ray absorption spectra and Auger-Meitner electron spectra. The unmodified Hartree-Fock method was conceived to approximate a numerical solution for the time-independent electronic Schrödinger equation in a many-electron system. Its compelling feature is the use of Slater determinants as an ansatz to approximate the many-electron wavefunction $\Phi_{x_1...x_n}$:

$$\Phi_{x_1...x_n} = \frac{1}{\sqrt{N!}} \begin{vmatrix} \chi_1(x_1) & \chi_2(x_1) & \dots & \chi_n(x_1) \\ \chi_1(x_2) & \chi_2(x_2) & \dots & \chi_n(x_2) \\ \vdots & \vdots & \ddots & \vdots \\ \chi_1(x_n) & \chi_2(x_n) & \dots & \chi_n(x_n) \end{vmatrix} \tag{6}$$

In Eq. 6, $\Phi_{x_1...x_n}$ represents the Hartree-Fock approximation of the multi-electron system electronic wave function. This approximate wave function is defined as the normalized determinant of spin orbitals, where $\chi_n(x_n)$ stands for a spin orbital in dependence on a set of space-spin coordinates. The Hartree-Fock equation $\widehat{F}|\phi_m\rangle = \varepsilon_m|\phi_m\rangle$, which defines the orbitals using the Fock-operator $\widehat{F}$ and the energy ε, can be written as:

$$h(x_1)\chi_i(x_1) + \sum_{j \neq i}\left[\int dx_2\left|\chi_j(x_2)\right|^2 r_{12}^{-1}\right]\chi_i(x_1) - \sum_{j \neq i}\left[\int dx_2\chi_j^*(x_2)\chi_i(x_2)r_{12}^{-1}\right]\chi_i(x_1) = \varepsilon_i\chi_i(x_1)$$

(7)

In this Eq. 7, h defines the one-electron operator and ε_i represents the energy eigenvalue associated with orbital χ_i. In the SCF approach, the spin orbitals are now refined from an initial guess in consecutive steps to ever better approximations by requiring the minimization of the Slater determinant energy produced by them. In this way, an optimization of orbitals after the initial guess is performed in an iterative loop over the matrix of slater determinants consecutively, until convergence.

The Cowan code and its application have been well described in the review of Alexander Kramida [45]: In a first calculation, single-configuration radial wavefunctions for a spherically symmetrized atom are calculated using the Hartree-Fock method. The radial integrals, including the configuration interactions are computed in the next step. The second part of the code computes the angular matrix elements of the Hamiltonian and diagonalizes it to arrive at the energy levels, transition wavelengths and radiative rates for the electric dipole, magnetic dipole and electric-quadrupole transitions. The fourth step of a typical analysis involves a least-squares fit of the atomic energy levels to adjust Slater parameters to fit experimental levels. The version of the Cowan code in use in this thesis has been expanded and adapted by Michael Martins [55, 56]. These adaptations facilitate the extraction of X-Ray absorption spectroscopy (XAS) predictions and Auger-Meitner-electron spectra directly from the results of the Cowan code calculations. More information on this subject can be found in the review on core level photoionization of the $3d$ metal atoms by Martins et al. [57], which also includes application examples for the isolated iron atom. This approach has previously been used successfully to accomodate the measured $3p$ photoabsorption spectrum of Cr^+ ions by McGuinness et al. [62] and variety of published results on the iron cations, such as Fe^+ and Fe^{2+} by Schippers et al. [80, 81], or Fe^{3+} by Beerwerth et al. [9].

3.2 Calculating Electronic Configurations in Isolated Iron Cations

To inform the experimental detection of resonant DCH Auger-Meitner electrons in $3d$ metal complexes with Fe cores, the Cowan code described above was used to provide cation data for isolated Fe atoms. Besides the neutral Fe atom, the cationic states studied in this manner were chosen to include Fe^+ to Fe^{14+}, to approximate the expected highly ionized iron targets encountered in the photon-matter interaction region of the experiment. Using short and intense X-Ray pulses, such targets are to be expected when ionized fragments of the initial molecules serve as targets for further ionization steps. As the photon energy range of the experiment extends from $680\,eV$ to $800\,eV$, the model assumes an initial photon-electron interaction at the Fe $2p$ site.

In order to gain an accurate understanding of the expected X-Ray absorption cross-sections and the corresponding Auger-Meitner electron spectra which are to be expected from the interaction of X-Ray photons and the $3d$ metal complexes, the possible resulting transitions that were studied for the Fe cations are listed in TABLE 1. The results of the Cowan Code cal-

culations then inform the expected SCH and DCH cross-sections, as well as the SCH Auger-Meitner electron spectra for isolated Fe cation charge states.

A similar consideration was applied to the isolated Fe atom to simulate resonant $2p^2$ DCH excitation. For this model, the Fe atom immediately after SCH $2p$ ionization was considered as the starting point of the transition. Relaxation processes after a subsequent $2p^2$ excitation were calculated according to the transitions detailed in TABLE 2.

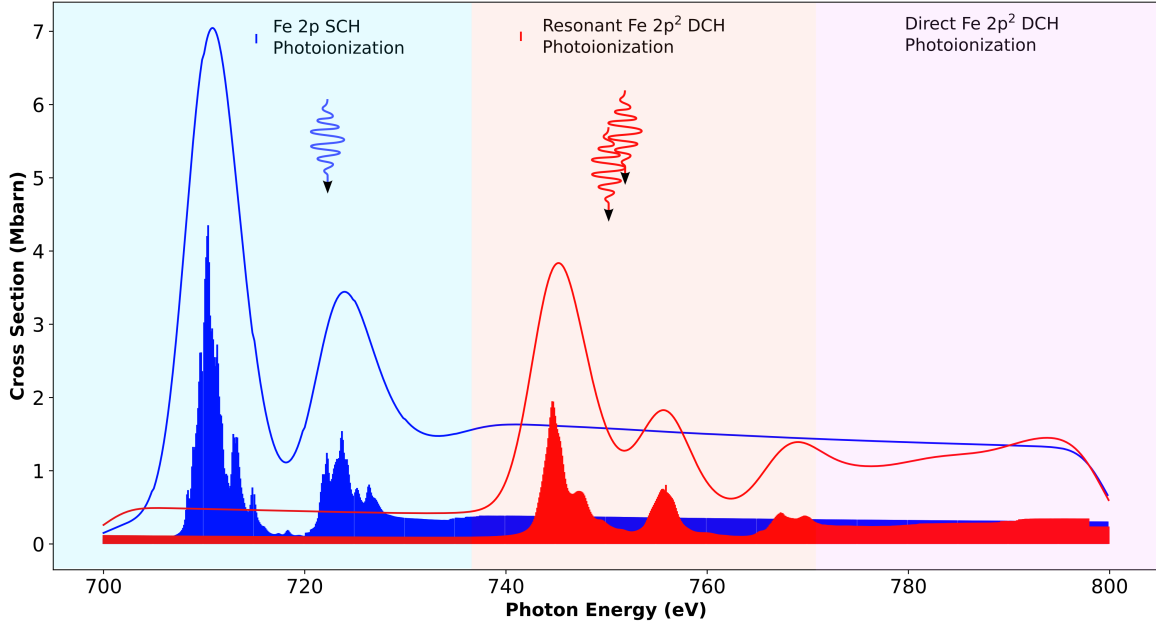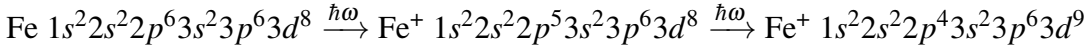## 3.3 Expected SCH and DCH X-Ray Absorption Cross-Sections

Figure 5: The expected XAS cross-sections for a single core-hole (SCH) ionization process (blue line) in Fe, compared to the resonant double core-hole (DCH) excitation (red line) in Fe for the $2p$ and $2p^2$ target sites, respectively. They show three distinct photon energy regions (shown in blue, red, and magenta, respectively), where SCH ionization, resonant DCH excitation, and direct DCH ionization are expected to be the dominant source of signal, respectively. The theoretical cross-sections are produced by convoluting the results of the Cowan code calculations with a Gaussian with a width of 7 eV Full Width at Half Maximum (FWHM) to account for the bandwidth. The rise in the first few calculation points, as well as the curved decline at the end of the calculation interval are known artifacts, that need not match experimental results.
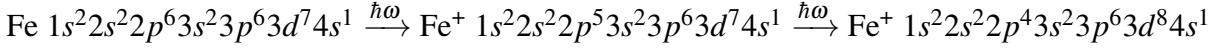
The calculation results of the Cowan Code for the cationic states and electronic transitions detailed in TABLE 1 were used to produce expected X-Ray absorption cross-sections for Fe to Fe^{14+}. The model systems and their expected X-Ray absorption spectra provide insight into the photon energy ranges expected to be most impactful for the photoionization. This

information can be understood easily when plotting the XAS cross-sections for the photon energy range 680 eV to 800 eV. The target interaction for the experiment is focused on the $2p$ electron and the $2p^2$ electron of the Fe center in the $3d$ metal complexes $Fe(CO)_5$ and $Fe(C_5H_5)_2$. Expected XAS cross-sections of the SCH processes for Fe cations therefore inform the experiment's photon energy range for the two complex metals at different cationic states. Furthermore, when compared to the expected XAS cross-section for the $2p^2$ DCH resonant excitation, these simulated XAS cross-sections provide some estimation at which photon energy of the experiment the SCH processes will outweigh DCH processes in their detected signal and vice versa. This latter consideration allows for a general idea of what regions of interest in the photon energy range are particularly suited for the detection of DCH electron- and ion-signal.

FIG. 5 shows the expected cross-sections for the $2p$ photoionization as compared to the resonant $2p^2$ double core-hole photoionization for Fe between 680 eV and 800 eV. Three distinct regions can be seen, which are marked with blue, red and magenta respectively. In the blue region, which extends to approximately 737.5 eV, the signal of the $2p$ photoionization can be expected as the dominant signal source, as the strong resonance for the $2p^2$ DCH excitation is not yet expected to arise. For the region of 737.5 eV to 778 eV, resonances in the Fe $2p^2$ cross-section are expected. A particular region of interest is expected between 740 eV and 760 eV, as the two primary groups of resonant transitions,

$$\text{Fe } 1s^2 2s^2 2p^6 3s^2 3p^6 3d^8 \xrightarrow{\hbar\omega} \text{Fe}^+ \, 1s^2 2s^2 2p^5 3s^2 3p^6 3d^8 \xrightarrow{\hbar\omega} \text{Fe}^+ \, 1s^2 2s^2 2p^4 3s^2 3p^6 3d^9$$

and the alternative

$$\text{Fe } 1s^2 2s^2 2p^6 3s^2 3p^6 3d^7 4s^1 \xrightarrow{\hbar\omega} \text{Fe}^+ \, 1s^2 2s^2 2p^5 3s^2 3p^6 3d^7 4s^1 \xrightarrow{\hbar\omega} \text{Fe}^+ \, 1s^2 2s^2 2p^4 3s^2 3p^6 3d^8 4s^1$$

can outscale the SCH $2p$ photoionization edge. The theoretical calculations of the SCH XAS cross-sections match the measured X-Ray absorption spectra of Godehusen et al., published in their study on iron pentacarbonyl and ferrocene in the gas phase [32].

The calculations that result in FIG. 5 allow a rough estimate of the lifetime of the associated states. Zewail's article [104] on chemistry at the uncertainty limit provides a good explanation for an estimate based on the uncertainty relation:

$$\Delta t \Delta E \geq \frac{\hbar}{2} \tag{8}$$

Eq. 8 can be used on the calculated energy widths of the Cowan code results. The resulting shortest and longest lifetimes for the photon energy regions shown in FIG. 5 and the two excitations considered are shown in TABLE 3. These estimates emphasize the short timescales on which DCH processes occur. DCH spectroscopy provides access to these timescales, even while employing pulses with as much as an order of magnitude longer pulse lengths.

3.4 SCH and DCH Auger-Meitner Electron Spectra for Isolated Iron Cation Charge States

The Cowan Code results for the configurations considered in TABLE 1 provide theoretical Auger-Meitner electron spectra for the isolated Fe charge states in question. With the experimental configuration calling for an intense short X-Ray pulse in the photon energy range of

680 eV to 800 eV interacting with samples $Fe(CO)_5$ and $Fe(C_5H_5)_2$ in gaseous form, sequential ionization of cationic charge states of the central Fe atom is possible. It is also possible for the SCH proccesses in these cations to produce Auger-Meitner electrons of the same order of magnitude of kinetic energy as those resulting from DCH processes. Thus defining regions of interest, not only in the photon energy range, but also the kinetic energy scale of the expected electron signal is necessary. The expected SCH Auger-Meitner electron spectra inform this decision.
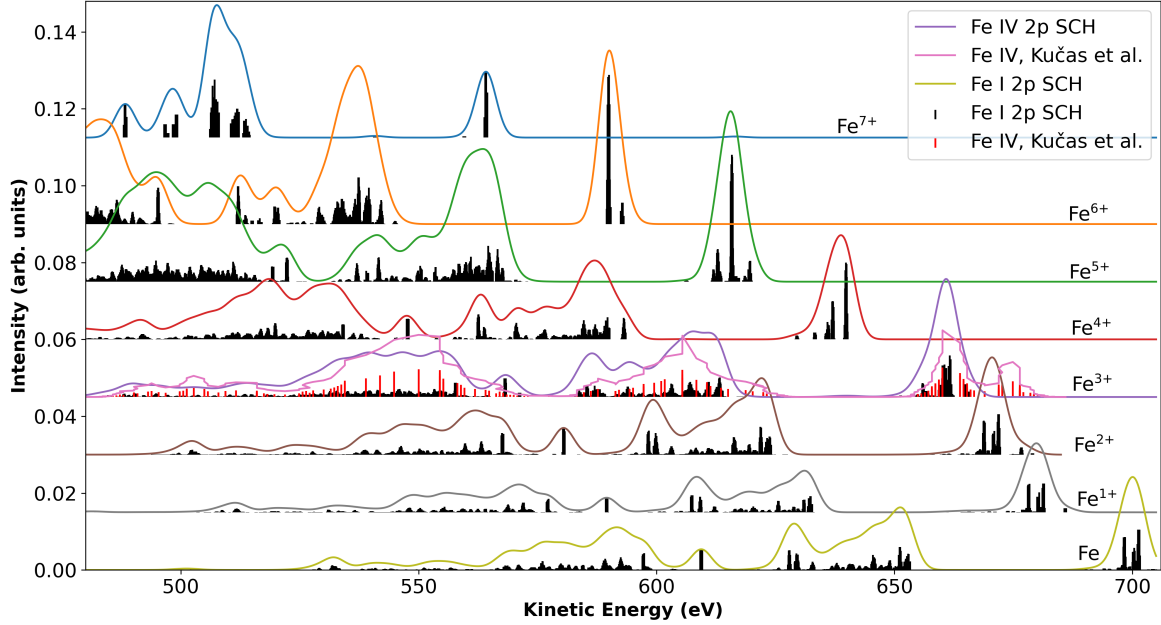

Figure 6: The expected Auger-Meitner electron spectra for $2p$ a single core-hole (SCH) ionization process in the cationic charge states of Fe^{n+} ; n=0-7, denoted in the usual format, where Fe I signifies the neutral isolated Fe atom. This notation may be used in other places in this work. The expected spectra were convoluted with a 7 eV FWHM Gaussian to simulate XFEL experimental conditions. This representation assumes equal interaction (e.g. cross-section) between all cationic charge states and the X-Ray pulse within the interaction region. A trend towards lower modelled kinetic energies with higher charge states is observed for all depicted charge states. The results for Fe_3^+ are compared to the digitized spectra published by Kučas et al. [49] to verify agreement.

FIG. 6 demonstrates the expected Auger-Meitner spectra for an interaction between X-Ray pulse and isolated cationic charge states of Fe, produced in the photon energy range of 680 eV to 800 eV. A bandwidth of 7 eV of photon energy of the FEL was assumed to approximate experimental conditions. The range of expected Auger-Meitner electron binding energies is several 100 eV broad and extends from 1 eV to 800 eV. Here, only the kinetic energy region from 480 eV to 720 eV is shown. Each single charge state contributes three potential signatures to the overall spectrum, resulting from $L_{23}M_{23}M_{23}$, $L_{23}M_{23}M_{45}$ and $L_{23}M_{45}M_{45}$ transitions in

the respective iron cations. Each group of transition lines is separated by a several electronvolts large gap, implying a clear identification of each peak group, even when convoluted with the Gaussian simulating experimental conditions. The overall shape of the collective Auger-Meitner signatures suggests a series of high kinetic energy peaks at close to $700\,\text{eV}$. These peaks decrease in kinetic energy with increasing charge state. The aforementioned grouping, which is prevalent for individual Auger-Meitner spectra, is lost as the prevalent trend to lower binding energies leads to a mixing of high-energy, high-charge-state transitions with low-energy, low-charge-state transitions.

FIG. 6 further reveals this trend of decreasing expected kinetic energies for Auger-Meitner electrons when considering increasing charge states. This observation matches an intuitive understanding of decreasing energy differences between electronic orbitals with each removed electron. Removing multiple electrons from the neutral Fe atom's orbitals increases the effective potential of the core with respect to the remaining electrons. This, in turn, decreases the energy levels associated with the electron orbitals and thereby the binding energy of Auger-Meitner electrons following a SCH process.

Kučas et al. calculated the expected transitions for the Fe^{3+} cation following a $2p$ photoionization [49]. The authors used a Dirac-Fock-Slater approach and a $2p^5 3d^6$ configuration in their work and assume a $1\,\text{eV}$ FWHM Gaussian to simulate bandwidth. Nevertheless, the form of the expected Auger-Meitner spectra (Fe IV in FIG. 6) matches between their work and this thesis, extending to the absolute energy of low binding-energy Auger-Meitner signatures and to the relative position on the energy scale of the three main signal groups towards each other. It is only in absolute binding energy and relative intensities that this work differs from the results of Kučas et al. Our results show the highest binding energy of a Fe^{3+} associated Auger-Meitner electron at a roughly $10\,\text{eV}$ lower energy than the work of Kučas et al. This is a phenomenon that can be ascribed to both the configurations considered in each work, as well as the code in question. Ultimately, comparison between the results of Fe^{3+} does suggest that the results of the Cowan Code calculations tend toward higher absolute kinetic energies.

FIG. 7 shows the the expected Auger-Meitner spectra for an interaction between XFEL and isolated Fe atoms in the photon energy range of $680\,\text{eV}$ to $800\,\text{eV}$. A bandwidth of $7\,\text{eV}$ was assumed for the XFEL pulses. The range of expected Auger-Meitner electron binding energies extends from $0\,\text{eV}$ to $800\,\text{eV}$, but only the $480\,\text{eV}$ to $770\,\text{eV}$ kinetic energy range is shown here. The features of the expected DCH features qualitatively resemble those expected for the SCH process. Three kinetic energy regions can be identified for the expected DCH signal. Of these three, the region extending from $650\,\text{eV}$ to $690\,\text{eV}$ and the region extending from $705\,\text{eV}$ to $747\,\text{eV}$ are particularly important. Here the iron DCH signal not only presents rather strongly, but is also predicted to be mostly unencumbered by SCH signal. These two regions of interest on the kinetic energy scale are separated by a rather strong SCH signal around $700\,\text{eV}$, with clearly defined features and a narrow band of peaks.

This chapter illustrated via use of Cowan code that the expected photon energy region of interest for the resonant DCH cross-section to outscale that of SCH processes occurs between $737.5\,\text{eV}$ and $778\,\text{eV}$. It also detailed that encumbrance in the detection scheme by SCH electron signal could be avoided in the region extending from $650\,\text{eV}$ to $690\,\text{eV}$ and the region extending from $705\,\text{eV}$ to $747\,\text{eV}$ and onward. The next chapter presents the experimental setup that was used to detect DCH signatures and provides details on the studied samples.
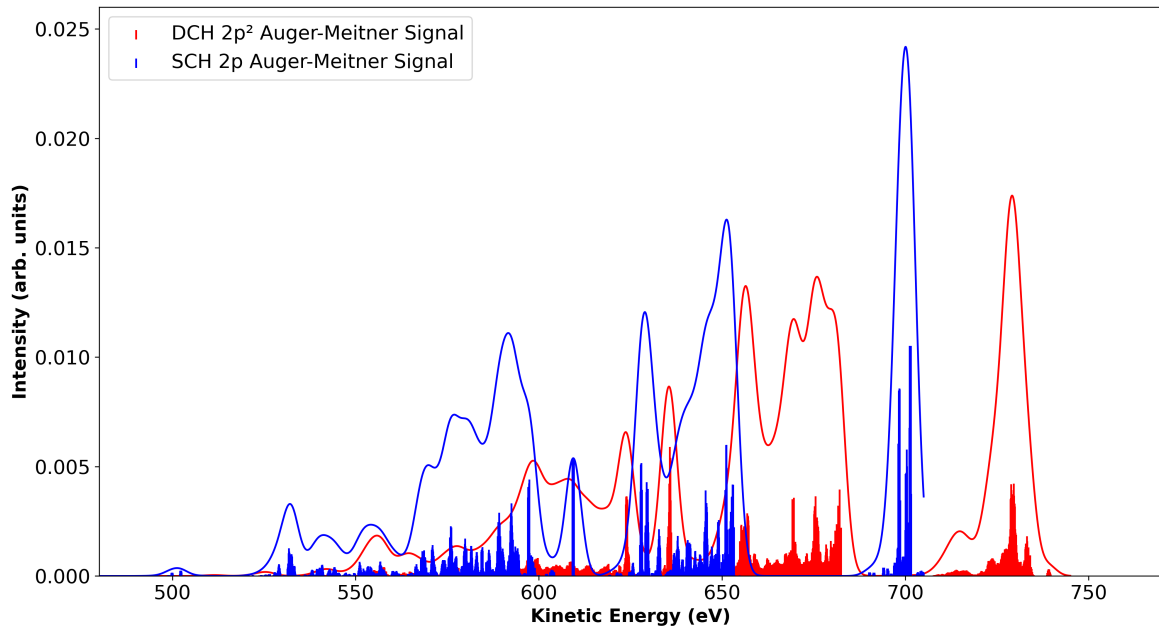
Figure 7: The Auger-Meitner electron spectra expected for the $2p$ site and a single core-hole ionization process in the isolated iron atom (blue line), compared to the expected Auger-Meitner signal expected for the $2p^2$ site and a double core-hole ionization process (red line). The expected spectra were convoluted with a 7 eV FWHM Gaussian to simulate XFEL experimental conditions. The $2p^2$ signal appears without overlap at two kinetic energy regions between approximately 660 eV and 690 eV and at kinetic energies higher than 705 eV.

Fe charge state	Ground States	Electronic Transitions
Fe^{N+} ; N=0-5	$1s^2 2s^2 2p^6 3s^s 3p^6 3d^{8-N}$	$3d^{-1} + e_{ph}^{+1}$
	$1s^2 2s^2 2p^6 3s^s 3p^6 3d^{7-N} 4s^1$	$4s^{-1} + e_{ph}^{+1}$
	$1s^2 2s^2 2p^6 3s^s 3p^6 3d^{6-N} 4s^2$	$2p^{+1} + 3p^{-1} + 4s^{-1} + e_{AM}^{+1}$
Fe^{6+}	$1s^2 2s^2 2p^6 3s^2 3p^6 3d^2$	$2p^{+1} + 3p^{-1} + 3d^{-1} + e_{AM}^{+1}$
	$1s^2 2s^2 2p^6 3s^2 3p^6 3d^1 4s^1$	$2p^{+1} + 3s^{-1} + 3p^{-1} + e_{AM}^{+1}$
Fe^{7+}	$1s^2 2s^2 2p^6 3s^2 3p^6 3d^1$	$2p^{+1} + 3p^{-2} + e_{AM}^{+1}$
	$1s^2 2s^2 2p^6 3s^2 3p^6 4s^1$	$2p^{+1} + 3s^{-2} + e_{AM}^{+1}$
Fe^{N+} ; N=8-12	$1s^2 2s^2 2p^6 3s^2 3p^n; n = 6,5,4,3,2$	$2p^{+1} + 3s^{-1} + 3d^{-1} + e_{AM}^{+1}$
		$2p^{+1} + 3s^{-1} + 4s^{-1} + e_{AM}^{+1}$
Fe^{13+}	$1s^2 2s^2 2p^6 3s^2 3p^1$	$3d^{-1} + e_{ph}^{+1}$
		$4s^{-1} + e_{ph}^{+1}$
		$2p^{+1} + 3p^{-1} + 4s^{-1} + e_{AM}^{+1}$
		$2p^{+1} + 3p^{-1} + 3d^{-1} + e_{AM}^{+1}$
		$2p^{+1} + 3s^{-1} + 3p^{-1} + e_{AM}^{+1}$
		$2p^{+1} + 3s^{-2} + e_{AM}^{+1}$
		$2p^{+1} + 3s^{-1} + 3d^{-1} + e_{AM}^{+1}$
		$2p^{+1} + 3s^{-1} + 4s^{-1} + e_{AM}^{+1}$
Fe^{14+}	$1s^2 2s^2 2p^6 3s^2$	$3d^{-1} + e_{ph}^{+1}$
		$4s^{-1} + e_{ph}^{+1}$
		$2p^{+1} + 3s^{-1} + 3p^{-1} + e_{AM}^{+1}$
		$2p^{+1} + 3s^{-2} + e_{AM}^{+1}$
		$2p^{+1} + 3s^{-1} + 3d^{-1} + e_{AM}^{+1}$
		$2p^{+1} + 3s^{-1} + 4s^{-1} + e_{AM}^{+1}$

Table 1: The cationic states of isolated Fe atoms that were considered for the $2p$ SCH excitation and ionization. The electronic transitions following such a SCH process consist primarily of Auger-Meitner processes. Other relaxation processes, such as fluorescence are considered to be negligible for these sample cations and this target interaction.

Fe charge state	Ground States	Electronic Transitions
Fe$^+$	$1s^2 2s^2 2p^5 3s^s 3p^6 3d^{8-N}$	$3d^{-1} + e_{ph}^{+1}$
	$1s^2 2s^2 2p^5 3s^s 3p^6 3d^{7-N} 4s^1$	$4s^{-1} + e_{ph}^{+1}$
	$1s^2 2s^2 2p^5 3s^s 3p^6 3d^{6-N} 4s^2$	$2p^{+1} + 3p^{-1} + 4s^{-1} + e_{AM}^{+1}$
		$2p^{+1} + 3p^{-1} + 3d^{-1} + e_{AM}^{+1}$
		$2p^{+1} + 3s^{-1} + 3p^{-1} + e_{AM}^{+1}$
		$2p^{+1} + 3p^{-2} + e_{AM}^{+1}$
		$2p^{+1} + 3s^{-2} + e_{AM}^{+1}$
		$2p^{+1} + 3s^{-1} + 3d^{-1} + e_{AM}^{+1}$
		$2p^{+1} + 3s^{-1} + 4s^{-1} + e_{AM}^{+1}$

Table 2: The considered $2p^2$ DCH excitation and ionization. The electronic transitions following such a DCH process consist primarily of Auger-Meitner processes.

Fe Excitation	Photon Energy Region (eV)	Lowest Lifetime (fs)	Longest Lifetime (fs)
$2p$	$700 - 720$	0.23	2.1
	$720 - 730$	0.29	1.83
$2p^2$	$740 - 750$	0.58	0.74
	$750 - 760$	0.59	0.76
	$760 - 780$	0.42	0.75

Table 3: An estimation of shortest and longest lifetimes for $2p$ and $2p^2$ excitations in an isolated Fe atom. While the $2p^2$ excitations show very little lifetime variance between photon energy regions, $2p$ lifetimes vary by as much as 0.27 fs in maximum lifetime.

4 Experiments and Samples

To study ultrafast processes in molecules, the European X-Ray Free-Electron Laser (XFEL) in Hamburg, Germany provides intense, bright, coherent X-Ray pulses. These ultrashort, brilliant X-Ray pulses were used in the work this thesis is based on to excite small, isolated $3d$ metal compounds in a gas-phase experiment. In order to study processes in these samples, which respond in a nonlinear fashion to the energy of the X-Ray pulse, such as the resonant iron $2p^2$ DCH excitation, a series of ion- and electron-spectroscopy measurements was conceived and conducted with varying X-Ray pulse energy to establish the pulse energy and signal intensity data for both, product-ions, as well as -electrons.

A series of diagnostic tools provides the required information about the beam properties, specifically its pulse energy and pulse length. The product ions and electrons of the resulting photon-matter interaction are detected via ion- and electron-time-of-flight spectroscopy using the Atomic Quantum Systems (AQS) endstation of the scientific instrument Small Quantum Systems (SQS) at the SQS beamline at European XFEL. For more information, please consider the publication of Meyer et al. [66] on the instrument and the citations contained therein.

4.1 European XFEL

The European XFEL is a free-electron laser (FEL) facility which is providing exceedingly brilliant soft and hard X-Ray pulses to an international users community. It operates coherently in the energy regime of 0.25 keV to 25 keV . A detailed description of FELs and the European XFEL, its setup and operation principles can be found in the works of Saldin et al., Tschentscher et al., and Weise & Decking [77, 92, 96] and the references contained therein.

Beam generation at the European XFEL starts with a set of electrons emitted into a 1.7 km long linear accelerator of superconducting radiofrequency (SRF) cavities, which enable the high-energy, high-intensity and high-frequency beams required for the study of ultrafast processes in complex molecules [87]. These SRF cavities accelerate the electron beam to relativistic velocities, before it passes through a spatially periodic assembly of magnets called undulators. The alternating magnets of the undulators force the electron beam on a sinusoidal path and to emit electromagnetic radiation along it's forward vector due to relativistic effects. The undulator equation describes the fundamental wavelength λ of the emitted electromagnetic wave [1]:

$$\lambda = \frac{\lambda_W (1 + K^2)}{2\gamma^2} \tag{9}$$

In this Eq. 9, λ_W is the undulator period, $K = \frac{eB_W \lambda_W}{2\pi m_e c}$ is the undulator parameter, B_W is the root mean square (rms) value of the undulator field, γ is the relativistic factor, c the velocity of light and m_e and e are the mass and charge of the electron, respectively. As the undulators force the electron beam to take on a sinusoidal form, the emitted electromagnetic waves that are propagating along the undulator axis interact with the electron beam and create a structure of electron packets within the bunch which is known as microbunching. As the radiation emitted by these microbunches is particularly brilliant, short, and coherent, this Self-Amplified Spontaneous Emission (SASE) principle, is particularly useful for beam generation at the Eu-

ropean XFEL. The statistical nature of the SASE process does, however, entail that each pulse emitted by the machine can vary from the previous one when it comes to pulse parameters, such as pulse length, wavelength, or pulse energy. The European XFEL can provide a pulse frequency of 27 kHz with wavelengths between 0.05 nm and 4.7 nm at an average brilliance of $1.6 * 10^{25} (photons/s/mm^2/mrad^2/0.1\% \, bandwidth)$.

For the European XFEL proposal 2880, during which the measurements on ferrocene and ironpentacarbonyl for this work were taken, a beam profile with 100 pulses per pulse train at a pulse train length of 200 μs was requested at the SQS, so the duration of a single pulse was requested to be 20 fs. This falls into the capabilities of the machine. During an indirect measurement at the same SASE 3 undulator beamline that was used for this proposal, an indirect pulse duration measurement by Khubbutdinov et al., yielded possible pulse durations of as low as 10 fs [40]. With a central photon energy of 750 eV at a bandwidth of 7.5 eV to excite the resonant iron $2p^2$ double core-hole, the maximum energy of a single pulse was requested to be at least 1 mJ in order to increase the detection efficiency of the nonlinear resonant $2p^2$ DCH response to the point where it outscales the background of iron $2p$ photoionisation. The spot at the interaction region was requested not to be larger than 3 μm. The requested parameters were delivered and, where possible, verified before the measurements.

4.1.1 Beam Diagnostics and Pulse Energy Measurements

The SASE process of the European XFEL creates fluctuating X-Ray pulse parameters due to its statistical nature. This calls for a shot-to-shot monitoring of the X-Ray pulses, in order to ensure that the requested X-Ray pulse parameters are not foregone in the individual pulse. For the gas-phase experiment of this work, there are three X-Ray pulse parameters, which are particularly important; the wavelength, the pulse energy and the pulse duration.

The pulse energy E_{pulse}, in terms of the number of photons N_{photon}, their wavelength λ_{photon} the Planck constant $\hbar$ and the speed of light c is defined as:

$$E_{pulse} = \frac{N_{photon} \, \hbar \, c}{\lambda_{photon}} \tag{10}$$

It can be measured for the average X-Ray pulse using a X-Ray Gas Monitor Detector (XGMD). The principles of a XGMD, as they are used within the larger setup of a X-Ray Gas Monitor (XGM) at European XFEL, are described in the works of Maltezopoulos et al. [53] and Sorokin et al. [90], as well as the references contained in these publications. An XGM, as they are used at European XFEL, consists of a combination of two XGMDs and two Huge-Aperture Open Electron Multipliers (HAMPs). The measurement principle of the XGMD part of the XGM is based on the photo-ionization of rare gas atoms, after which the product ions are detected with Faraday cups and the product electron signal is measured over a capacitor and digitized. The number of photons passing through the detector can be reconstructed from the number of detected charged particles via the Beer-Lambert law:

$$N_{photon} = \frac{N_{particle}}{1 - exp(-\sigma_{ph} \, z_{eff} \, n_{atom})} \cong \frac{N_{particle}}{\sigma_{ph} \, z_{eff} \, n_{atom}} \tag{11}$$

31

As further described by Sorokin et al. [90], the HAMP part of the XGM extracts the ions created by the photo-ionization of these rare gas atoms with a homogeneous electric field, before amplifying the secondary electron signal via a series of 24 activated CuBeO grid dynodes connected via a passive resistance divider of $29\,M\Omega$ upon ion impact on the first grid. This amplification scheme keeps the information about the position of the primary ion impact, which can be treated as a projection of the photon beam position, intact throughout the amplification process. Thus, the HAMP part of the XGM preserves not only the relative photon flux, which can be cross-calibrated against the absolute measurement of the XGMD, but also the photon beam position.

The photon beam position could be further monitored via camera by a series of scintillator screens that allow the observation of an energetically weaker photon beam to optimize the beam transport to the scientific instrument in use. The last of these screens is a Yttrium Aluminium Granat (YAG) screen placed at the desired postion of the photon-matter interaction point. This also makes it possible to verify the spot size for the energetically weaker photon beam.

During the experiment, the energy of the X-Ray pulses arriving at the photon-matter interaction region was tuned by using the Gas Attenuator (GATT) instrument for the SASE 3 soft X-Ray beamline at European XFEL. The instrument is described by the poster of the X-Ray Optics and Beam Transport Group [34] and the article on the beamline published by Dommach et al. [26], as well as the references contained therein. This device allows for the transparent attenuation of pulse energy at the photon-matter interaction point. A gas absorption cell is placed upstream of the scientific instrument and filled with Nitrogen or Xenon, to achieve a certain gas density within the $15\,m$ long FEL beam path within the instrument. Its operative photon energy range of $260\,eV$ to $3500\,eV$ accommodates well the desired scanning range of the photon energies of $680\,eV$ to $830\,eV$ which were used in the experiments. Features of particular importance for this work are the instruments attainable attenuation factor of 0.01 orders of magnitude to at least 3 orders of magnitude, independently from gas type or photon beam energy.

The cross-section of the resonant iron $2p^2$ DCH excitation, the focus of this thesis, grows exponentially more likely with higher pulse energies. Thus, using the GATT to attenuate the beam energy to a small percentage of its original magnitude reveals the spectral signatures of the DCH excitation in contrast.

During this work, two XGM were used to amass the body of pulse energy measurements that provide the backbone of the pulse energy considerations that the work upon which this thesis is based relies on. One of these is placed past the GATT and provides the most accurate information on the pulse energy provided by the above-mentioned attenuation. The second XGM that was used for a majority of the pulse energy data used in this work is placed within the SQS scientific beamline and provides additional information on the beamline transmission.

The two primary instruments to accomplish the task of temporal pulse characterization are the Photon Arrival time Monitor (PAM), located in a diagnostics chamber downstream from the photon-sample interaction point, and the photoelectron streaking technique, which is also located in a diagnostics chamber downstream from the photon-sample interaction point. The PAM is described in the works of Czwalinna et al. [21] and Grychtol et al. [33] as well as the references contained therein. It overlaps a linearly chirped optical laser pulse spatially
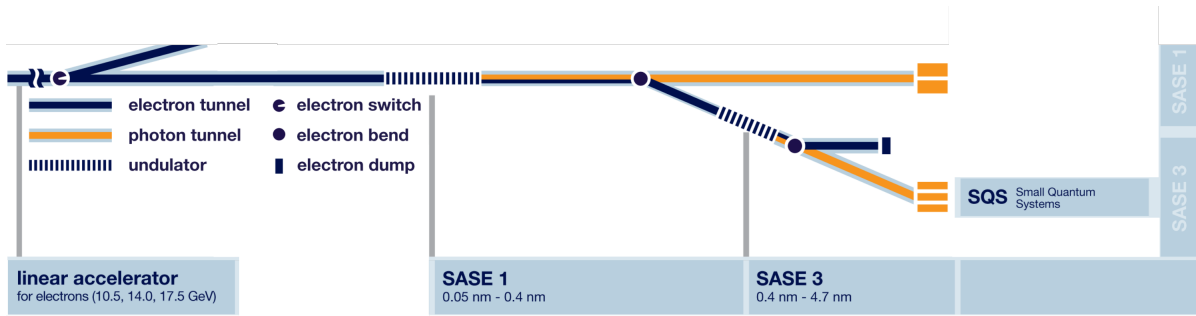
Figure 8: A sketch of the XFEL accelerator and undulators merging into the scientific instrument small quantum systems. The electron and photon tunnels involved in the beam transfer towards the instrument are displayed, as well as the two undulators responsible for the emitted wavelength. Figure adapted from the official press release of the XFEL press office for the occasion of the third light source generating first X-Ray light [4]. Adaptations encompass cropping of other beamlines involving SASE 2, as well as other scientific instruments at SASE 3 and SASE 1.

and temporally with the FEL at the same position in a rare gas sample. In this FEL-pump-optical-probe constellation, the arrival time of the FEL is imprinted to the transmission modulation of the optical beam. The overall measurement uncertainty of this technique is given by Czwalinna et al. [21] as 3 fs. The photoelectron streaking technique that is used to measure the pulse duration is described in [59] and the references contained therein. In this part of the diagnostics chambers, a few-cycle IR laser pulse is superposed in a rare gas sample onto the XUV pulse from the FEL, which ejects photoelectrons from the rare-gas target. The initial kinetic-energy distribution of the emitted electrons is pumped by the FEL and probed by the optical field. As the photoemission is limited to a much shorter period than the half-cycle of the superposed field, the streaked photoelectron kinetic-energy distribution is encoded with the temporal structure of the ionizing pulse. An additional feature of this technique is its ability to resolve the pulse duration on a shot-by-shot basis.

The pulse duration of the X-Ray pulses interacting with the sample was not verified directly during this experiment, as it was up to date never measured directly at the European XFEL [76]. It was, however, estimated based on the electron bunch charge in the accelerator to be 30 fs with an associated error of 10 fs, which was found to be in sufficient accordance with the requested 20 fs for the purposes of this experiment. The tools integrated into the scientific instrument Small Quantum Systems beamline offered some further bunch pattern overview.

4.1.2 Scientific Instrument Small Quantum Systems

The scientific instrument Small Quantum Systems (SQS) is one of the scientific instruments in use at the European XFEL facility. Its design purpose is the study of non-linear and multi-photon processes, as well as time-resolved studies of ultra-fast dynamic processes. The scientific instrument is particularly suited for studies on atomic and molecular systems, as well as clusters, nano-particles and small bio-molecules [66]. In this context, the particular suitability of the SQS instrument for the study of non-linear processes in molecular targets stems from

its access to the highly intense XFEL X-Ray pulses in the soft X-Ray regime in combination with the instruments variable end chambers for detection and analysis.

This regime is accessed, as shown in FIG. 8, via the SASE 3 undulator that allows for photon wavelengths in the range of 0.4 nm to 4.7 nm, corresponding to a photon energy range of roughly 240 eV to 3 keV [82]. For this experiment, a central photon energy of 750 eV was chosen. Following the SASE 3 undulator, a horizontal and vertical chicane are passed. They are well described by the commissioning results of Mazza et al. [61] and the citations contained therein. As a horizontal chicane, two mirrors are passed by the photon beam. They constitute the chicane that filters out high-photon-energy background and additional contributions from higher harmonics. Their pitch and transverse position were established at three different working grazing-incidence angles by Mazza et al. [61]. For the measurements conducted in this work, the working point at 20 mrad was chosen. The vertical chicane is established by two mirrors passed by the photon beam after the horizontal chicane. They additionally improve the focus of the beam and were set up for the matching 20 mrad setting during the measurements of this work.

The photon pulses produced by the SASE undulator of the XFEL are focused using a Kirkpatrick-Baez (KB) mirror system, which is described in the work of Mazza et al. [58] and the citations contained therein. This mirror system is comprised of a series of physically deformable and sometimes retractable mirrors in the horizontal and vertical plane. They focus the beam to three possible photon-matter interaction points, using a set of beam transport configurations that determine the beam path and whether or not intermediate focusing is applied before focusing the beam at the chosen interaction point. The chosen interaction point depends on which of the various end stations available at SQS is currently in use. For our experiments, the Atomic Quantum Systems (AQS) end station was chosen, as its feature combination of gas needle target delivery and high-resolution time-of-flight spectrometer setup makes it the ideal chamber for the experiments carried out over the course of this work.

4.1.3 AQS End Station

The AQS End Station houses a sample delivery needle with the interaction point of photon beam and sample flow directly beneath it, as well as the time-of-flight spectrometers used to detect the product ions and electrons of the excitation.

The sample was delivered to the interaction point by means of effusive gas needle. This injection device, mounted on a manipulator within the AQS end station, was used to deliver both samples. The iron pentacarbonyl sample $Fe(CO)_5$ undergoes a phase transition to a gas under the high vacuum within the AQS chamber. The sample could therefore be mounted directly onto the gas needle in its liquid phase at room temperature and pressure to be evaporated by the establishment of the vacuum within the chamber. The ferrocene sample $Fe(C_5H_5)_2$ is solid at room temperature and ambient pressure. To provide an effusive gas stream at the interaction region, it was mounted in a gas bubbler onto the gas needle. Under the action of the high vacuum within the AQS end station and an additional carrier gas, the sample entered gaseous form and was delivered to the interaction region. Helium was used as a carrier gas to provide a reliably tuneable pressure at the interaction region.

The detection of product electrons is accomplished in this thesis by using electron time-of-

flight spectrometers (eToF spectrometers). As described in the work of Moreschini et al.[67], the base functionality of the eToF spectrometer, as applied in this thesis, is the determination of an electrons kinetic energy by timing its path through a fixed distance drift tube between the photon-sample interaction region and a Micro Channel Plate (MCP) detector. In the eToF spectrometer's roughest design, after experiencing an initial retardation voltage, the electrons traverse a nearly-free-field drift tube at constant velocity, before being detected by the anode after being amplified by the MCP stack. Hemmers et al., in [36], give the energy resolution of an eToF spectrometer as:

$$
\frac{\Delta E}{E} = \sqrt{\left(\frac{2\Delta t}{t}\right)^2 + \left(\frac{2\Delta l}{l}\right)^2 + \left(\frac{2\Delta \lambda}{\lambda}\right)^2} \tag{12}
$$

Here, $\frac{\Delta t}{t}, \frac{\Delta l}{l}$ and $\frac{\Delta \lambda}{\lambda}$ stand for the uncertainty in time, electron flight path length and wavelength, respectively. A detailed account of the AQS electron time-of-flight spectrometers, their design and working principles was given by De Fanis et al. in [22] and the citations contained therein.

In the AQS end station, six identical eToF spectrometer are arranged in triplets around two interaction points and provide angle-resolved electron spectroscopy with multi-hit capability even at high pulse-repetition rates, large accessible energy windows and high energy resolution. One triplet, shown in FIG. 9, is placed in the vertical plane orthogonal to the beam path directly aligned at the photon-matter interaction point. In said plane, two eToF spectrometers form a vertical-horizontal orthogonal pair, while one is positioned at the 'magic' angle of 54.7° from the horizontal. The other triplet is placed in a vertical plane upstream of the interaction point. Here, two eToF spectrometers are placed in the horizontal, while one is aligned at a 45° angle from the horizontal. In this thesis, all six eToF spectrometers were used, with focus being placed on the primary triplet of eToF spectrometers. In order to observe the electron kinetic energy regions of interest from 500 eV to 750 eV outlined in FIG. 7, each of the three eToF spectrometers in the primary triplet was set to a different retardation voltage. These retardation voltages were mirrored in the second triplet. The individual retardation voltage for each eToF spectrometer is given in TABLE 4.

eToF	$V_{Detector}$ (V)	V_{Front} (V)	V_{Mid} (V)	V_{Back} (V)	V_{Drift} (V)	V_{Shield} (V)	**Angle**(°)
1	2450	0	-320	-432	-480	20	90
2	2350	0	0	0	0	2	0
3	2400	0	-427	-576	-640	20	54.7
4	2350	0	-320	-432	-480	0	90
5	2350	0	-427	-576	-640	20	0
6	2400	0	0	0	0	0	54.7

Table 4: Exemplary eToF spectrometer settings are shown for both triplets of eToF spectrometers. The retardation voltages applied to V_{Drift} for the first triplet (eToF 1-3), shown in FIG. 9, are mirrored for the second triplet (eToF 4-6) and define the observed regions of interest.
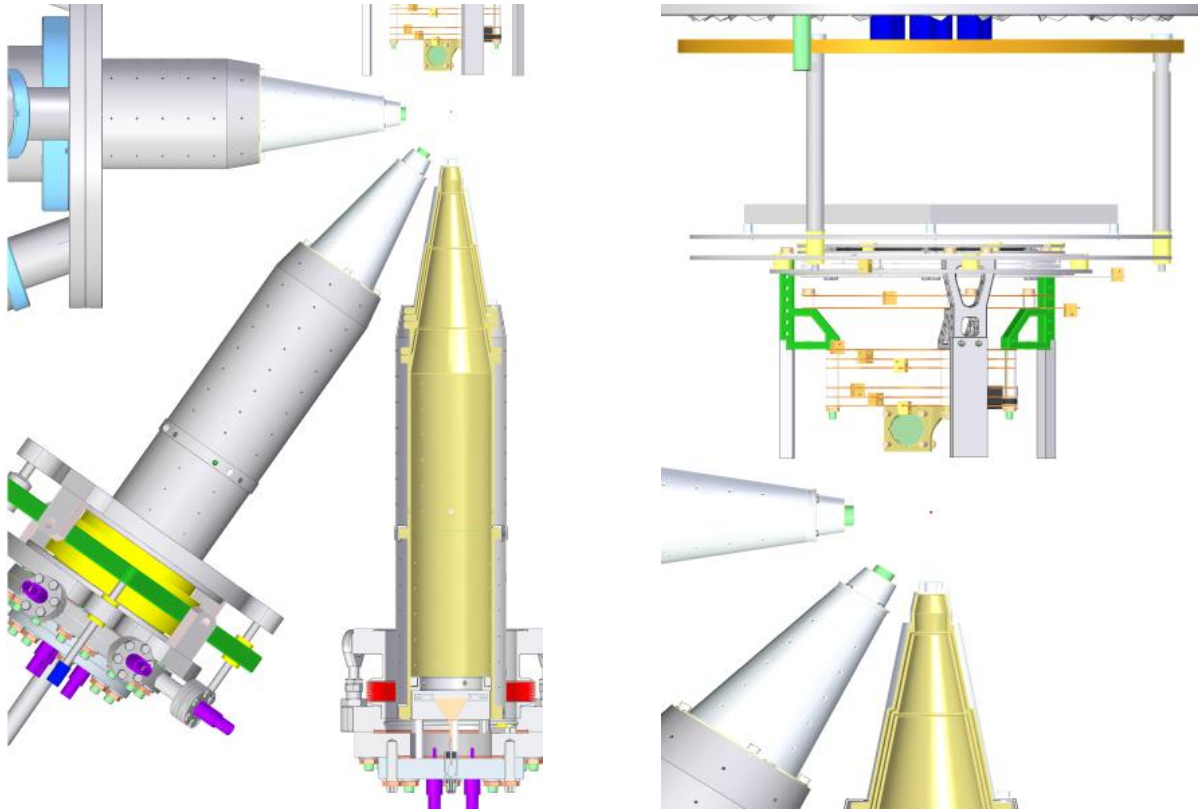
(a) The eToF triplet design in use at the AQS end station.

(b) The primary interaction point of the AQS end station.

Figure 9: Two drawings of the eToF spectrometer detectors used in the AQS end station of the SQS instrument. FIG. 9a shows a drawing of a triplet of eToF spectrometers used in the AQS endstation and their configuration within the chamber around the primary interaction point. The design and functionality of these apparatuses is described in the work of De Fanis et al. [22]. Vertical and horizontal eToF spectrometers are supported by a third eToF angled at the 'magic' angle of $54.7°$ from the horizontal and the polarization surface. FIG. 9b focuses on the interaction point and shows the circular plates used as biasing to arrive at an iToF spectrometer configuration in combination with the vertical eToF spectrometer (shown in gold). Both figures were adapted from the website of the European XFEL [27] without changes.

In their work, De Fanis et al. [22] provide simulated and measured data for ΔE in relation to the retardation voltage applied to V_{Drift} and the remaining kinetic energy of the electron in the drift tube. For retardation voltages of $0\,\mathrm{V}$ and $-750\,\mathrm{V}$ and remaining kinetic energies of at maximum $45\,\mathrm{V}$, De Fanis et al. give the energy resolution $\Delta E \approx 300\,\mathrm{meV}$ and $\Delta E \approx 500\,\mathrm{meV}$, respectively.

One of the eToF spectrometers described above is installed co-axially opposite the interaction region from a Velocity Map Imaging (VMI) spectrometer [66]. It is shown in gold in FIG. 9. By applying a biasing voltage to the circular electrodes of the VMI, the eToF spectrometer can function as a high resolution ion Time-of-Flight (iToF) spectrometer instead. This is enabled by applying the aforementioned potential on the electrodes of the VMI while simultaneously switching the voltage biases on the eToF spectrometer to enable a detection of ions. Ions, which are created at the interaction point, are now forced to enter through the $20\,\mathrm{mm}$ iToF aperture by the strong electric field emanating from the VMI electrodes. This configuration is shown in FIG. 9b. Similar to its use as an eToF spectrometer, a voltage is applied to the iToF spectrometer's drift tube, this time inverted. This focuses the flight path of the ions on their way towards the MCP, to which a negative potential is applied in order to attract the ions. The time-of-flight of the ions is measured relative to the trigger of the arriving X-Ray pulse. From the applied biasing voltages and the measured time-of-flight relative to the arrival of the X-Ray pulse, a mass-over-charge ratio can be constructed using the equation describing the relation between time-of-flight and mass-over-charge ratio, as was described in Section 2. This time-of-flight equation will be given here again, for convenience:

$$
E_{kin} = qU = \frac{ms^2}{2t^2}
$$
$$
t = \sqrt{\frac{ms^2}{2qU}}
$$
(13)

As described in Eq. 13, the iToF spectrometer cannot distinguish between different particles of the same mass-over-charge ratio $\frac{m}{q}$, nor can it detect neutral particles. The iToF spectrometer has been used at the AQS end station successfully in the past [22, 51].

4.2 Data Acquisition and Processing

The data acquisition and support infrastructure at the European XFEL are extensive. While the description of data processing given here suffices for the scope of this work, further details concerning this topic can be found in [29] and the references contained within.

During the recording of iToF signals, the MCP detector signal was continuously recorded for the whole X-Ray pulse train. For this type of measurement, the bunch rate being used at the SQS instrument was set to $47.020\,\mathrm{kHz}$ to avoid overlapping of spectra (slow ions), resulting in a bunch period of $21\,267.69\,\mathrm{ns}$ between recorded bunches. The MCP signal of the iToF spectrometer was read out by the SQS digitizer integrated into the scientific instrument. It allows, via interleaving of two alternate readouts via two alternate fast recorders, to record the MCP signal at $\frac{4GS}{1s}$. This sampling rate results in a sample being taken every $0.25\,\mathrm{ns}$ and allows for resolutions of even very short signal pulses of the duration of $\approx 1\,\mathrm{ns}$.

During the measurements of the eToF spectrometer signals, this sampling rate was maintained for the eToF detector 1 (as seen in TABLE 4), associated with the retardation region of interest at 480 eV. The other eToF spectrometers were sampled using a rate of $\frac{2GS}{1s}$, resulting in a sample being taken every 0.5 ns. For the recording of the electron time-of-flight signals, the bunch rate for the SQS scientific intrument was requested to be 1.1 MHz. The bunch period was 886.15 ns.

For both types of signal, the recording of MCP signal traces corresponding to X-Ray pulse trains via the SQS digitizer leads to an ID of the corresponding train being saved, alongside the measurements taken from both parts of the XGM, GMD and HAMP. Similarly, the current settings of photonenergy and the GATT value are recorded and saved. Next, the eToF or iToF recorded trace of each X-Ray pulse train is cut into signal slices corresponding to single X-Ray pulses identified by a time zero and a length of trace. This allows for the inspection of the averaged signal of an entire run of X-Ray pulses.
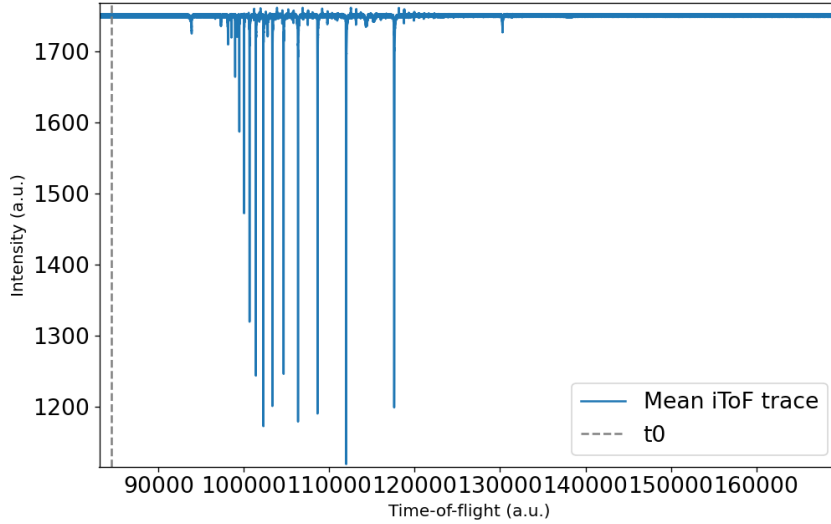
Figure 10: An averaged ion spectrum of the sample $Fe(CO)_5$ for a single run in its rough form, as recorded by the iToF spectrometer detailed in Section 4.1.3. The line of cut t_0, at which the traces were separated and averaged, is marked.

FIG. 10 shows the averaged trace of an entire run for a single spectrometer. The visibility of the signal can be increased further by applying a baseline filter and a constant fraction discrimination threshold to the signal. Next, the cut traces are associated with their corresponding pulse energy, which itself is extracted from the corresponding recorded XGM measurements. Both the photon energy, as well as the GATT transmission setting affiliated with the original X-Ray pulses, are also connected to the spectrometer signal detected for a single pulse. Once these measurements are integrated, the resulting data is then filtered by the average pulse energies, for the two XGMs involved, respectively. Measurements with pulse energies lower than 85% of the average pulse energy are filtered out. Similarly, spectra with pulse energies exceeding 115% of the average pulse energy are filtered out as well. This serves to unify the

pulse energies considered over a given photon energy range. Calibration of the spectrometer occurred using the known spectra of Argon as reference points for a time-of-flight to mass-over-charge conversion. The measurements using some calibration samples were carried out during the beamtime. Following this calibration, a logarithmic X-axis and indicators of the time-of-flight for the mass-over-charge ratio associated with the successive charge states of iron are added. FIG. 11 shows an examplary ion spectrum with the iron charge states marked.
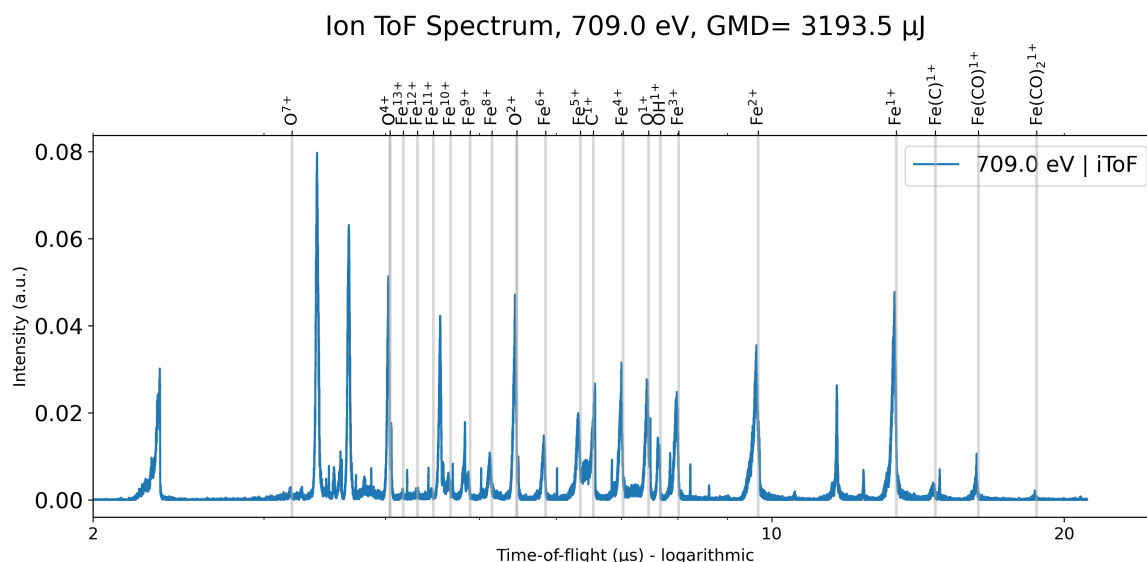
Figure 11: An exemplary ion spectrum of the sample $Fe(CO)_5$ for a single photon energy, as recorded by the iToF spectrometer detailed in Section 4.1.3 after filtering by pulse energy, subtracting a common background, inverting and averaging the resulting spectra. The mass-over-charge ratios corresponding to the sequential charge states of Fe with 55.845 amu have been marked as a guide to the eye on the logarithmic ToF axis.

Spectra like the one presented in FIG. 11 were measured for the photon energy range of 695 eV to 800 eV and pulse energies ranging from 10% GATT transmission with 600 µJ to 100% GATT transmission with 6 mJ.

After the data treatment described above, the spectra were filtered an additional time by their corresponding photon energy. Spectra were taken for the photon energy range 695 eV to 800 eV with photon energy steps of 3.5 eV. Corrective factors for the signal strength, which are due to varying sample pressure inside the AQS chamber, were applied. They were made necessary as low- and high- pulse energy measurements have vastly different requirements for the sample concentration in the photon-matter interaction region to produce strong, reliable signal while remaining in counting mode. A constant fraction discrimination process with a baseline and threshold value approximating the constant background measured in each run was applied.

The data structure of the measured electron spectra were assembled similarly to those of the ion spectra, as the involved hardware in both sets of measurements was essentially identical

from a data processing point of view. Filtering by XGM was carried out with the same thresholds as for the iToF spectra. Measurements with pulse energies lower than 85% of the average pulse energy were filtered out. Similarly, spectra with pulse energies exceeding 115% of the average pulse energy were filtered out as well. In this way, unified pulse energies during the considered measurements could be guaranteed to the limit of XGM measurement error and slight variations in pointing vector. Spectra were taken for the photon energy range 695 eV to 830 eV with photon energy steps of 3 eV. Pulse energies were varied between 1% GATT transmission with 60 μJ to 100% GATT transmission with 6 mJ. Similar corrective normalization factors as for the iToF measurements, due to variations in sample pressure inside the AQS chamber, were applied if made necessary by the vastly different signal requirements for low- and high- pulse energy measurements.

Calibration for the eToF spectra were carried out using both responses from measurements on Argon, as well as Neon as points of reference. Using the Argon measurements as a first calibration iteration, the eToF time-of-flight axis is converted to a kinetic energy scale.
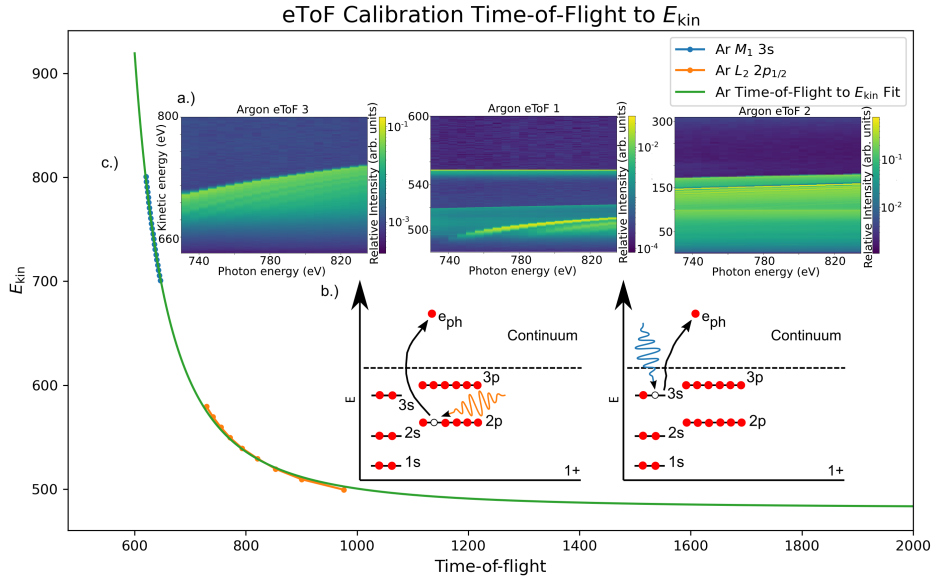
Figure 12: An eToF time-of-flight to kinetic energy calibration for the kinetic energy region of interest for the resonantly excited DCH Auger-Meitner electrons. In a.), the photon energy scans of all three eToFs in the photon energy range of 730 eV to 830 eV are shown. The two illustrations in b.) show the respective photo excitations in Argon that are used to create the calibration shown in c.). This calibration is based on the $3s$ and $2p$ photoelectron traces from an Ar excitation found in the time-of-flight window from eToF 1 (see TABLE 4).

FIG. 12 shows the results of this conversion and the Argon reference spectra that were used to achieve it as well as illustrations of the relevant photo-excitation. As the region of interest established for the detection of $2p^2$ DCH resonant Auger-Meitner electrons in Section 3 is covered by eToF 1 and 4, this kinetic region is of special interest in this work. Nevertheless, similar calibration work was carried out for all eToF spectrometers involved. This also

included an eToF transmission calibration, which was carried out using the Argon $3s$ and $2p$ lines and comparing their transmission to their known absorption cross-sections in the relevant photon energy regime [101]. References for the relevant binding energies were taken from the works of Cardona and Ley, as well as Lablanquie et al. for multiple ionization references [16, 50].

Absolute photon energy calibration was carried out using a photon energy scan from $860\,\text{eV}$ to $885\,\text{eV}$ with neon as a sample. The work of Mazza et al. was used as reference [60]. We measured a deviation of $3\,\text{eV}$ from the values the literature suggests. In the manner discussed above and with the parameters outlined in this section, ion time-of-flight spectroscopy and electron time-of-flight spectroscopy was carried out for two $3d$ metal complex systems: Iron pentacarbonyl ($Fe(CO)_5$), with a characteristic spherical symmetry and ferrocene ($Fe(C_5H_5)_2$), with a characteristic cylindrical symmetry. Their properties, as relevant for the experiment, will be discussed in the following chapter.

For the different analysis steps, a systematic error estimate was carried out and displayed. Wherever appropriate, error bars on the signal intensity scale indicate the estimated error.

The statistical error for both eToF measurements as well as iToF measurements was calculated for each individual measurement point on the time-of-flight axis and the photon energy axis. For any one such bins, counts (number of events) were used to calculate the statistical error. As the number of counts for each observable was large, the appropriate equation for the statistical error is:

$$\varepsilon_{st} = \frac{1}{\sqrt{N}} \tag{14}$$

Here, N represents the number of counts for the respective measurement. Furthermore, wherever pulse energy measurements are used in this work, the full range of pulse energy binning is shown with horizontal error bars to indicate the range of pulse energies used in the respective data point.

For iToF measurements, isotope deconvolution was not considered a major contributing factor. The isotope configuration of the samples could be assumed to contain Fe^{56} as the primary iron isotope. For ferrocene, contributions of other isotopes are relatively small, as implied by the work of Wrackmeyer et al. [100] on the isotopic shift due to Fe^{57} in ferrocene and ferrocene complexes. For iron pentacarbonyl, Wiesli et al. [97] showed that at the 2σ level, there is no significant Fe isotope fractionation between vapor and liquid under conditions thought to reflect equilibrium in iron pentacarbonyl. As no charge states higher than Fe^{14+} were detected, overlap of iron isotopes of high charge states with those of lower charge states could be ruled out as a contributing factor.

Background subtraction of overlapping charge states of differing cationic fragments was not conducted for highly charged cations, such as O^{4+} and C^{3+} with Fe^{14+}. This means that cations without a resonant feature in the photon energy range contribute a uniform background to those measurements in which such an overlap of mass-to-charge ratios occurs. Target density in the interaction region varied however, as measurements at high pulse energies were recorded with different gas pressures than those at low pulse energies. Therefore, both ion and electron yields were normalised to the gas pressure, as measured by an ion gauge in the AQS chamber, in parallel to the data recording.

4.3 Samples

Two $3d$ metal complex samples were investigated during the course of this experiment. The iron environment in iron pentacarbonyl $Fe(CO)_5$ and ferrocene $Fe(C_5H_5)_2$ differ both in bond structure, as well as overall geometry, which enriches the Fe-centered photospectroscopy approach of the study by potentially highlighting molecule specific differences in cationic or DCH-electronic signature.

Relevant chemical and safety information on the two samples was procured from the safety data sheets and specifications sheets provided by the supplier Sigma Aldrich [85, 86].

Data for relevant bond lengths and angles are calculated with GAMESS [6] using density functional theory (DFT) calculations with B3LYP functional and SPK basis set. Thes B3LYP functional was chosen as suitable option for complexes involving heavy elements and has been previously shown by Coriani et al. [18] to give results with excellent agreement for ferrocene and to produce deviations for the metal-carbon distance in that complex of around 2 pm and less for the cyclopentadienyl rings. It was successfully used in time-dependent DFT models to model the ultraviolet and visible light absorption spectrum of ferrocene [78]. With regards to the iron pentacarbonyl sample, the B3LYP functional was previously used by Atkins et al. [38] to produce high-resolution X-Ray absorption spectra of iron pentacarbonyl at the iron K-edge. Reasonable agreement was found with experimental investigations of the sample and the works of Fortes et al. [30] and Bohn et al. [11].

$Fe(CO)_5$ Properties	
CAS Number	13463-40-6
Molecular Weight	195.90 amu
Density	1.49 g/cm^3 at 298.15 K
Phase at STP	Liquid
Appearance	Yellow-Orange
Melting Point	253.15 K
Boiling Point	376.15 K
Vapor pressure	47 hPa at 298.15 K

Table 5: The relevant chemical properties of Iron Pentacarbony $Fe(CO)_5$ as taken from the Specification Sheet and Safety Data Sheet of the sample provided by the distributor Sigma Aldrich. For more information, see [85].

$Fe(CO)_5$ Bond Lengths and Angles	
	Bond Lengths
Fe - C	1.82 Å
C - O	1.16 Å
	Bond Angles
Vertical C - Fe - C	90°
Horizontal C - Fe - C	119.8°

Table 6: Relevant bond lengths of Iron Pentacarbony $Fe(CO)_5$ as calculated by DFT calculations using GAMESS , with the B3LYP functional and the SPK basis set. [6]

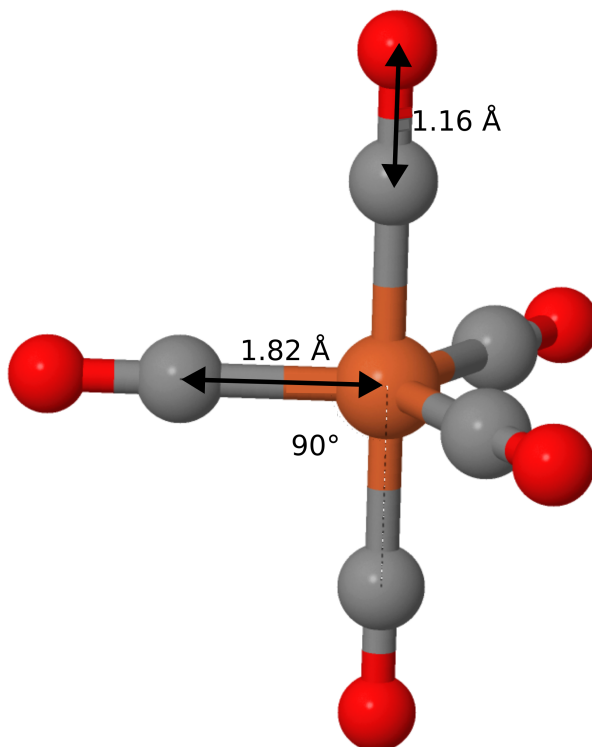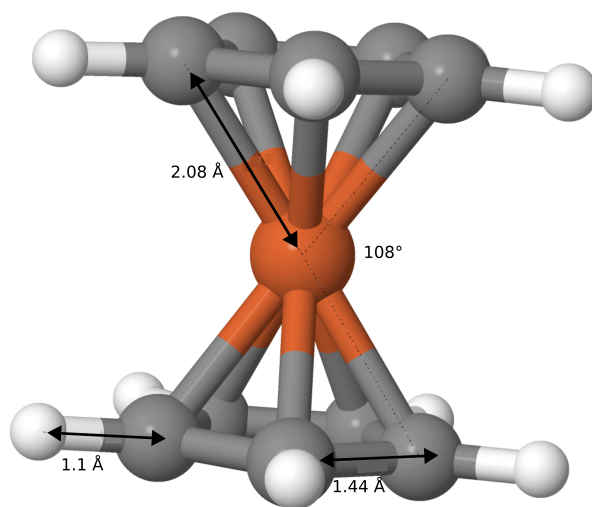Figure 13: A three dimensional visualization of the $Fe(CO)_5$ molecule displaying the relevant molecular geometries.

$Fe(C_5H_5)_2$ Properties

CAS Number	102-54-5
Molecular Weight	186.03 amu
Density	1.49 g/cm^3 at 293.15 K
Phase at STP	Crystalline
Appearance	Yellow
Melting Point	445.15 K
Boiling Point	522.15 K
Vapor pressure	0.1 hPa at 313.15 K

Table 7: The relevant chemical properties of Ferrocene $Fe(C_5H_5)_2$ as taken from the Specification Sheet and Safety Data Sheet of the sample provided by the distributor Sigma Aldrich. For more information, see [86].

$Fe(C_5H_5)_2$ Bond Lengths and Angles

	Bond Lengths
Fe - C	2.08 Å
C - H	1.1 Å
C - C	1.44 Å
	Bond Angles
Vertical C - Fe - C	108°
Horizontal C - C - C	108°

Table 8: Relevant bond lengths of Ferrocene $Fe(C_5H_5)_2$ as calculated by DFT calculations using GAMESS , with the B3LYP functional and the SPK basis set [6].

Figure 14: A three dimensional visualization of the $Fe(C_5H_5)_2$ molecule displaying the relevant molecular geometries.

5 X-Ray Absorption Spectra of Fe Complexes

Having a detailed understanding of the experimental setup used, this chapter is going to focus on the product cation data obtained from the X-Ray absorption ion spectroscopy. A careful analysis of the various product cation traces at increasing pulse energies reveals an increase in multiply charged iron cations, as well as an increase in resonance energy for the corresponding XAS resonances.

As described in Section 4.1.3, the vertical eToF shown in FIG. 9b, was used in the iToF configuration of the AQS end chamber in this experiment to obtain ion spectra of the two samples $Fe(CO)_5$ and $Fe(C_5H_5)_2$. Spectra were taken over the photon energy range of $680\,eV$ to $800\,eV$ in $3.5\,eV$ steps with the bandwidth given as 1% of the photon energy (FWHM), resulting in an estimated bandwidth of $6.80\,eV$ to $8.00\,eV$ over the course of the measured spectra. These photon energy scans were repeated for both samples at GATT percentages of 100%, 50%, 25% and 10%, corresponding to an average X-Ray pulse energy of $6000\,\mu J$, $3000\,\mu J$, $1500\,\mu J$ and $600\,\mu J$, as measured by the XGM directly after the GATT, but before the further transmission losses of the beamline closer to the experimental hutch. Pulse energy was also measured post interaction zone via the SQS XGM. Pulse energies measured by the XGM in the SQS instrument yielded fractions of this GATT transmitted average pulse energy, with pulse energies measured between approximately $600\,\mu J$ and $3670\,\mu J$. This incorporation of not one, but two separate GMD measurements into the analysis of the measurements is in accordance with the works of Baumann et al. who in their studies on the transmission of pulse energy to the SQS instrument attested a 50% to 80% transmission of pulse energy, depending on the mirror configuration [8].

Following the data processing described in Section 4.2, the acquired spectra were filtered by their associated photon- and pulse-energy. Pulses with energies smaller or larger than the average pulse energy $\pm 15\%$ of the average pulse energy were filtered out to guarantee as uniform a pulse energy as possible during the measurements. The resulting pulses were averaged and a uniform background was subtracted. This background was integrated over the 500 channels with the slowest flight times of the spectra, as said area was unaffected by signal in the iToF configuration.

The resulting spectra provide a map of the cationic fragments of the high intensity photon-matter interaction with the two samples $Fe(CO)_5$ and $Fe(C_5H_5)_2$. In a next step, the relevant cationic product channels are here checked for resonant behavior and signal dependency on pulse energy, which aids in understanding high intensity ionization processes in these samples. This knowledge aids not only in finding the experimental signatures of potential DCH cation product fragments, but also allows for a very good overview of the potential cationic targets present during a DCH excitation at a given photon energy and pulse energy, with only the specific relative makeup of cationic targets overlapping on the same mass-over-charge ratio remaining obscure. This information of the potential cationic targets is particularly useful when trying to separate SCH from DCH contributions in electron spectra. Incorporating the deviations of cation fragment production over the range of two orders of magnitude to high intensity irradiation on the scale of $3672.5\,\mu J$ into the study of DCH processes in the two studied samples follows some of the methods outlined in the work of Koulentianos et al. on DCH processes in formamide [43]. Their approach is extended in this work using the ability

to scan the photonenergy at the European XFEL, which allowed for these measurements to be conducted over the range of the cationic resonances of the iron L-edge.

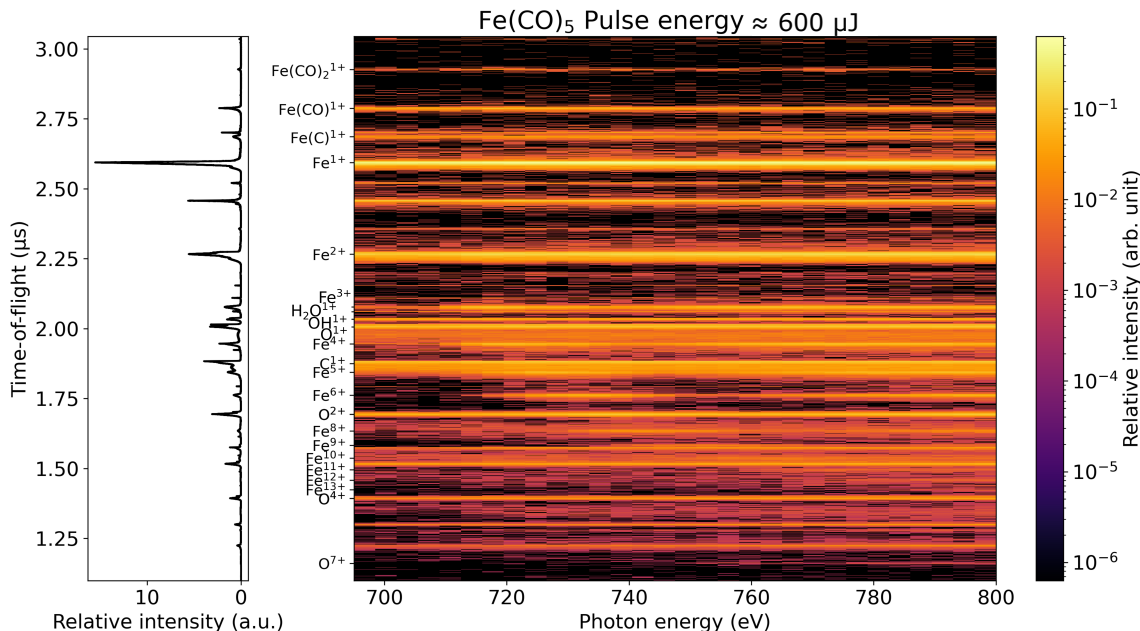## 5.1 X-Ray Absorption Ion Spectra of Iron Pentacarbonyl

Figure 15: The photon energy scan of ion spectra taken of the sample $Fe(CO)_5$ for the photon energy range 695 eV to 800 eV, as recorded by the iToF spectrometer detailed in Section 4.1.3. Ticks for the cationic Fe charge states and other cation species have been added on the time-of-flight scale. GATT transmitted intensity was 10% of maximum requested energy with pulse energies measured by SQS GMD from approximately 600 μJ to a peak pulse energy of approximately 690 μJ. Some product cations, particularly Fe charge states of 3+ and higher, show identifiable resonances in the photon energy scan, that tend towards increasing photon energies with increasing charge state.

FIG. 15 shows the $Fe(CO)_5$ X-Ray absorption ion spectrum taken at the lowest pulse energy settings with a lower limit pulse energy of approximately 600 μJ, in which a clear trace of the Fe^+ cation can be found as the most intensive signal. Traces of four fragments with mass-over-charge ratios larger than that of Fe can be found at this pulse energy level. They correspond to the ratios associated with $Fe(CO)_2^+$, $Fe(CO)^+$ and $Fe(C)^+$. An additional fifth trace at a slightly longer time-of-flight hints at some slight contamination within the chamber, as it corresponds to a mass-over-charge ratio corresponding to 70 amu/e. According to Godehusen et al. [32], the three identified larger fragments are the most common large fragments associated with a photon-matter interaction at the L-edge involving iron pentacarbonyl. Each shows slightly resonant behavior in the region around the 718 eV threshold.

Looking at the fragments with mass-over-charge ratios smaller than the Fe^+ cation, the Fe^{2+} cation trace with mass-over-charge ratio corresponding to 28 amu/e is also clearly visible, yet does not show a clearly visible resonance feature, possibly because it overlaps with the trace of the much stronger CO^+ cation line. The representation of FIG. 15 does not lend itself for the identification of resonances in these two cations, but similar approaches were equally unsuccessful in revealing such a feature. The Fe^{3+} cation, however, can be recognized by its L-edge resonance. Both O^+- and OH^+-cation trace can be found, yet do not show an identifiable resonance in this representation. The observation that Fe cations can be identified by their L-edge resonances holds similarly true for the Fe^{4+} cation. The C^+ cation, which can be seen as well, shows resonant behavior that suggests a similar resonance energy as the Fe^{5+} and Fe^{6+} cation found at slightly lower time-of-flight channels. The trace of the Fe^{7+} charge state at the time-of-flight associated with mass-over-charge ratio 8 amu/e does not immediately show such a resonance, which is partly due to its shared time-of-flight channel with the seemingly stronger O^{2+} cation. The Fe^{8+} cation can be identified by resonant behavior and is the most highly charged Fe cation accessed in these experimental conditions. The C^{2+} cation signal appears rather weak before the threshold of 718 eV, but can be clearly identified at higher excitation energies. Both O^{3+} and O^{4+} are present, both without identifiable resonant behavior. Furthermore, the O^{4+} cations overlap with the time-of-flight channel of the C^{3+} cation.

FIG. 16 shows the spectra collected over the same photon energy range (695 eV to 800 eV) at higher pulse energies, specifically from approximately 780 µJ to a peak pulse energy of 890 µJ. FIG. 16 differs from FIG. 15 most notably in the higher signal intensity across all traces. The higher pulse energies result in the appearance of new cation fragment traces. New traces appear in the spectrum, for one, with Fe cation charge state traces appearing for more highly charged cations in ever shorter time-of-flight channels. In FIG. 16, the signal trace corresponding to the time-of-flight associated with the Fe^{8+} cation becomes much clearer. Signal traces at time-of-flight channels associated with Fe^{9+}, Fe^{10+}, Fe^{11+} and Fe^{12+} can also be identified. The correspondence between signal trace and responsible cation can be easily verified for these traces, as their strong resonance within the L-edge excitation energy region in the photon energy scan identifies them clearly as Fe cations.

FIG. 16 also reveals some overarching trends in the $Fe(CO)_5$ fragments. The cationic series of fragments associated with the iron core of the molecule is extended toward higher charge states, which implies a sequential ionization and Auger-Meitner cascade, due to the stronger irradiance combination of the short pulse duration of the X-Ray pulse and its increased intensity. These higher charge states, starting at Fe^{3+} all the way to the low-signal trace of Fe^{12+}, all show two areas of higher signal. The first of these is an X-Ray absorption resonance, while the form and position on the photon energy scale of the second implies that the Fe L-edge was passed. Both signal shifts increase towards higher photon energies, as more highly charged cations are considered. Starting with the Fe^{10+} cation trace, the ionization edge that can be identified for Fe^{9+}, falls outside of the scanned region, showing only the pre-edge absorption resonance within the bounds of the experimental conditions.

FIG. 17 shows the iToF spectra in the photon range 695 eV to 800 eV with a pulse energy of approximately 1890 µJ as measured by SQS GMD. FIG. 17 shows a continuation of the trends established in FIG. 15 and FIG. 16. Inspection of the Fe cation traces reveals the Fe^{13+} cation by its resonance that starts at 770 eV. This resonance emerges, in line with previously
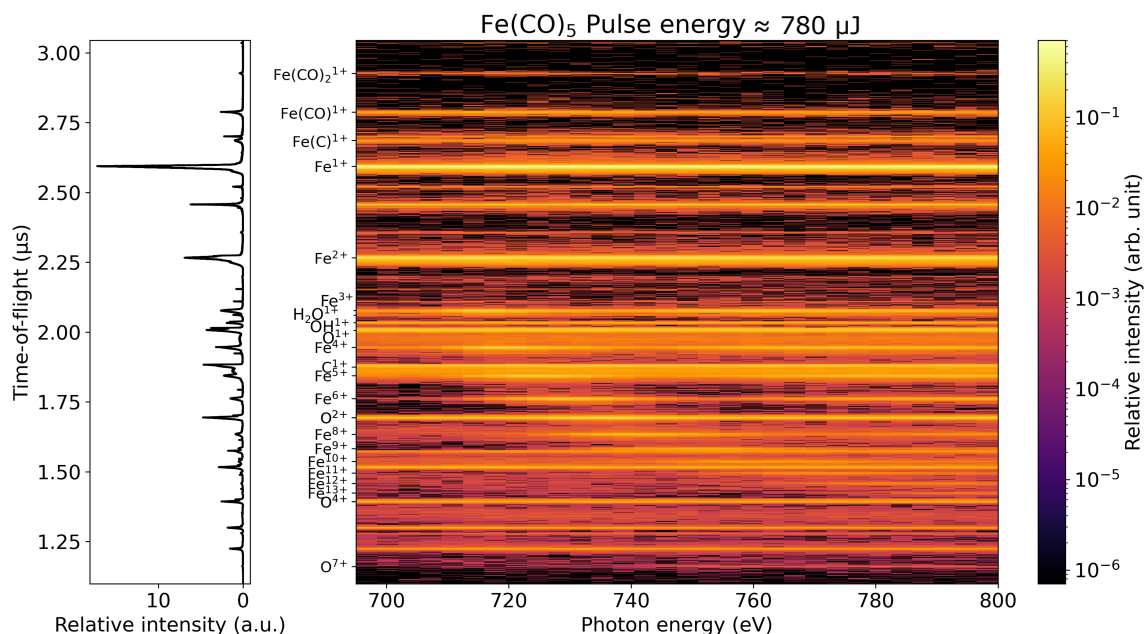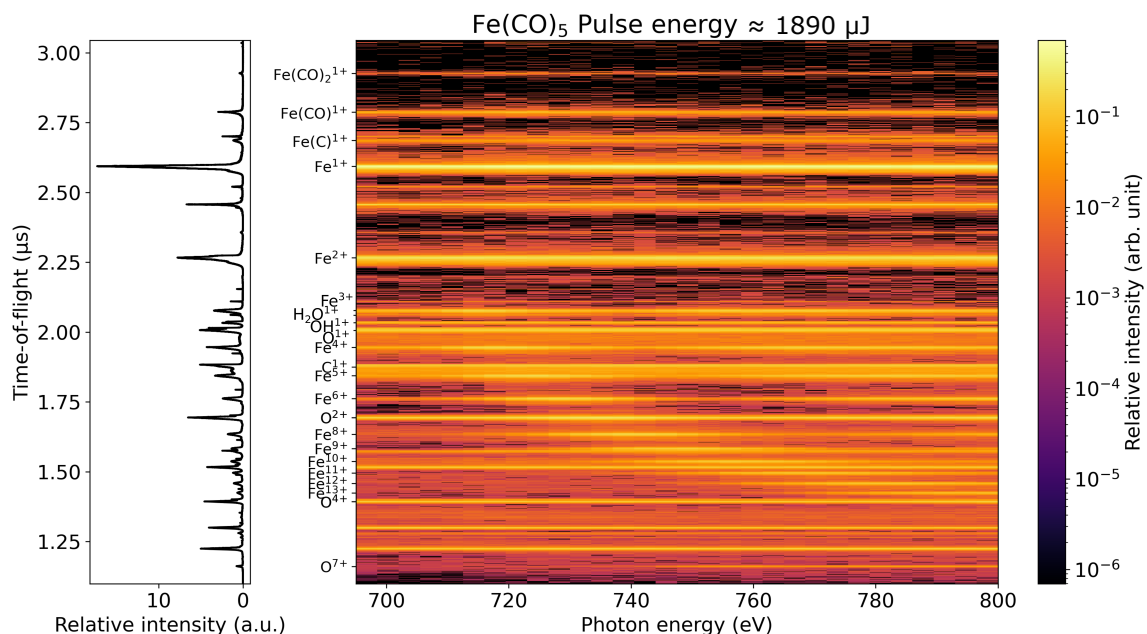
Figure 16: The collection of ion spectra taken of the sample $Fe(CO)_5$ for the photon energy range 695 eV to 800 eV, as recorded by the iToF spectrometer detailed in Section 4.1.3. Ticks for the cationic Fe charge states and other cation species have been added on the time-of-flight scale. GATT transmitted intensity was 25% of maximum requested energy with pulse energies measured by SQS GMD ranging from approximately 780 µJ to 890 µJ. The onset of the resonances of the Fe charge states of 3+ and higher are more pronounced and the cations contribution to the ovearall ion yield increases.

established trends, at a higher photon energy than its counter part of lower charge state Fe^{12+}. Extrapolating from this pattern, one can see small increases in the signal with time-of-flight corresponding to O^{4+} and C^{3+}, where one would expect a resonance of Fe^{14+} to overlap with the signal due to the other two cations.

Signal for all other measured fragments increased further compared to lower pulse energies and the resonance in the $Fe(CO)_2^+$ signal is more evident. Furthermore, the high pulse energies measurements show some of the higher charge states that were previously only accessed on-resonance, meaning no signal was detected outside of the relatively narrow photon-energy range for which the resonance was seen, to be present with small signals pre- and post-resonance.

A new signal with mass-over-charge ratio corresponding to $\frac{16}{7}$ amu/e was detected at these pulse energies (approximately 1890 µJ to 2180 µJ). Its mass-over-charge ratio implies a highly charged oxygen cation being created during the interaction. The onset of this signal around 744 eV at a mass-over-charge ratio corresponding to the O^{7+} cation shows helium-like oxygen as a product of the high pulse energy measurement. This signal is absent in the measurements at lower pulse energies. The signal strength of this exotic fragment is evidence for it stemming
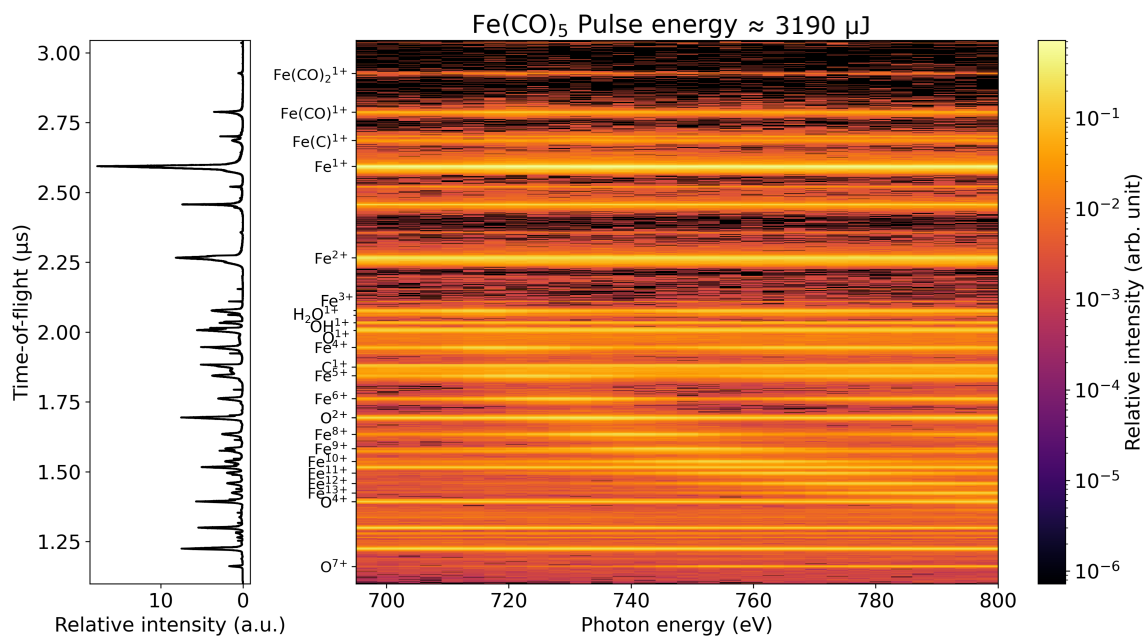
49
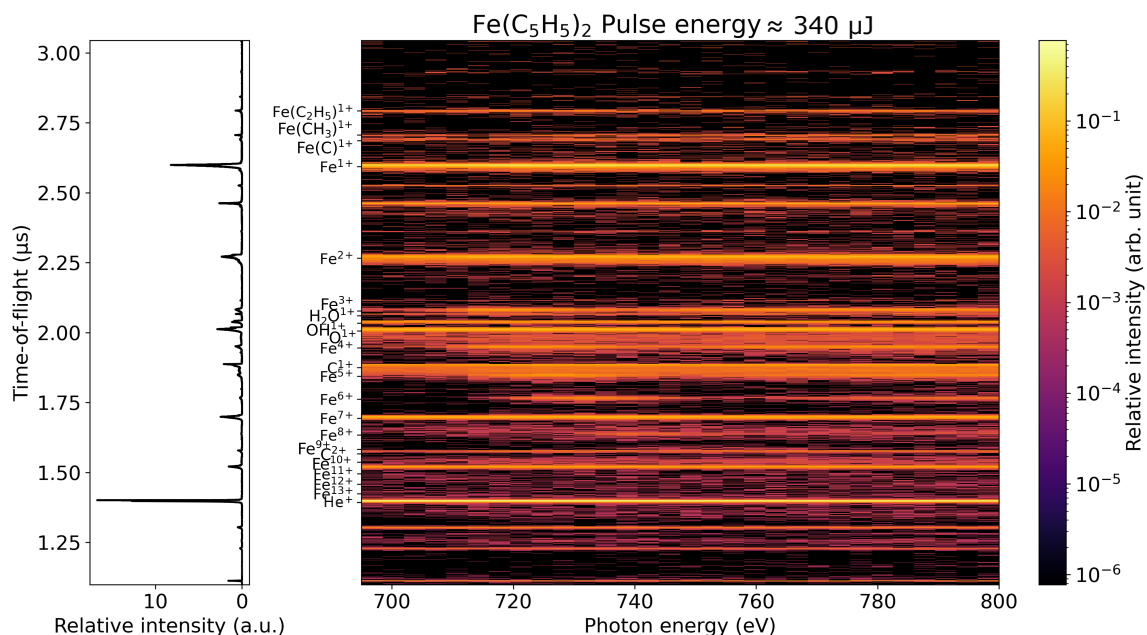
Figure 17: The collection of ion spectra taken of the sample $Fe(CO)_5$ for the photon energy range 695 eV to 800 eV, as recorded by the iToF spectrometer detailed in Section 4.1.3. Ticks for the cationic Fe charge states and other cation species have been added on the time-of-flight scale. GATT transmitted intensity was 50% of maximum requested energy with pulse energies measured by SQS GMD ranging from approximately 1890 μJ to 2180 μJ. The resonances of the Fe charge states of 3+ and higher are clearly pronounced and the 'stepwise' increase in resonance energy is quite apparent.

from a photon-matter interaction with iron pentacarbonyl. The fragment's resonant emergence at 740 eV point at the involvement of non-linear processes in that photon energy region playing an important role in enabling its creation. This observation verifies the experimental setup's capability to deliver the required pulse energies at the necessarily short pulse duration to the interaction zone to observe the non-linear regime.

FIG. 18 shows the iToF spectra of $Fe(CO)_5$ for the photon energy range 695 eV to 800 eV and pulse energies ranging from approximately 3190 μJ to 3670 μJ. Comparing FIG. 18 to FIG. 17, one can see clearly the increased signal intensity of iron pentacarbonyl fragments that comes along with the maximum of the pulse energies in this experiment. In this figure, all signal traces that were present in the previous measurement can also be identified. The previously identified Fe^{14+} cation resonance has a stronger signal in this experimental configuration, as well. Despite higher pulse energy, no trace associated with Fe^{15+} was found, making 14 the highest detected charge in Fe cation fragments for this experiment and the $Fe(CO)_5$ sample.

The onset of the O^{7+} signal occurs at 740 eV at this pulse energy setting, which further implies the dependence of the creation of this fragment on not only the photon energy, but

50

Figure 18: The collection of ion spectra taken of the sample $Fe(CO)_5$ for the photon energy range 695 eV to 800 eV, as recorded by the iToF spectrometer detailed in Section 4.1.3. Ticks for the cationic Fe charge states and other cation species have been added on the time-of-flight scale. GATT transmitted intensity was 100% of maximum requested energy with pulse energies measured by SQS GMD ranging from approximately 3190 µJ to 3670 µJ. The contribution of higher Fe charge states, with clearly identifiable resonances at this intensity, makes up a significant portion of the total ion yield.

also the pulse energy.

5.2 X-Ray Absorption Ion Spectra of Ferrocene

Figure 19: The collection of ion spectra taken of the sample $Fe(C_5H_5)_2$ for the photon energy range 695 eV to 800 eV, as recorded by the iToF spectrometer detailed in Section 4.1.3. Ticks for the cationic Fe charge states and other cation species have been added on the time-of-flight scale. GATT transmitted intensity was 10% of maximum requested energy with pulse energies measured by SQS GMD ranging from 340 μJ to 390 μJ. The scan shows persistent Fe^{1+} trace, but an even stronger persistent He^{1+} trace. Small contributions of highly charged Fe cations can also be found.

FIG. 19 shows the $Fe(C_5H_5)_2$ X-Ray absorption ion spectrum for the photon energy range 695 eV to 800 eV and pulse energies ranging from 340 μJ to 390 μJ. In this spectrum, a clear trace at the previously established time-of-flight associated with C^{3+} and He^{1+} cations is found as the most intensive signal, overlapping with the marked signal trace for the mass-over-charge ratio associated with Fe^{14+}. Traces of two fragments with mass-over-charge ratios larger than that of Fe^+ can be found at this pulse energy level. They correspond to the time-of-flight channels associated with $FeC_2H_5^+$ and $FeCH_3^+$. The $FeCH_3^+$ signal is accompanied by several traces with resonant features of $FeCH^+$ and FeC^+. Similarly to what was observed in the iron pentacarbonyl sample, an additional trace at the equivalent of 70 amu/e was found present in the spectrum, but whether this remains the contaminant detected in other measurements, or is indeed associated with $Fe(CH_2)^+$, remains to be investigated in future works. According to the work of Godehusen et al.[32], $FeC_2H_5^+$ and $Fe(CH_3)^+$ are expected fragments after an L-edge excitation of ferrocene. Each shows resonant behavior.

The signal at mass-over-charge ratio associated with 56 amu/e shows a resonance between

720 eV and 730 eV. Looking at the fragments with mass-over-charge ratios smaller than the Fe^+ cation, the Fe^{2+} cation trace with mass-over-charge ratio associated with 28 amu/e is clearly visible, and, contrary to its appearance in the measurements on iron pentacarbonyl, shows resonant behavior in the region around 720 eV. The Fe^{3+} cation can be recognized by its L-edge resonance at 720 eV, just as it was for the iron pentacarbonyl. Two traces at mass-over-charge ratios associated with the O^+- and OH^+-cation trace can be found, suggesting a water contamination of the chamber. Indeed, a faint trace of H_2O^+ can be seen just below the Fe^{3+} line. This suggests the main source of contamination in the chamber for both samples as it also matches the observations in iron pentacarbonyl. The previously observed Fe cation L-edge resonance series continues for the Fe^{4+} cation. The C^+ cation shows resonant behavior at similar resonance energies as the Fe^{5+} and Fe^{6+} cation found at slightly longer time-of-flight channels. The trace of the Fe^{7+} charge state at mass-over-charge ratio associated with 8 amu/e shows a small resonance between 730 eV and 740 eV, despite its time-of-flight channel being shared with the O^{2+} cation. The Fe^{8+} cation can be identified by resonant behavior and is the highest Fe charge state accessed in measurements at this pulse energy. The C^{2+} cation signal appears rather weak before the threshold of 718 eV is crossed, but can be clearly identified afterward. A signal trace that is identified as O^{3+} is readily apparent in the spectrum just below the Fe^{10+} marker. The most intensive signal trace in the spectrum is found at the time-of-flight associated with a mass-over-charge ratio of 4 amu/e. This includes He^+, Fe^{14+}, O^{4+} and C^{3+} as potential sources, where Fe^{14+} can be safely discarded as a potential source as the charge states between Fe^{14+} and the highest verified iron charge state Fe^{8+} are absent in the spectrum. The spectrum shows no resonant feature during the photon energy scan, which means both remaining sources O^{4+} and C^{3+} are viable candidates, but likely out-scaled by the cationic trace of the helium carrier gas. A faint trace that can be attributed to O^{5+} can also be seen.

FIG. 20 shows the iToF spectra of the sample $Fe(C_5H_5)_2$ for the photon energy range 695 eV to 800 eV, for the pulse energies ranging from approximately 890 µJ to 1020 µJ. FIG. 20 differs only slightly from FIG. 19. The onset of the Fe^{3+} resonance is much stronger in signal and suggests a slightly lower photon energy than was previously suggested. The resonances of higher iron charge states emerge step-wise, similar to the observations in iron pentacarbonyl, and correct the onset of each resonance towards slightly lower photon energies than was suggested in FIG. 19. The most notable difference in this measurement is the detection of resonant iron charge states of Fe^{n+}, with $n = 9 : 13$ at this intensity, higher charge states than were observed in FIG. 19. The sample thereby accesses a higher iron charge state at this intensity than the iron pentacarbonyl does at comparable experiment conditions and pulse energies. The resonances for these higher charge states themselves also differ somewhat in photon energy from the measurements in iron pentacarbonyl, as they tend towards photon energies a few eV higher than what was measured in iron pentacarbonyl.

Inspecting FIG. 21 and comparing the measurement results to lower intensity results further emphasizes the accessibility of high iron charge states at high pulse intensities. While the results show virtually no difference to FIG. 20 in most cationic species, the iron cations Fe^{n+} with $n = 10 : 13$ all show a significant increase in signal strength relative to the other detected cationic fragments.

Another significant difference in this measurement is the detection of a resonantly emerging
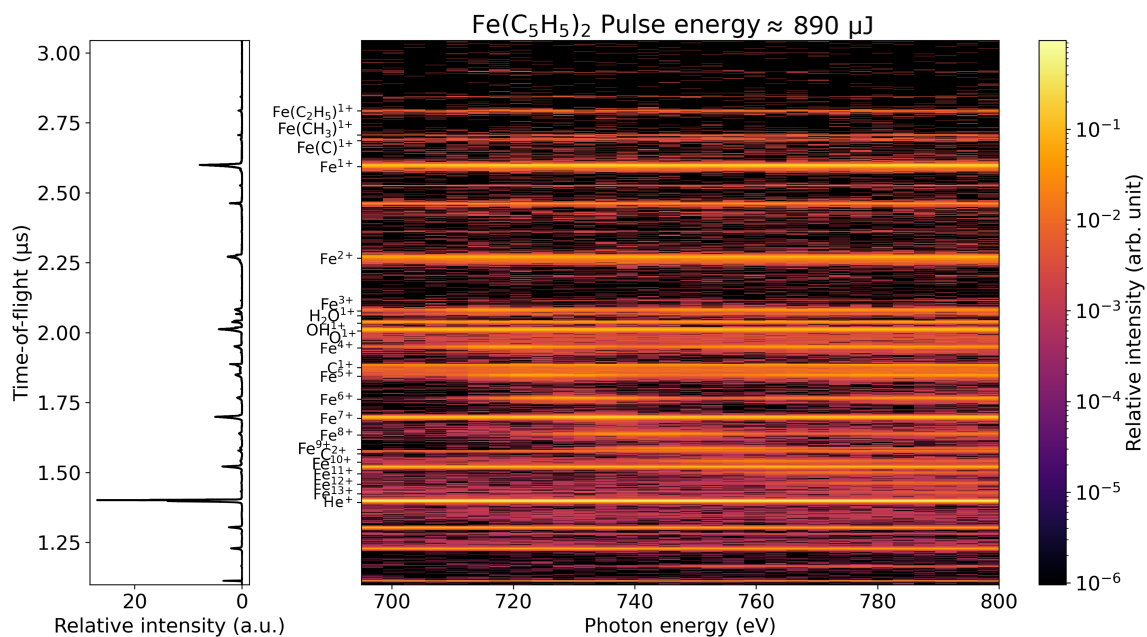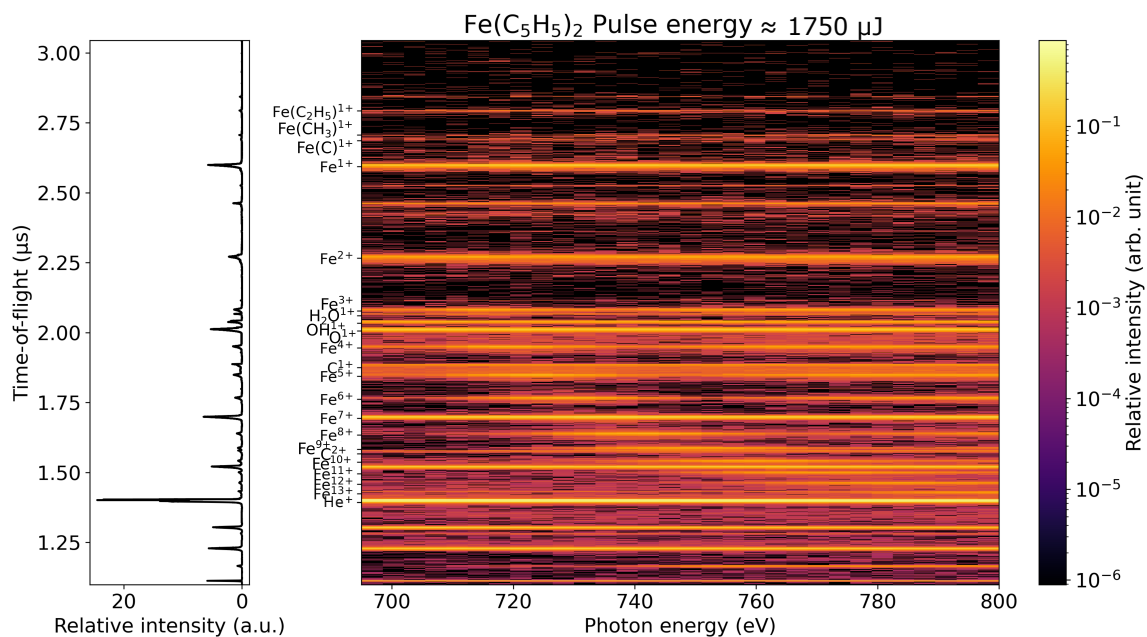
Figure 20: The collection of ion spectra taken of the sample $Fe(C_5H_5)_2$ for the photon energy range $695\,eV$ to $800\,eV$, as recorded by the iToF spectrometer detailed in Section 4.1.3. Ticks for the cationic Fe charge states and other cation species have been added on the time-of-flight scale. GATT transmitted intensity was 25% of maximum requested energy with pulse energies measured by SQS GMD ranging from approximately $890\,\mu J$ to $1020\,\mu J$. Resonances of Fe cations of charge state $3+$ and higher can be idetified by their resonances, which tend towards higher onset photon energies as the charge increases.

signal that can be associated to the mass-over-charge ratio of O^{7+}. The detection of this cation at this intensity lends support to the hypotheses of a sequentially ionized contaminant which was posed earlier in the context of the iron pentacarbonyl results. A corollary of this is the presence of similar contamination within the AQS chamber during both measurements, which for one does not inhibit the quality of the vacuum, but does, on the other hand, contribute enough oxygen to the interaction region to sequentially ionize and be detected in sufficiently large count rates to surpass any uniform background correction. H_2O is a candidate for this background contaminant, as its cation trace can be found in spectra of both samples.

FIG. 22 shows the results of the ferrocene measurement at the maximum reached pulse energy. In comparing this measurement to the results of measurements at lower pulse energies, we find some strong differences in the appearance of the iron cations and their resonances. For the signal traces associated with the mass-over-charge ratios of the cations Fe^{n+}, with $n = 1 : 9, 12, 13$, the traces appear throughout the spectrum, at photon energies below- as well as above the respective resonances. While this is the case in the other measurements for ferrocene, as well for Fe^{1+} and Fe^{2+}, it was not observed for Fe^{n+} with $n = 3 : 9, 12, 13$. This mimics the behavior of the cationic iron charge states for the iron pentacarbonyl measurements
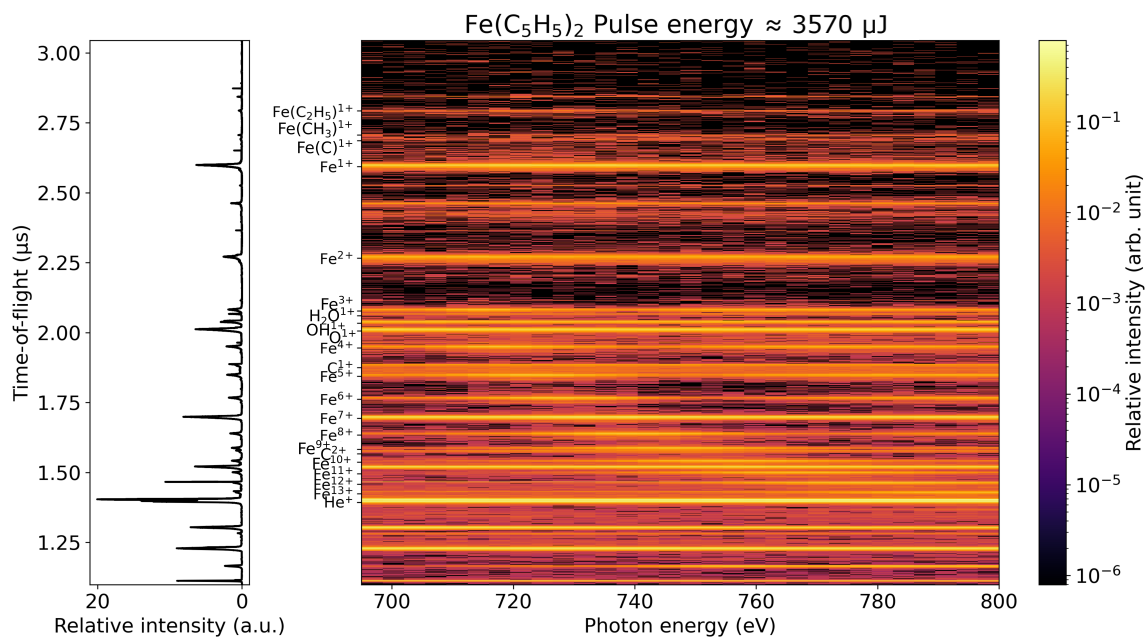
54

Figure 21: The collection of ion spectra taken of the sample $Fe(C_5H_5)_2$ for the photon energy range 695 eV to 800 eV, as recorded by the iToF spectrometer detailed in Section 4.1.3. Ticks for the cationic Fe charge states and other cation species have been added on the time-of-flight scale. GATT transmitted intensity was 50% of maximum requested energy with pulse energies measured by SQS GMD ranging from approximately 1750 µJ to 2010 µJ. The increase in signal strength for highly charged Fe cations is apparent. The resonances of these cations, which tend towards higher photon energies with higher charge states, contribute to the higher ion yield.

at high pulse energies. With iron pentacarbonyl as target, it was the sequence of Fe^{n+} with $n = 3 : 10$, which became more apparent at pre-resonance photon energies. With ferrocene as target, the cations Fe^{12+}, and Fe^{13+} show this behavior as well, linking the emergence of highly charged iron cations to particularly intense pulse energies. The apparent gap in the sequence of ever higher emerging charge states symbolized by the Fe^{10+} and Fe^{11+} cation in this ferrocene measurement are the exception to this trend.

Figure 22: The collection of ion spectra taken of the sample $Fe(C_5H_5)_2$ for the photon energy range 695 eV to 800 eV, as recorded by the iToF spectrometer detailed in Section 4.1.3. Ticks for the cationic Fe charge states and other cation species have been added on the time-of-flight scale. GATT transmitted intensity was 100% of maximum requested energy with pulse energies measured by SQS GMD ranging from 3570 μJ to 4100 μJ. The product cation's ion yield is significantly increased for Fe cations with more charge. Their contribution makes up a large part of the total ion yield and is amplified by the strong signal from their respective resonances.

6 DCH Ion Spectroscopy of Fe Complexes

Having found increasing differences in cation production pathways for increasing pulse energies, this chapter will compare the various ion yields for iron cations of increasing charge across pulse energies to reveal the influence of DCH processes not only in the sample, but also the product iron cations.

6.1 L-edge Resonances of Multiply Charged Iron Cation Fragments after Intense X-Ray Excitation in Iron Pentacarbonyl and Ferrocene

The previous section introduced the observation of multiply charged iron cations as the product of an ultrashort, intense photon-matter interaction for the targets iron pentacarbonyl and ferrocene. The resonant behavior of these iron cations and particularly deviations and shifts in their position on the photon energy scale informs the identification of regions where the creation of double core-holes influences the decay channels and the cationic fragmentation products. They also provide insight into the sequential ionization of the Fe center of the two $3d$ metal complex molecules studied. Comparing these experimental results with the theoretical X-Ray absorption spectra of isolated iron cations presented in Section 3 and the single-photon ionization results of others in the field serves as a normative reference for this evaluation.

FIG. 23 shows the integrated iron cation signals over small time-of-flight regions for charge states 1 through 14, extracted from the measurements shown in FIG. 15, FIG. 16, FIG. 17 and FIG. 18. On first inspection, the strong disagreement between the theoretically predicted resonances for the XAS of an isolated iron atom and the experimentally measured ion yields of iron pentacarbonyl into the Fe^+ channel for all intensities is apparent, yet unsurprising, as the work of Godehusen et al. [32] suggests a shift towards higher photon energies in the absorption of iron pentacarbonyl compared to the isolated iron atom. On closer look, however, the measurement also disagrees with the findings of Godehusen et al. [32] regarding the measurement of the $Fe(CO)_5 \longrightarrow Fe^+$ channel, in terms of resolution capability. In their work, Godehusen et al. measure a strong L-edge resonance in this fragmentation channel for photon energies of $710\,eV$, which is not resolved in our measurement, as per the resolution and bandwidth of the experiment. Some agreement is preserved, however, between this work and the measurements of Godehusen et al. for the two resonances starting at $720\,eV$. By also contrasting this observation with the results of Schippers et al. [80] on L-edge XAS of singly charged iron cations, the impact of charge transfer to the ligands becomes apparent. Where Godehusen et al. found a strong production of singly charged iron in the molecule, Schippers et al. observe that single, double and even triple ionization of the singly charged iron cation have very similar cross-sections. The implication of additional charge being transferred to the ligands in the molecule before coulomb explosion is reflected in the strong production of Fe^{1+} in this experiment.

For the cation charge states Fe^{n+}, with $n = 2 : 9$, remarkable good agreement is found between the predicitons of resonance photon energies of the isolated iron atom model and the measured resonances for the product fragmentation channels associated with each cation,
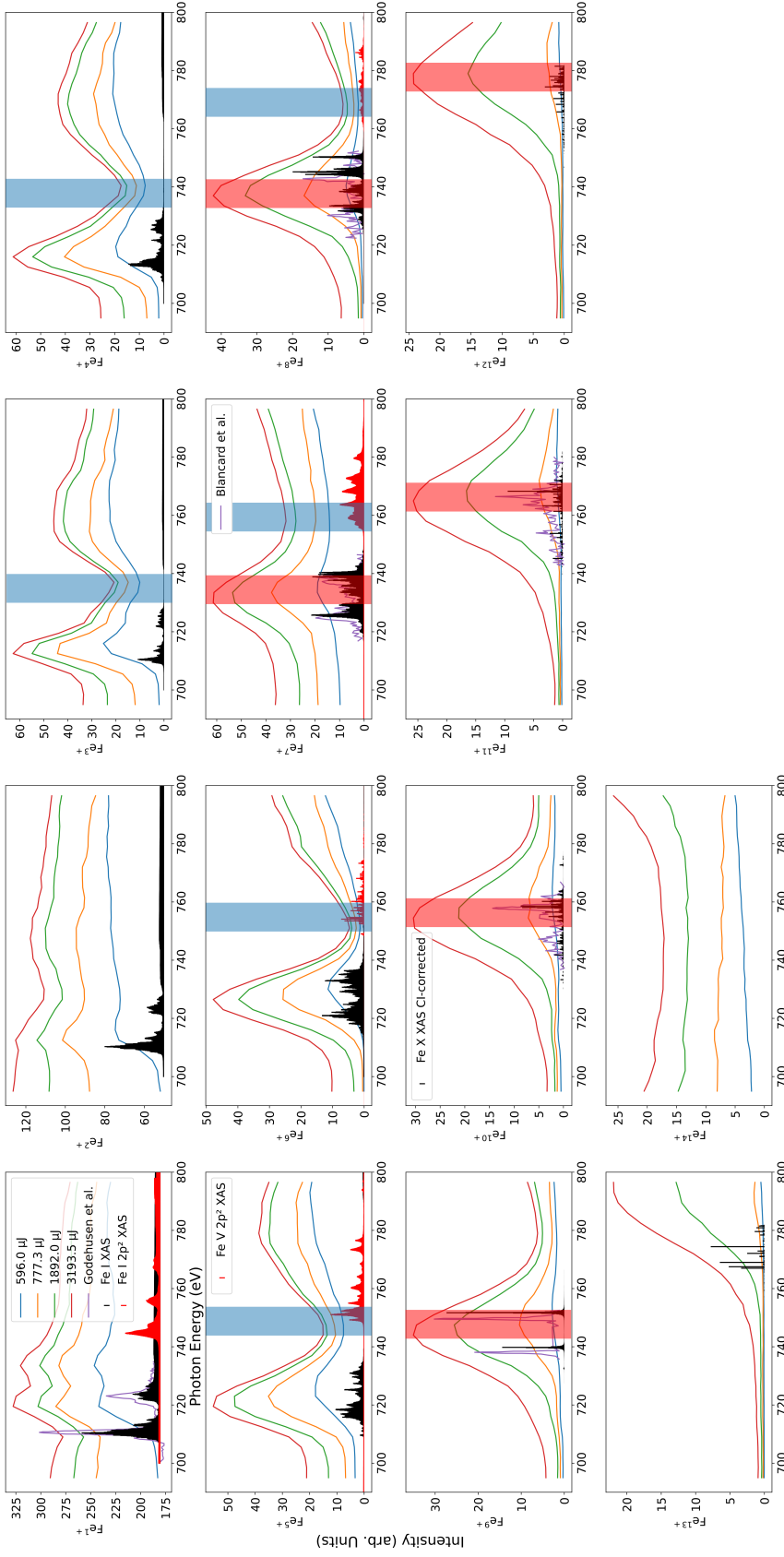
Figure 23: The collection of iron cation signals taken of the sample Fe(CO)$_5$ for the photon energy range 695 eV to 800 eV, as recorded by the iToF spectrometer detailed in Section 4.1.3 for the transmitted intensity percentages of 10%, 25%, 50%, and 100%. The integrated signal is compared to the results for isolated iron cations outlined in Section 3 and to the experimental single photoionization results of Godehusen et al. and Blancard et al., respectively [10, 32]. Regions of 10 eV, associated with uncharacteristically large signal depletion for high pulse intensities at photon energies not connected to known SCH-resonances of the respective charge state have been marked in blue. Contrast with the resonance maxima marked in red reveals evidence for an effective pumping mechanism into resonances of charge states of 4 additional charges for Fe^{n+} ($n = 2-5$). For Fe^{n+} ($n = 6-7$), the overlap of signal depletion and resonance suggests and the accumulation of 3 additional charges instead.

58

despite some mass-over-charge ratios overlapping with cations of different product fragments. The notable exception lies in the rising ionization edge in each channel, which is not well mapped in the model considerations.

This adherence to the isolated cation model offers some insight into the production channels of the cations in question. The agreement between the model and these results suggest the relevant cation fragments to be the product of sequential ionization or Auger-Meitner cascade relaxation effects occurring in the $Fe^{(n-1)+}$ cation for $n = 2 : 9$ within the interaction region, where each step occurs within the bounds of the single core-hole processes accounted for by the model. While the resonance position offers no hint at double core-hole processes playing a role in their formation when compared to the resonance positions predicted by the isolated cation model, the comparison shows a trend in resonance maxima towards lower photon energies for high pulse energy measurements in the cations Fe^{5+} and those more highly charged. Furthermore, a 'bleaching effect' (marked in blue) is notable in cations Fe^{3+} and those more highly charged. In these regions, the ion yield intensity drops below the expected offset between low intensity and high intensity measurements.

The effect can be observed in all cationic resonances at the same relative position: In the right flank of the resonance signal, relative intensity decreases drastically. This effect is strongest for the cations Fe^{n+}, with $n = 3 : 6, 8$, but also somewhat present for the iron cations of higher charges and those encumbered with a background signal that was assigned to a different product cation species. This 'bleaching' effect decreases the relative intensity unevenly across the different measured intensities. For the measurements associated with 10% GATT transmitted pulse energies, no such effect can be observed in the recorded spectra to the degree that both flanks of the resonance appear at the same intensity. For the three higher pulse energy categories though, the effect is not only present, but also increases continuously in strength with increasing pulse energies. For example, this means that for 100% GATT transmitted pulse energies, the signal in the right flank of the resonance is almost as low as the signal for 50%, 25% and 10% GATT transmitted pulse energies. Even when assuming a merely linear rise in signal intensity for these photon energy regions and a quadratic rise for on-resonance measurements, the intensity observed at these energies falls short for these pulse energies.

Turning the focus again toward the resonance positions of the multiply charged iron cations, for the cation charge states Fe^{n+}, with $n = 10 : 14$, agreement between the isolated iron atom model and the experimental results of the iron pentacarbonyl measurement vanes. As the iron cation is continuously ionized, more and more electrons are stripped from it. For the charge state Fe^{9+} in this model, the ionization process involves not only the $3d$ electronic shell, but also electrons of the $3p$ shell. The isolated atom model in use here diverges to significantly higher resonance energies for this and higher charge states. This can be ameliorated by including more accessible states, thereby correcting for configuration interaction for these charge states. The resulting, CI-corrected model, can be compared to the experimental and theoretical results of Blancard et al. [10] in their work on single-photon ionization resonance energies of multiply charged iron atoms. Thus, the corrected values that are in good agreement with the experimental results of previous single-photon ionization experiments were used in FIG. 23 to model the absorption cross-section of charge states Fe^{9+} and higher (Fe^{10+} in the figure). The shape of the corresponding resonances is accurately predicted by the model. De-

spite this general resemblance, the resonance maxima at higher pulse energy measurements diverge from this prediction, mostly to lower photon energies.

This observation is akin to most multiply charged iron cations included in FIG. 23, but most observable for iron cation products Fe^{5+} and those more highly charged. The shifts of resonance maxima with increased intensity to lower photon energies are not expected in a purely single-photon ionization based model. These observed shifts are several eV large for some cations and tend toward lower photon energies for larger pulse energies. Despite these shifts falling within the estimated photon energy bandwidth of 7 eV of this experiment for many cations, for Fe^{10+} and more highly charged cations, the difference between the resonance maximum at 340 µJ and 3570 µJ exceeds the bandwidth. The continuous trend of this observation in relation to the pulse energy of the respective measurement is notable.

The iron cations Fe^{n+}, with $n = 2 : 9$ and those of the iron cations Fe^{n+}, with $n = 10 : 14$ furthermore show a difference in relative fragment channel intensity in these two groups. The former group maintains traces of the observed resonances even at low intensities, while the relative signal intensity gains, when compared to the next highest intensity measurement, are lowest for high intensity measurements. The latter maintains traces of resonant signal only at 10% intensity, with marked increases in relative signal intensity for higher pulse energies. Due to the short pulse duration, the pulse energy features as a prominent factor in the irradiance and the non-linear processes. This observation represents evidence for the creation of these high charge state iron cations being a direct or indirect product of non-linear processes in iron pentacarbonyl.

FIG. 24 shows the integrated iron cation signals for charge states 1 through 14, extracted from the ferrocene measurements shown in FIG. 19 , FIG. 20, FIG. 21 and FIG. 22. Similar to what was observed in FIG. 23, the strong disagreement between the theoretically predicted resonances for the XAS of an isolated iron atom and the experimentally measured ion yields of ferrocene into the Fe^+ channel for all intensities is apparent, yet unsurprising. Similarly, the measurement also disagrees with the findings of Godehusen et al. [32] regarding the measurement of the $Fe(C_5H_5)_2 \longrightarrow Fe^+$ channel. In their work, Godehusen et al. measure a strong L-edge resonance in this fragmentation channel for photon energies of 709 eV and 712 eV, which they call the 'low-energy' peaks and which are absent in our measurement. Some agreement is preserved between this work and the measurements of Godehusen et al. for the two resonances starting at 720 eV. By also contrasting this observation with the results of Schippers et al. [80] work on L-edge XAS of singly charged iron cations, a similar impact of charge transfer to the ligands, as was observed for iron pentacarbonyl, can be deduced along a similar line of argument.

What is more surprising than this disagreement in measurements, is the shift in relative signal intensity with dominant on-resonance signal for 10% and 25% GATT transmitted energy. The relative strong production of Fe^+ for the lower pulse energy measurements seems to indicate that the fragmentation channel $Fe(C_5H_5)_2 \longrightarrow Fe^+$ is more accessible for low pulse energies than for high ones. A similar observation can be made for the channel $Fe(C_5H_5)_2 \longrightarrow Fe_2^+$, in which the relative signal intensity for low pulse energies is similarly strong. This result hints at a notable difference in fragmentation pathways between iron pentacarbonyl and ferrocene.

Returning to the considerations on the resonances for the cation charge states Fe^{n+}, with $n =$
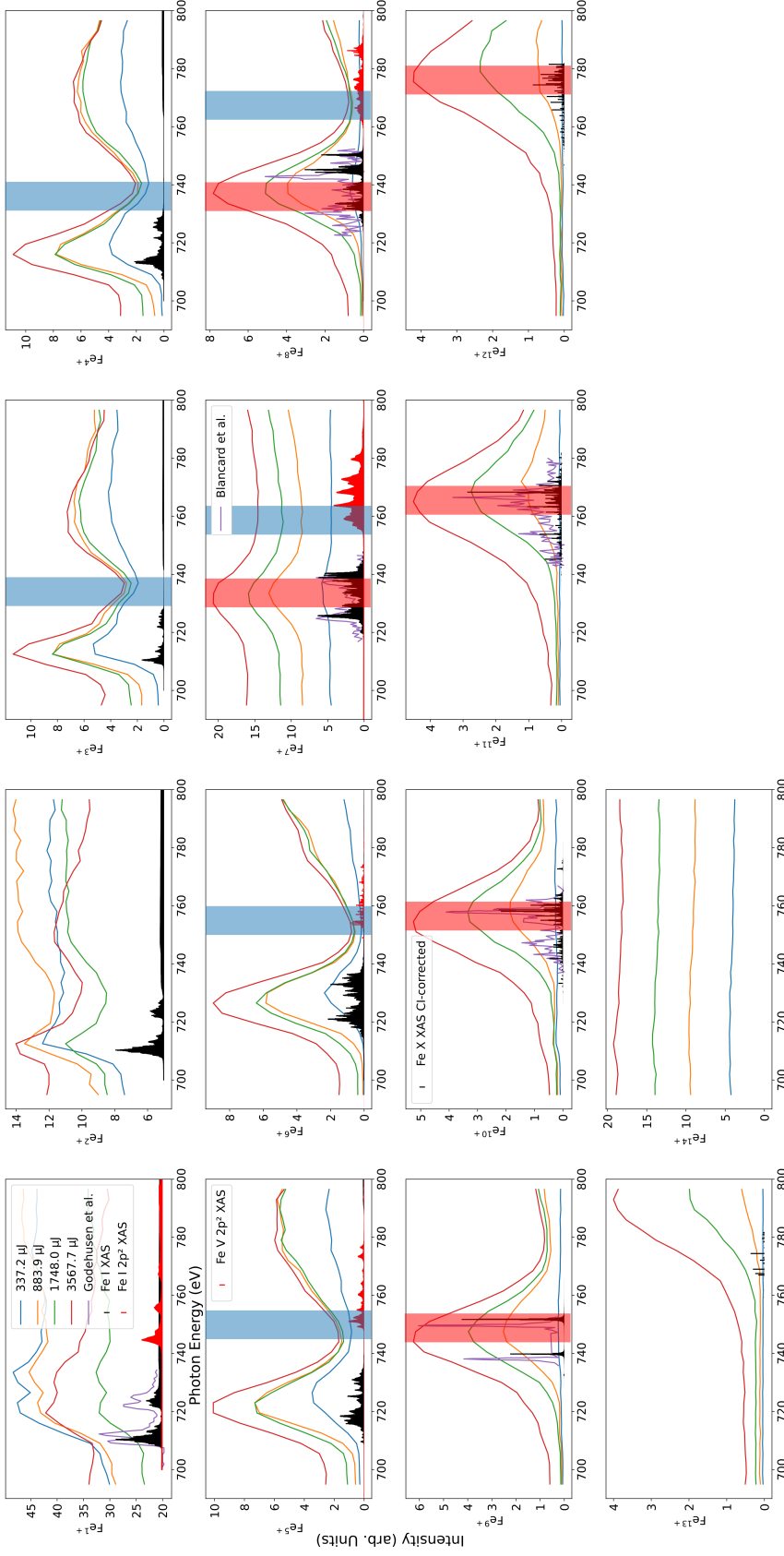
Figure 24: The collection of iron cation signals taken of the sample Fe(C$_5$H$_5$)$_2$ for the photon energy range 695 eV to 800 eV, as recorded by the iToF spectrometer detailed in Section 4.1.3 for the delivered intensity percentages of 10%, 25%, 50%, and 100%. The integrated signal is compared to the results for isolated iron cations outlined in Section 3 and to the experimental single photoionization results of Godehusen et al. and Blancard et al., respectively [10, 32].Regions of 10 eV, associated with uncharacteristically large signal depletion for high pulse intensities at photon energies not connected to known SCH-resonances of the respective charge state have been marked in blue. Contrast with the resonance maxima marked in red reveals evidence for an effective pumping mechanism into resonances of charge states of 4 additional charges for Fe^{n+} ($n = 2 - 5$). For Fe^{n+} ($n = 6 - 7$), the overlap of signal depletion and resonance suggests the accumulation of 3 additional charges instead.

2 : 9, very good agreement is found between the resonance energy results of the isolated iron atom model and the measured resonances for the product fragmentation channels associated with each cation in ferrocene. The distinct disagreement lies in the rising ionization edge in each channel, which is not well mapped in the model considerations. These observations mirror the previously discussed results obtained for iron pentacarbonyl.

A further similarity between the measurement series on both samples is found in the recurring trend of shifting resonances in the ferrocene iron cation data, particularly in the context of high intensity and high charge states found in the measurement results. FIG. 24 shows that as charge increases on a cationic species, shifts in resonance maxima at very intense pulse energies are observed. These tend toward lower photon energies as compared to the resonance maxima for the same pulse energy measurement results in their less charged counterparts. This trend is nearly absent for Fe^+, but several electronvolts large for charge states Fe^{12+} or above. While these measurements do fall within the bandwidth of the European XFEL, the behavior is constrained and effectively very similar to the results that were measured for the iron pentacarbonyl. The possibility of these shifts representing a hint at non-linear production pathways during the photon-matter interaction influencing the measured photon energy resonances should therefore be taken into consideration.

In terms of resonance maximum intensity, we also obtain findings similar to the iron pentacarbonyl measurement. In particular, the results obtained for the high charge iron cation resonances in the low pulse energy cation group maintains traces of the observed resonances even at low intensities. This also affects some low charge state cations. In the case of Fe^+, it even becomes the dominant signal at low pulse energy measurements. The relative signal gains when comparing to the next highest pulse energy measurement are lowest for measurements with high pulse energy for this species of cations. The group of high charge state cations, starting at Fe^{9+}, maintain traces of identifiable resonances only at 10% intensity, with observed increases in relative signal intensity for higher pulse energies. If one ascribes the specific onset of this process to the irradiance of the sample at high pulse energies for Fe^{9+} and to the chemical environment of the molecule, the remaining observation matches the findings for multiply charged iron cations in iron pentacarbonyl.

FIG. 24 shows the same 'bleaching' effect in most cationic resonances at the same relative position, similar to what was observed for iron pentacarbonyl: In the right flank of the resonance signal, relative intensity decreases drastically. Again, this effect is strongest for the cations Fe^{n+}, with $n = 3 : 6, 8$. The relative decrease in intensity is also spread unevenly across the different measured intensities. For the measurements associated with 10% GATT transmitted pulse energies, no such effect can be observed, while for the three other pulse energy categories the effect is not only present, but also increases continuously in strength from low-, to high-intensity pulse energies. This mirrors the findings for iron pentacarbonyl and lends itself as evidence for an intensity dependent effect occuring in these cation production channels at higher photon energies than the SCH resonance and ioniztion region. Non-linearly pulse-energy-dependent processes such as DCH creation represent such effects.

The similarities in the data underscore the observations that were made, both for the measurements on iron pentacarbonyl as well as those for ferrocene. Despite some apparent differences between the measurement results on both samples, that may be ascribed to the molecular makeup and geometry of each sample, they fragment remarkably similar when irradiated with

high pulse energy X-Ray pulses.

6.2 Impact of DCH Processes on the XAS Ion Spectra

The conducted measurements on iron pentacarbonyl and ferrocene reveal some striking similarities in the fragmentation of complex $3d$ metals under extreme irradiative conditions. Yet, for fragmentation channels into Fe^+ and Fe^{2+}, strong differences in relative resonance intensity were observed, as shown in FIG. 23 and FIG. 24 . Several resonance peaks, shown in the work of Godehusen et al., were not resolved [32] and low pulse energy measurements appear to favor the fragmentation products Fe^+ and Fe^{2+} in ferrocene, but not in iron pentacarbonyl.

While good agreement was found for the overall resonance positions between the isolated iron atom model and the measurement results of the iron pentacarbonyl and ferrocene measurements, it was observed that the width of the measured resonances is unexpectedly large. Taking the fragmentation into the Fe^{9+} product cation channel as an example, this becomes very apparent. Comparing FIG. 23 and FIG. 24 for Fe^{9+}, the observed resonance is much larger than what would be expected for the 7.4 eV bandwidth and the two expected sharp lines stemming from the isolated iron atom model. Similar observations can be made for the other multiply charged iron cations, starting at the Fe^{4+} cation.

There are three indicators, then, for DCH processes playing a role in the irradiation of iron pentacarbonyl and ferrocene with short, intense X-Ray pulses. The width of the respective resonances for multiply charged cations, their shift in resonance maxima and the observed "bleaching" effect occuring in regions not associated with SCH processes.

A possible explanation for the observed depletion of ion yield at high intensities is provided by the work of Nagler at al. [70]. In their work on saturable absorption in aluminum during soft X-Ray irradiation, Nagler et al. [70], describe a similar effect occurring in L-edge absorption for aluminum at intense pulse energies. Their work details the observed 'bleaching' as a lack of accessible low-level electrons in their aluminum sample. For short X-Ray pulses, the L-shell electrons getting ionized by the first part of the pulse are not replenished, as the lifetime of the Auger-Meitner decay is estimated as 40 fs by the work of Almbladh et al. [3]. This turns the sample transparent for the remaining X-Ray pulse. A depletion of L-shell electrons seems to be the source of this effect in iron as well. The lack of electrons representing of course another reason to suspect the involvement of non-linear processes in this scenario, despite the considerably shorter estimated lifetime of the Auger-Meitner decay.

There is even more evidence to suspect the exact nature of the non-linear processes as double core-hole excitations, when comparing the positions of the right flank of the resonances in question to the resonance maxima of iron cations of higher charge. Here, we observe that these positions for both ferrocene and iron pentacarbonyl in FIG. 23 and FIG. 24 occur at the region of resonance maxima for charge states not two, but four charges higher than the iron cation in question. Examples of this can be found in the Fe^{3+}, Fe^{4+}, Fe^{5+} and Fe^{6+} cation signals. This trend continues more or less accurately throughout the cationic series of L-edge resonances. It can be found in FIG. 24 and FIG. 23 by observing the photon energies of the 10 eV region marked in blue and that in red. The agreement for the first cation series not only connects two observations, but also reinforces DCH processes as the underlying processes behind them, as an explanation for this observation is the appearance of DCH processes at

these photon energies, pumping into higher charge states with great efficiency. As the non-linear processes deplete the L-shell of electrons with an additional Auger-Meitner process during the short pulse duration, the product cations become positively charged to a larger degree.

While agreement between depletion region and shifting resonance maximum at a charge gain of 4+ is very good for ion yields of Fe^{3+} through Fe^{5+}, slight differences in photon energy occur at Fe^{6+} that become much more apparent and extend to several eV for Fe^{7+} and above. This divergence from the postulated charge gain of 4+ requires an explanation, which can be provided when investigating the most likely relaxation processes in these cations.

FIG. 25 shows one sequence of excitation and relaxation processes that occur following a photon-matter interaction between a multiply charged iron cation and an intense X-Ray pulse. While resonant excitation has been previously discussed in Section 2, it is of note that in the photon energy range in question, a resonant-resonant DCH excitation is a viable pathway when compared to the relatively high photon energy required to ionize a multiply charged iron cation. First to occur are the two resonant excitations, the first depicted in a.) into the $4d$, $5d$ or nd orbital and the second, depicted in b.) into the $3d$ orbital. As previously discussed, these processes occur within the lifetime of the Auger-Meitner process. This first Auger-Meitner relaxation is shown in c.).

Following this, and within the lifetime of the second Auger-Meitner relaxation, there occur two super-Coster-Kronig transitions that fill the two holes in the $3p$ level. These relaxation processes, particularly the importance of the $M_{23}M_{45}M_{45}$ super-Coster-Kronig decay channel for metals such as Fe, have been previously discussed in the work of Nyholm et al. [71] on Auger-Meitner and Coster-Kronig broadening effects in the $2p$ and $3p$ photoelectron spectra from the metals Ti to Zn. It is this efficient and fast decay channel that ultimately enables more charge accumulation for Fe in the relaxation processes than for other samples.

Following the two super-Coster-Kronig decays, the final $2p$ hole decays via Auger-Meitner relaxation, as depicted in f.). The total charge accumulated in these processes corresponds to 4+. It is important to acknowledge that the product pathway depicted here is only one of a variety of decay channels that all compete with each other. Nevertheless, there are strong arguments for the efficiency of this particular product channel. The above-threshold photon energy marked in red in FIG. 23 and FIG. 24 lend themselves well to a resonant $3d$ DCH excitation, as the good agreement with the theoretical cross-sections calculated for fragment channels Fe^{5+} to Fe^{8+} shows. The efficiency of the super-Coster-Kronig relaxation process has been previously established, with shortness and efficiency in Zn *III* sufficing for the work of Walker et al. to report the observation of laser gain in the vacuum ultraviolet pumped by super-Coster–Kronig decay [95]. The absence of radiative decay channels also falls in line with the findings of Beerwerth et al. and McGuire et al. on their insignificance in neutral to triply charged Fe atoms [9, 63].

FIG. 26 shows a similar relaxation process cascade for an iron atom of even higher charge, in this instance Fe^{6+}. The notable difference to FIG. 25 is the further depleted $3d$ orbital in the initial target. This leads to an almost complete depopulation there over the course of the primary Auger-Meitner decay, which in turn prevents a second ultrafast super-Coster-Kronig decay from occurring. The result is a charge gain of 3+ for this cation and the ones with depleted $3d$ orbitals.

Lending more weight to the considerations of DCH processes in multiply charged iron cations, FIG. 27 shows the single-photon ionization cross-section for m-fold photoionization of Fe^{3+}, published by Beerwerth et al. [9]. These results on near L-edge single and multiple photoionization of triply charged iron cations not only match the observed single-photon ionization yield shown in FIG. 23 and FIG. 24, they also show that single-photon single- and double-ionization have comparable cross-sections at the L-edge, while triple- or quadruple-ionization have much weaker cross-sections. Furthermore, the onset of a strong resonance is found to partially overlap with the region of observed depletion for high pulse-energy measurements, making a resonant-resonant DCH process in this region a likely explanation due to the match in photon energy region between single-photon resonance and resonant double core-hole excitation.

These considerations on DCH processes in multiply charged iron cations explain the observations made on FIG. 23 and FIG. 24. Such an explanation roots in the assertion that model considerations of SCH processes only are ill-equipped to incorporate DCH processes for the shift in resonance position and width. In these measurements, however, the multiply charged iron cations seem to result from both SCH, as well as DCH processes. Yet any experimental mixture of origin states, such as SCH and DCH sources, that is not overwhelmingly leaning toward the former, will slightly skew the resulting picture and disagree with a purely SCH isolated iron cation model.
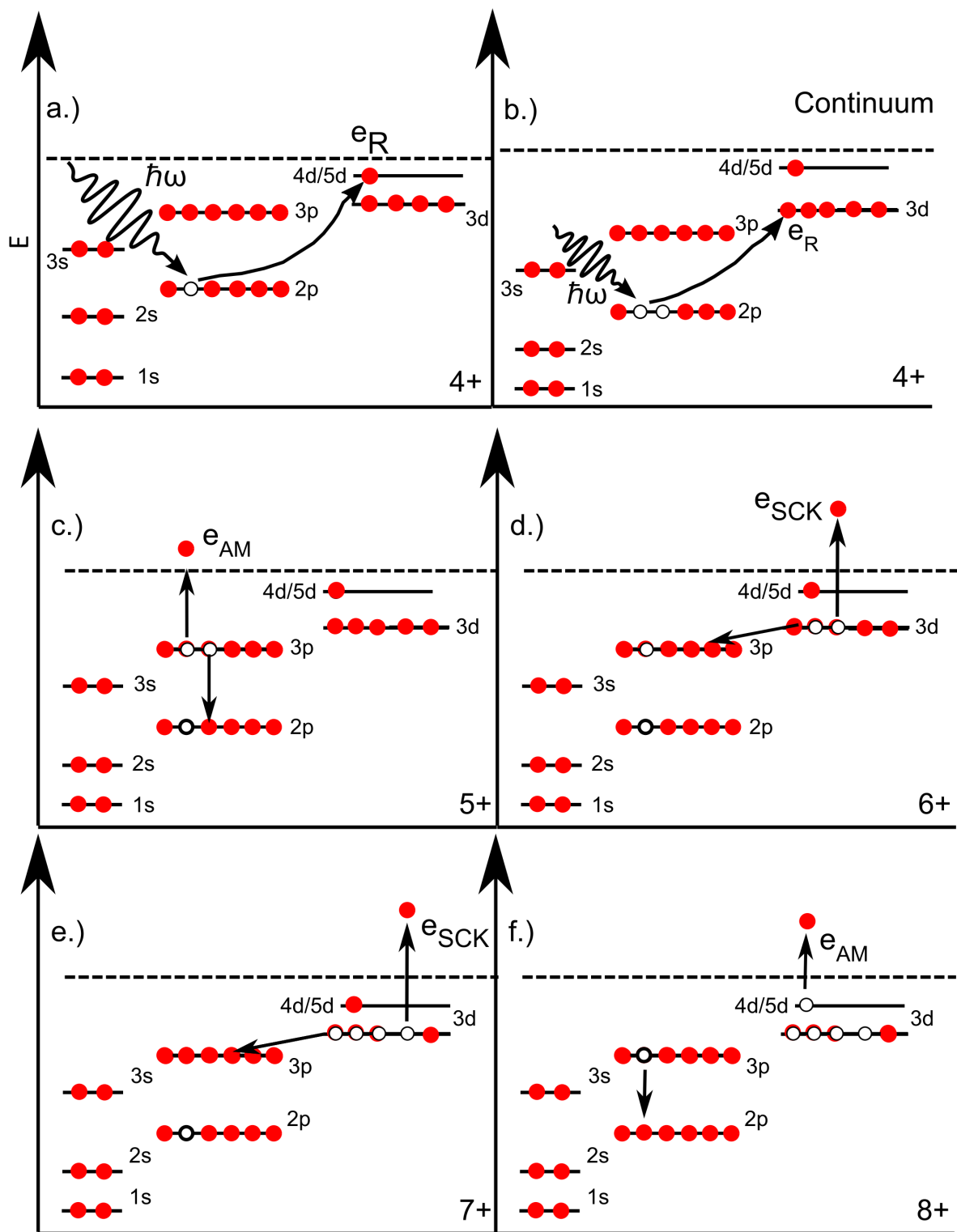
Figure 25: One step-by-step illustration of a likely cascade following irradiation of Fe^{4+} showing a resonant $2p^2$ excitation in a.) and b.), which leads to a primary Auger-Meitner relaxation in c.), followed by two ultrafast super-Coster-Kronig transistions in d.) and e.) and a final Auger-Meitner transition in f.). The total accumulated charge gain of such a process is 4+, leading to the production of Fe^{8+}.
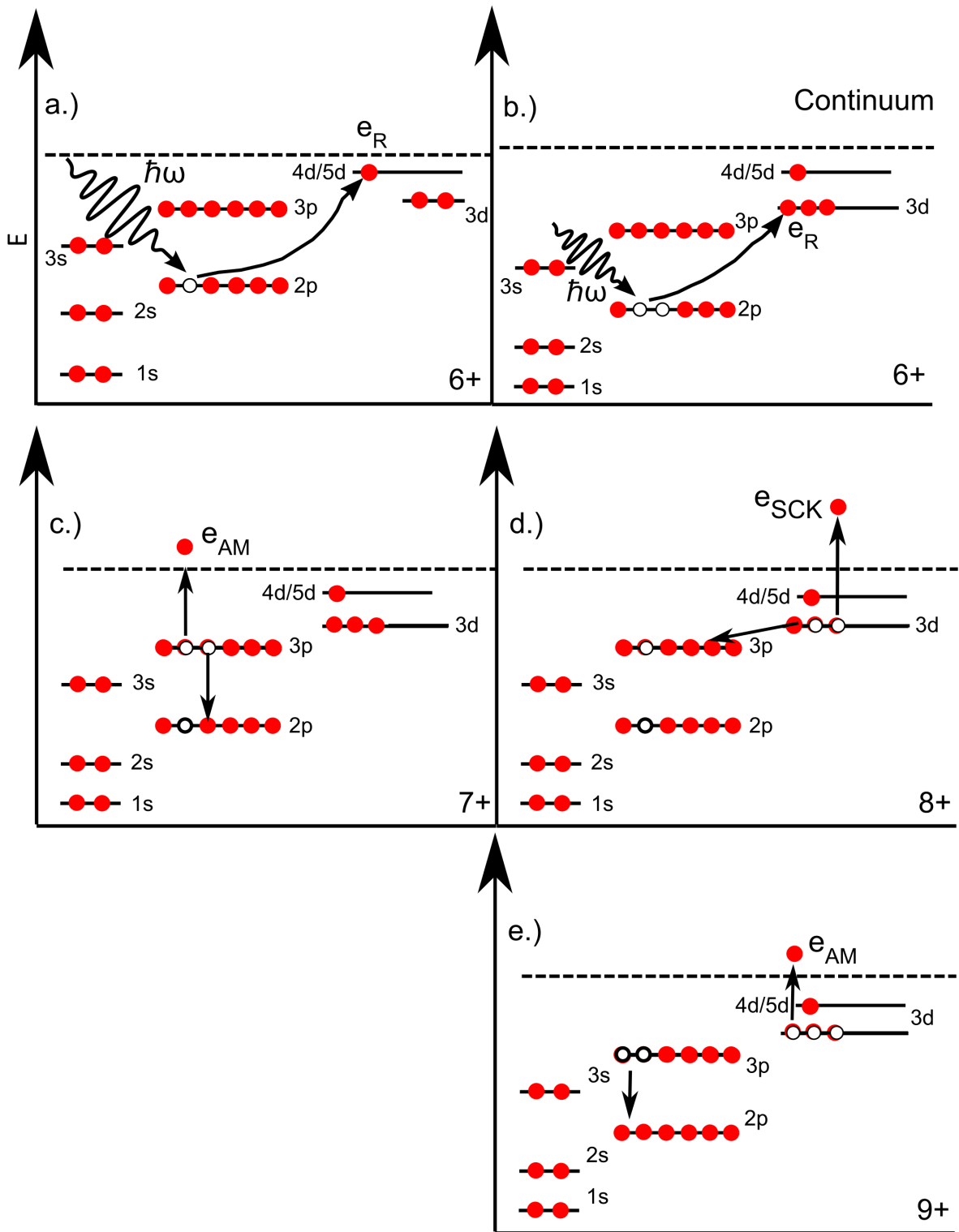
Figure 26: One step-by-step illustration of a likely cascade following irradiation of Fe^{6+} showing a DCH resonant $2p^2$ excitation in a.) and b.), which leads to a primary Auger-Meitner relaxation in c.), followed by a single ultrafast super-Coster-Kronig transistions in d.) and a final Auger-Meitner transition in e.). The total accumulated charge gain of such a process is 3+, leading to the production of Fe^{9+}.
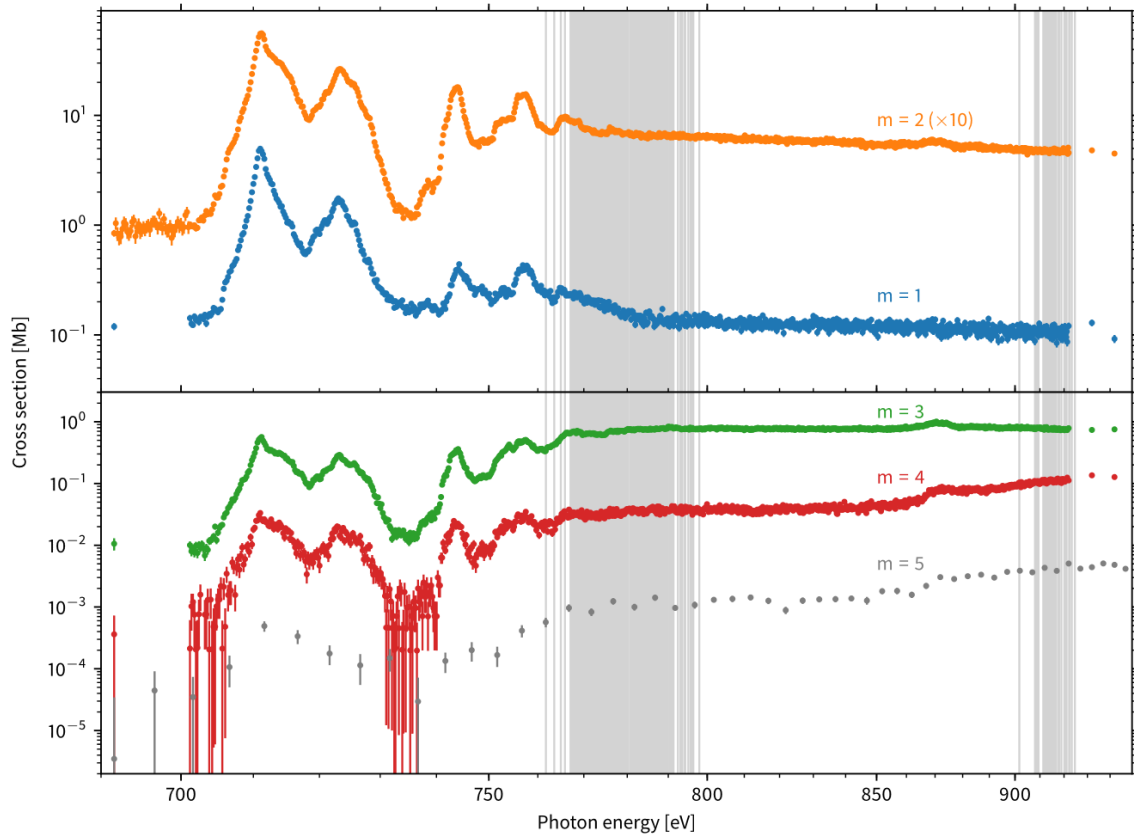
Figure 27: Measured partial cross sections by Beerwerth et al. [9], σ_m, for m-fold photoionization of Fe^{3+}. The data is plotted in units of megabarns (Mb), which is $1 \times 10^{-18}\,cm^2$. The partial cross section for $m = 2$ was multiplied by a factor 10 to avoid the large overlap with the $m = 1$ curve. The vertical gray lines show the computed energy level structure of the $2s^2 2p^5 3s^2 3p^6 3d^5$ and $2s 2p^6 3s^2 3p^6 3d^5$ configurations respectively, approximately between 760 and 800 eV and between 900 and 925 eV. The lowest energy levels correspond to the ionization threshold for $2p$ and $2s$ electrons, respectively. For a better view of the low-energy resonance structures, the energy scale has been compressed toward high photon energies according to the formula $E' = log(E - 600eV)$. Figure reproduced from *Near L-edge Single and Multiple Photoionization of Triply Charged Iron Ions*, 2019, The Astrophysical Journal, volume 887, page 189 with permission of the authors. ©AAS. Reproduced with permission.

6.3 Double Core-Hole Ion Spectroscopy in Iron Pentacarbonyl

FIG. 23 and FIG. 24 suggest the involvement of nonlinear processes in the creation of the multiply charged cations in ferrocene and iron pentacarbonyl. To evaluate the cationic side of the photon-matter interaction, each identified charge state must be tested for non-linear behavior in relation to pulse energy for the accessed photon energy range. In their studies on such processes in Xenon, Röhrig et al. present highly charged Xenon cations for a specific photon energy as a function of the peak fluence of the associated X-Ray pulse [76]. Following a similar approach, the signal associated with each iron cation charge state is integrated over its resonance for each pulse energy measurement. The resulting ion yields are then displayed by pulse energy in order to visualize the differences in yield rise by cationic state. Furthermore, the specific photon energy of 743 eV is chosen as an exemplary photon energy for the resonant DCH excitation regime and iron charge state intensities are similarly displayed in this isolated photon energy case.
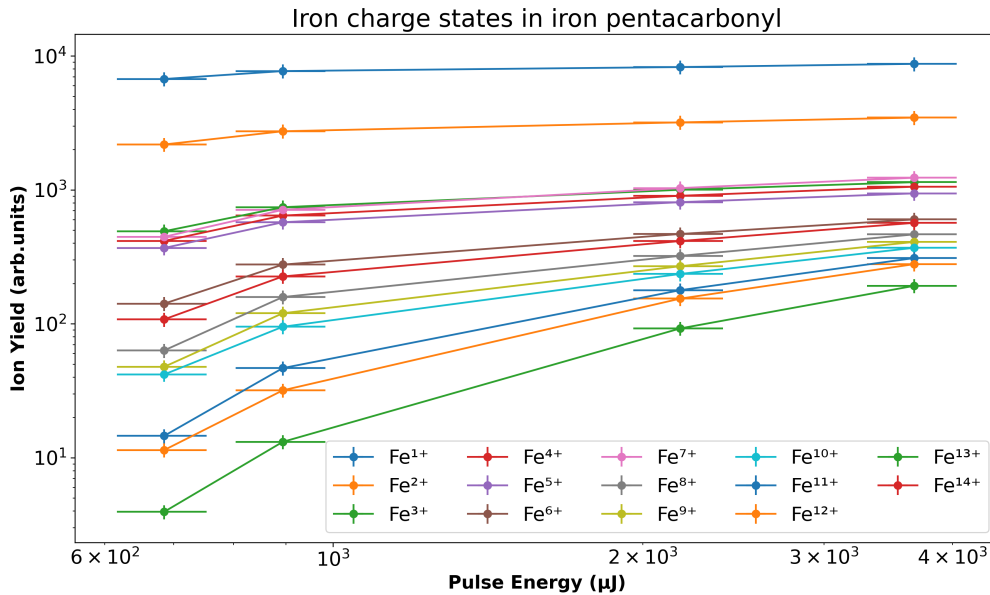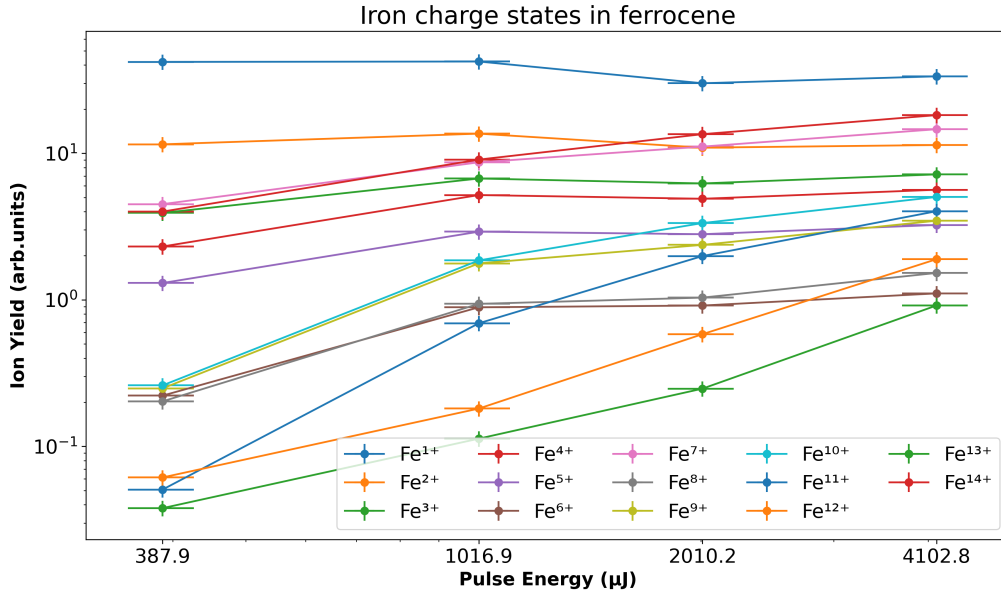

Figure 28: The iron ion charge states of iron pentacarbonyl detected for the various pulse energies and photon energies. The gain rates of multiply charged iron cations appear to conform more to non-linear behavior than those of less charged iron cations.

FIG. 28 displays the iron cation charge states and the rise of their signal intensity with rising pulse energy. The most notable observation regarding this figure is the increasingly non-linear relation between pulse energy and signal intensity, encapsulated by the gradient of the charge state intensities. The detection of Fe^{n+} with $n = 1 : 7$ shows only small increases with pulse energy that do not foster the thought of non-linear processes having a part in their creation. For Fe^{n+} with $n = 8 : 14$ this is not the case. The gain in signal with rising pulse energy is increasingly steep for each higher charge state from $n = 8$ to $n = 13$, with $n = 14$ rising more akin to the lower end of this charge state group. This suggests that the higher charge states
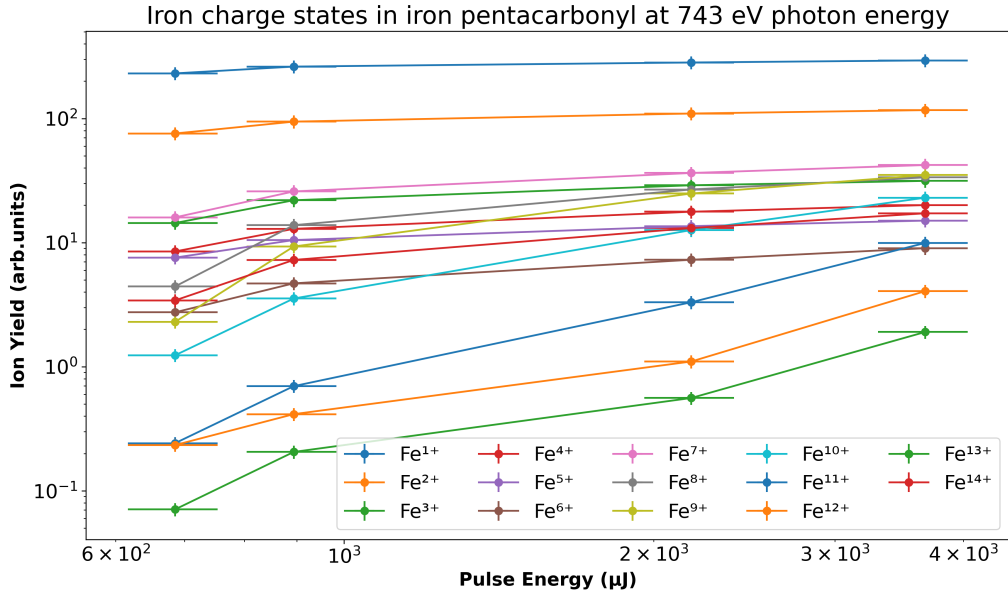
Figure 29: The iron ion charge states of iron pentacarbonyl detected for the various pulse energies at 743 eV. The gain rates of multiply charged iron cations appear to conform more to non-linear behavior than those of less charged iron cations.

detected during the experiment are indeed results of relaxation processes following non-linear excitations. These results align with the work of Rudek et al. on ultra-efficient ionization of Xenon atoms by a similar experimental scheme [75].

FIG. 29 specifies a distinct photon energy for which DCH resonance cross-section is reasonably expected to out-scale SCH cross-section in both samples. The difference to FIG. 28 is the distinctly stronger rise in signal intensity of Fe^{n+} with $n = 8, 9, 10$ that is notably larger than comparable species and thereby supports the hypothesis of non-linear processes playing a distinguishable role in their creation. The choice in photon energy also falls directly into the respective resonances for the charge states under consideration.

In the context of the work of Rudek et al. and Röhrig et al., the present results in FIG. 28 and FIG. 29 fall on the upper end of the signal intensity vs. fluence graph [75, 76]. Assuming a 3 μm by 3 μm spot for this experiment, the same spotsize that was assumed for Rudek et al., fluence in the present work ranges from 80 $\frac{\mu J}{\mu m^2}$ to 410 $\frac{\mu J}{\mu m^2}$, placing the present results at the far end of the fluence range. This could entail that the saturation effect that was observed in Xenon cations in the works of Rudek et al. plays a role for the high-fluence measurements in this work, particularly for less charged iron cations.

6.4 Double Core-Hole Ion Spectroscopy in Ferrocene

FIG. 30 shows the ferrocene iron cation charge states and the rise of their yield with rising pulse energy. The behavior of ion yield gain by cation charge state differs somewhat from
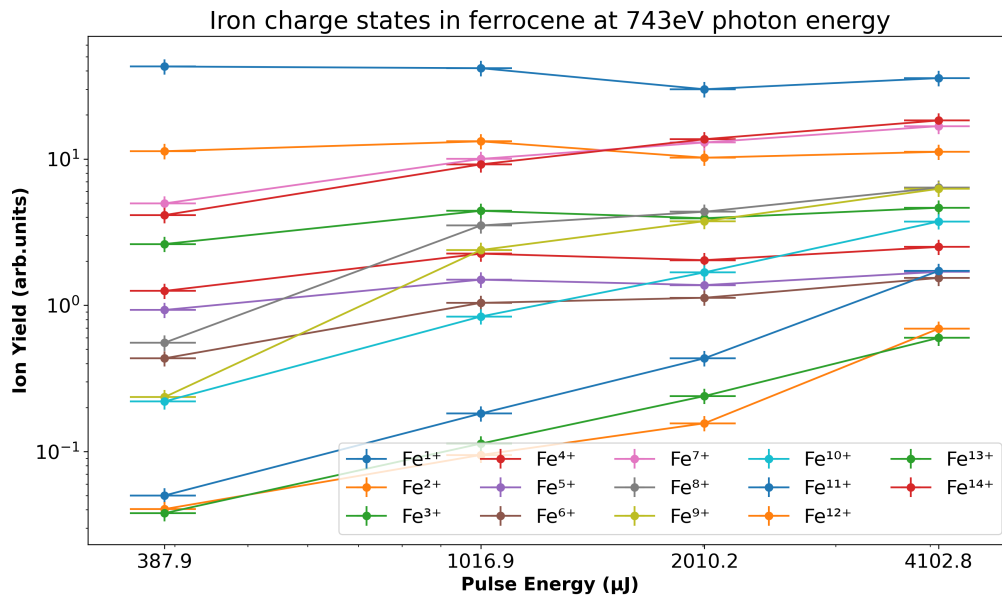
Figure 30: The iron ion charge states of ferrocene detected for the various pulse energies and photon energies. The gain of multiply charged iron cations appear to conform more to non-linear behavior than those of less charged iron cations.

FIG. 29. The most notable difference regarding this figure is the onset of the increasingly non-linear relation between pulse energy and signal intensity. The detection of Fe^{n+}, with $n = 1 : 5$, shows only small increases with pulse energy that do not foster the thought of non-linear processes having a part in their creation, which resembles the results for $Fe(CO)_5$. For Fe^{n+} with $n = 6 : 14$ this is not the case, which puts the onset of increased ion yield gain at a much lower cationic charge state than $Fe(CO)_5$. Similar to the cationic gain behavior in iron pentacarbonyl, the gain in signal with rising pulse energy is increasingly steep for each higher charge state from $n = 6$ to $n = 13$. This suggests that the higher charge states detected during the experiment for this sample are indeed results of relaxation processes following non-linear excitations. These results again align with the work of Rudek et al. [75].

FIG. 31 specifies a distinct photon energy for which DCH resonance cross-section is reasonably expected to out-scale SCH cross-section in both samples. The difference to FIG. 30 is the distinctly stronger rise in signal intensity of Fe^{n+} with $n = 8, 9, 10$ that is notably larger than comparable species and thereby supports the hypothesis of non-linear processes playing a distinguishable role in their creation. This matches the results for iron pentacarbonyl very well. The choice in photon energy also falls directly into the respective resonances for the charge states under consideration. In this sample, it can be seen that the rise in ion yield behaves similarly for Fe^{n+} with $n = 8, 9, 10$ as it does for Fe^{n+} with $n = 11, 12, 13$.

In the context of the work of Rudek et al. and Röhrig et al., the present results in FIG. 30 and FIG. 31 also fall on the upper end of the signal intensity vs. fluence graph [75, 76]. Assuming again a $3\,\mu m$ by $3\,\mu m$ spot for these measurements, the same spotsize that was assumed for

71

Figure 31: The iron ion charge states of ferrocene detected for the various pulse energies at 743 eV. The gain of multiply charged iron cations appear to conform more to non-linear behavior than those of less charged iron cations.

Rudek et al., fluence in the present work ranges from $40 \frac{\mu J}{\mu m^2}$ to $460 \frac{\mu J}{\mu m^2}$, placing the present results at the far end of the fluence range. This could entail that the saturation effect that was observed in Xenon cations in the works of Rudek et al. plays a role for the high-fluence measurements in this work, particularly for less charged iron cations.

7 Electron Spectra of Iron Pentacarbonyl and Ferrocene

The data pertaining to the product cations revealed regions of photon energies in which DCH processes occur in the iron *L*-edge spectroscopy of iron pentacarbonyl and ferrocene and their product iron cations at high pulse energies. In this chapter, a detailed analysis is conducted on the electron spectra obtained with the goal of resolving the Auger-Meitner electron traces of the DCH processes in iron pentacarbonyl and ferrocene.

As described in Section 4.1.3, the eToFs shown in FIG. 9b, were used in this experiment to obtain electron spectra of the two samples $Fe(CO)_5$ and $Fe(C_5H_5)_2$. Spectra were taken over the photon energy range of 680 eV to 800 eV in 3.5 eV steps with the bandwidth given as 1% of the photon energy, resulting in an estimated bandwidth of 6.80 eV to 8.00 eV over the course of the measured spectra. These measurements were repeated for ferrocene at GATT percentages of 1%, 10%, 30%, 80% and 100% corresponding to a GATT transmitted X-Ray pulse energy of 60 µJ, 600 µJ, 1800 µJ, 4800 µJ and 6000 µJ respectively, as measured by the tunnel GMD. Pulse energies measured by the GMD in the SQS instrument yielded fractions of this GATT transmitted pulse energy, with pulse energies measured between approximately 46 µJ and 3670 µJ. For iron pentacarbonyl, measurements were conducted at GATT percentages of 1%, 10%, 80%, and 100% corresponding to a GATT transmitted X-Ray pulse energy of 60 µJ, 600 µJ, 4800 µJ and 6000 µJ respectively, as measured by the tunnel GMD. Pulse energies measured by the GMD in the SQS instrument yielded fractions of this GATT transmitted pulse energy, with pulse energies measured between approximately 44 µJ and 3830 µJ. Line assignments and inspection of measurements at varying pulse energies help to disentangle the various SCH and DCH sources in the spectrum.

Analysis in this chapter focuses on the results obtained by the eToF spectrometer 1 with $V_{Drift} = -480$ V as outlined in TABLE 4. This reflects the presence of multiple regions of interest on the kinetic energy scale of the detected electrons, which were predicted in Section 3, in which the expected DCH electron signal outscales the SCH electron signal contribution in both samples.

7.1 Electron Spectra of Iron Pentacarbonyl

FIG. 32 shows the results of the eToF spectroscopy measurements conducted on iron pentacarbonyl in the kinetic energy window ranging from 480 eV to 800 eV. This kinetic energy window enables identification of kinetic energy regions of the iron L-edge Auger-Meitner electrons as the most prominently displayed signal. They can be found at markers *c*.), *d*.) and *e*.). In addition to the groups of traces of identifiable Auger-Meitner electrons with kinetic energies ranging from 560 eV to 720 eV in the signal sum representation at the left edge of the figure, two traces of photoelectron lines can be identified and are marked with black lines. These photo-excited valence electrons are recognizable as such due to their kinetic energy increasing linearly with the photon energy. The line assignments shown in TABLE 9 show an additional set of Auger-Meitner electron lines that can be attributed to the CO ligands of the sample and are marked as *a*.).

These aforementioned CO Auger-Meitner electron lines are present at every photon energy and show no specific resonant behavior, as the photon energies covered in this scan do not
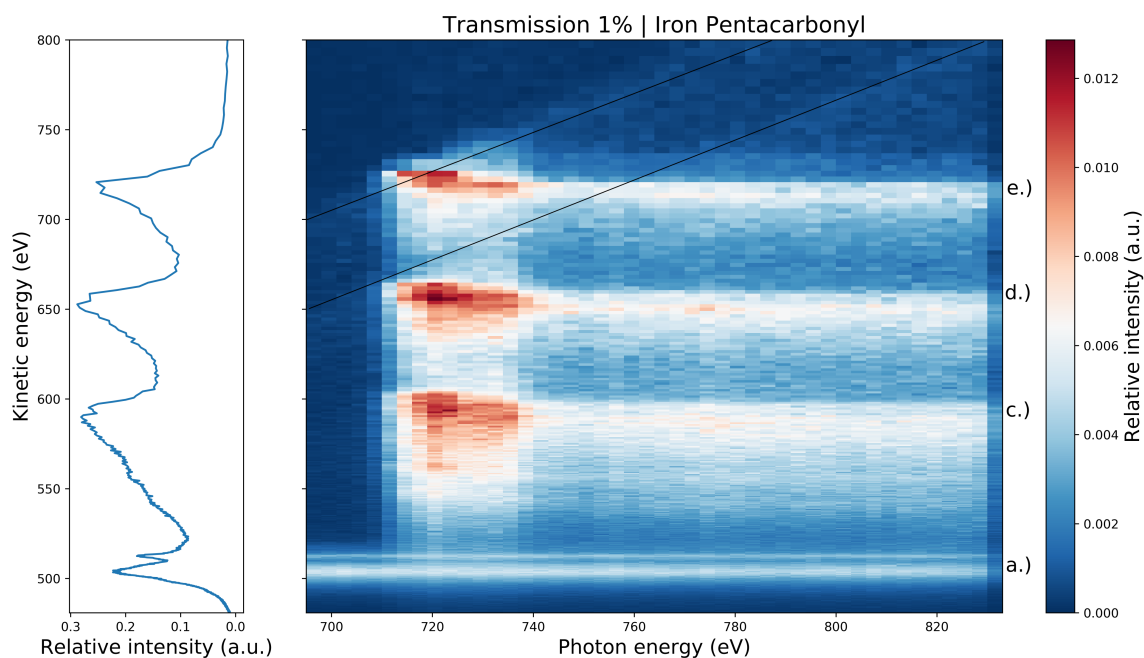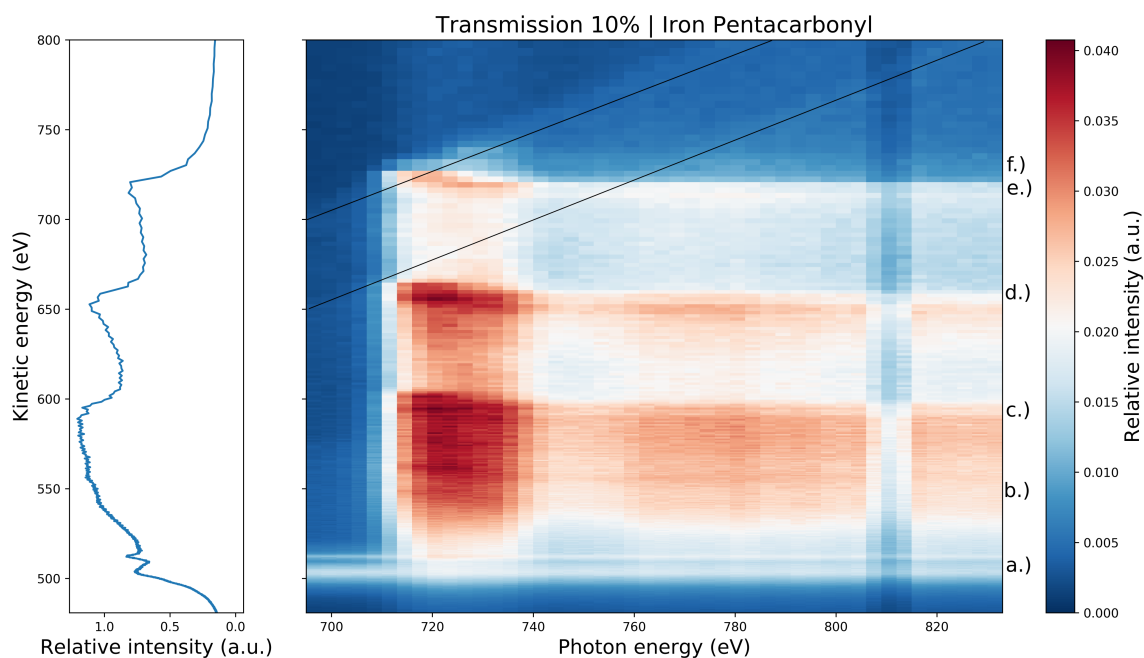
Figure 32: The collection of electron spectra taken of the sample $Fe(CO)_5$ for the photon energy range 695 eV to 830 eV, as recorded by the eToF spectrometer 1 with retardation voltages detailed in TABLE 4. Total signal with respect to the kinetic energy of the detected electrons is shown to the left. GATT transmitted intensity was 1 % of maximum requested energy with pulse energies measured by SQS GMD ranging from approximately 65 µJ to 74 µJ. Two photoelectron lines are marked in black. Four Auger-Meitner electron regions are marked with letters $a.)$, $c.)$, $d.)$ and $e.)$.

cover C or O resonances. Both lines could be resolved and their relative width matches the results obtained by Ungier et al. [94], who used electron–electron coincidence spectroscopy to separate KVV Auger spectra in CO into several component spectra, each arising from different core-excited initial states. A comparison to the studies of Koel et al. [41] on chemabsorbed CO on Ni furthermore enables to differentiate between CO and O lines for this feature in terms of feature form and kinetic energies. The electron signals associated with the Fe constituent, however, show strong resonant responses at photon energy ranges from 713 eV to 737 eV. This range is the same for all Auger-Meitner lines found at markers $c.)$, $d.)$ and $e.)$. The resonant behavior displayed here is quite strong and overlaps with the signal of both Fe photon lines at high kinetic energies. The Auger-Meitner electron signal at 560 eV could barely be resolved in the total signal, yet is recognizable in the color map. In a stark contrast to the low feature resolution, the signal of the $L_{23}M_{23}M_{23}$ Auger-Meitner electron feature at 590 eV could be resolved very well and the two peak structure matches well the work of Allen et al. [2]. The same is true for the $L_{23}M_{23}M_{45}$ signal at 650 eV, where the peak form presented by Allen et al. [2] is recreated in this work almost identically.

The apparent increased width in the peaks of the iron Auger-Meitner lines is responsible for one feature being clearly visible, while the other is surrounded by a large amount of signal.

It is explained by the observation that this broadening of the peaks is tending towards low kinetic energies only, similar to the trend that was modelled for the Auger-Meitner electrons of high charge states for the isolated iron atom cations. The observed effect is most apparent when comparing the relative width of the Fe associated Auger-Meitner lines with those associated with CO. This large signal width towards low kinetic energies is responsible for the broad region and small relative signal at 560 eV. The effect can be explained by referencing FIG. 15: At 600 mJ pulse energy, a significant presence of multiply charged iron cations is detected in the interaction region. It stands to reason, that when interacting with short 60 mJ X-Ray pulses, iron pentacarbonyl as well as multiply charged iron cations emit Auger-Meitner electrons, which would lead to the observed smearing out of the iron electron signal at low kinetic energies. Where electron signal of only iron pentacarbonyl is desired, the additional electron signal of multiply charged iron cations presents a hindrance. The trend towards lower kinetic energies of detected Auger-Meitner electrons, as charge increases on the iron cation, was demonstrated in FIG. 6. As a result of these observations, the spectrum can be thought of as hosting a collection of Auger-Meitner spectra of iron cation species, each shifting to slightly lower kinetic energies as charge increases.

Table 9: The Auger-Meitner- and photoelectron assignment of the traces identified in FIG. 32. The associated kinetic energies are in good agreement with previous works by Ungier et al. [94] and Allen et al. [2] . The literature used for the assignment of the particular trace are shown as a reference.

Kinetic Energy (eV)	Electronic Transition	Reference Energy (eV)	Literature
503	CO KVV Auger-Meitner	505	Ungier et al. [94]
513	CO KVV Auger-Meitner	510	Ungier et al. [94]
537.5	CO K^2VV		
558.5	CO K^2VV		
560	Fe $L_{23}M_{23}M_{23}$	560	Allen et al. [2]
590	Fe $L_{23}M_{23}M_{23}$	590	Allen et al. [2]
650	Fe $L_{23}M_{23}M_{45}$	650	Allen et al. [2]
720	Fe $L_{23}M_{45}M_{45}$	710	Allen et al. [2]
747.5	Fe $L_{23}^2M_{45}M_{45}$		
650	Fe M_{23}	648	
700	Fe(CO)$_5$ V	699	

FIG. 33 shows the product electrons of the same sample, after irradiation with X-Ray pulses of pulse energy ranging from 480 μJ to 550 μJ. The line assignments presented in TABLE 9 can be easily found at the same kinetic energies, as in FIG. 32. Overall, the signal appears similar to the lower pulse energy measurement, with resonant behavior of the features of interest that is in good agreement with previously detailed iron L-edge resonances. There is, however, some additional resonant behavior of the Auger-Meitner electron LMM lines that can be identified both in the regions 740 eV to 760 eV, as well as the 760 eV to 800 eV range. These two broad ranges match the observations made during the analysis of the iToF spectra
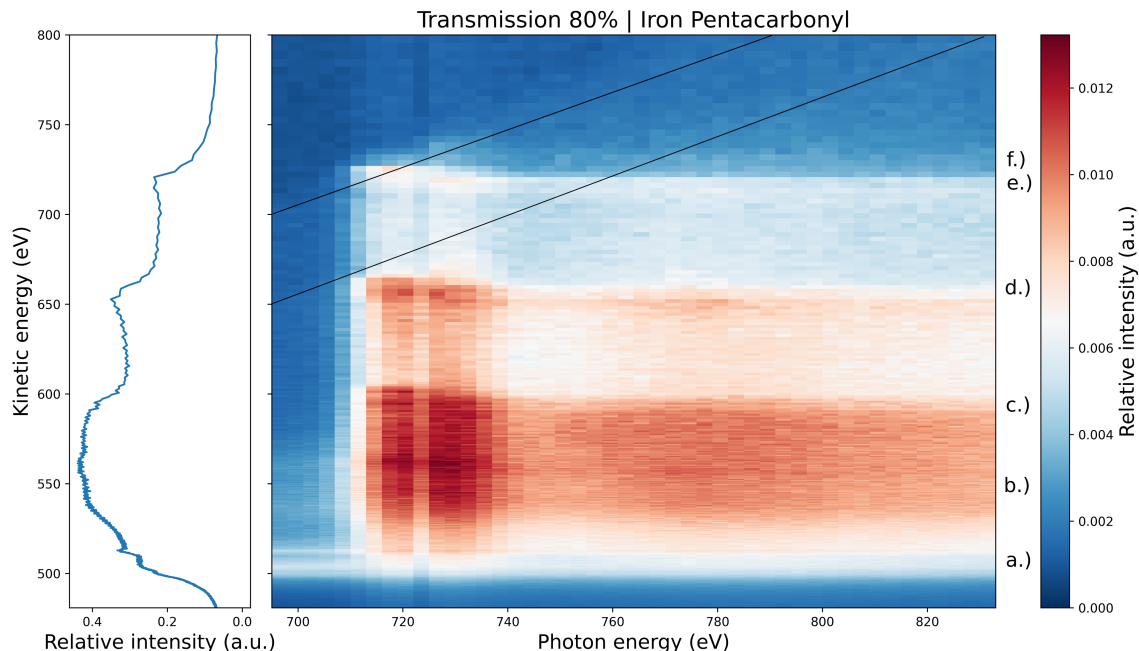
Figure 33: The collection of electron spectra taken of the sample Fe(CO)$_5$ for the photon energy range 695 eV to 830 eV, as recorded by the eToF spectrometer 1 with retardation voltages detailed in TABLE 4. Total signal with respect to the kinetic energy of the detected electrons is shown to the left. GATT transmitted intensity was 10% of maximum requested energy with pulse energies measured by SQS GMD ranging from approximately 480 μJ to 550 μJ. Two photoelectron lines are marked in black. Six Auger-Meitner electron regions are marked with letters $a.)$, $b.)$, $c.)$, $d.)$, $e.)$ and $f.)$.

analysis. These resonances are observed in the Fe $L_{23}M_{23}M_{23}$ and the Fe $L_{23}M_{23}M_{45}$ signals. It is important to note that this additional resonant response is not predicted by the previously modelled SCH relaxation processes for Fe(CO)$_5$. This observation hints at the entire photon energy range being host to non-linear responses, even at 10% of maximum requested pulse energy.

The entirety of the Fe $L_{23}M_{23}M_{23}$ Auger-Meitner electron signal region is hard to identify in the sum signal representation, as there is a variety of resonances overlapping in this region. The presence of electron signal associated with multiply charged iron cations, which was stipulated above, serves as an explanation for the strong low-kinetic energy shoulders of the resonances in FIG. 33 as well. The additional increase in burden in the form of increased signal strength of other species' Auger-Meitner traces of such signals for the Fe $L_{23}M_{23}M_{23}$ signal at 590 eV (marker $c.)$) is noticeably higher than that of the Fe $L_{23}M_{23}M_{45}$ signal at 650 eV (marker $d.)$), which is in turn higher than that of the Fe $L_{23}M_{45}M_{45}$ line at 720 eV (marker $e.)$). As, for the most part, the iron Auger-Meitner electron lines in FIG. 33 are the only ones exhibiting this effect, there seem to be additionally excited multiply charged iron cations present in the interaction region that were inaccessible in the measurement of FIG. 32.

Comparing these observations in the eToF measurement of $Fe(CO)_5$ to the respective iToF measurement of the same sample, conducted with an almost identical pulse energy, reveals the collection of multiply charged iron cations that account for the differences between FIG. 32 and FIG. 33. FIG. 15 includes well identifiable traces of iron cations ranging from Fe^+ to Fe^{10+}.

Figure 34: The collection of electron spectra taken of the sample $Fe(CO)_5$ for the photon energy range 695 eV to 830 eV, as recorded by the eToF spectrometer 1 with retardation voltages detailed in TABLE 4. Total signal with respect to the kinetic energy of the detected electrons is shown to the left. GATT transmitted intensity was 80% of maximum requested energy with pulse energies measured by SQS GMD ranging from approximately 3270 μJ to 3760 μJ. Two photoelectron lines are marked in black. Six Auger-Meitner electron regions are marked with letters $a.)$, $b.)$, $c.)$, $d.)$, $e.)$ and $f.)$.

FIG. 34 displays an increase in the previously observed effects. The CO Auger-Meitner electron signal is still identifiable, yet the entire kinetic energy region is encumbered by additional signal that was not present in previous measurements. This makes an accurate identification of the Fe $L_{23}M_{23}M_{23}$ line at 560 eV more difficult. In fact, the multiple Auger-Meitner lines that now encumber the spectrum result in a higher total signal than even the Fe $L_{23}M_{23}M_{23}$ line marked with $c.)$ at 590 eV. They also appear at lower photon energies than the iron resonance suggests, appearing as early as 695 eV, which hints at this additional signal stemming from the CO. The corresponding kinetic energy regions have been marked with $b.)$

Contrary to the analysis of FIG. 33, these newly present Auger-Meitner electron signals can not be solely attributed to the multiply charged iron cations that are created during the photon-matter interaction. They are readily apparent in all Fe Auger-Meitner electron signals and

show a strong resonant behavior around the photon energy mark of 720 eV, where the L_2 XAS resonance of Fe is according to Godehusen et al. [32]. However, as was discussed above, part of this signal appears at lower photon energies than the iron L-resonance at 713 eV, which calls for an explanation involving another source molecule; CO. The signal is likely a combination of DCH Auger-Meitner electrons excited in direct ionization in CO, superimposed on the Auger-Meitner signal of both DCH and SCH processes in the Fe core of the molecule and the increased charge states also present in the interaction region. The additional lines also appear at lower kinetic energies than the main Fe Auger-Meitner resonances, as can be seen in comparison to TABLE 9. They also appear more prevalent with higher pulse energies. This lends further proof to the hypothesis of this strong additional signal at higher intensities stemming from a mixture of relaxation processes in connection with the creation of multiply charged iron cations and the signal of DCH Auger-Meitner electron stemming from the CO fragment.

In FIG. 33, some additional resonant behavior can be observed in the range from 740 eV to 800 eV for the iron Auger-Meitner lines in the kinetic energy regions marked with $c.$), $d.$), $e.$) . This response is also found in FIG. 34. When comparing the signal of this response to lower pulse energy measurements, the increase in signal strength with respect to the L_2 XAS resonance becomes apparent in all Auger-Meitner lines associated with multiply charged iron cations. Furthermore, a trend towards higher photon energies as resonance onsets with lower kinetic energies of the associated signal can be seen. The affected photon energy regions correspond to the XAS iron cation resonances of Fe^{10+} and higher, yet resolving power does not allow for detailed peak identification in the region of interest.

The total signal of the iron Auger-Meitner signals decreases towards higher kinetic energies. Going along with this, the total signal of those iron Auger-Meitner electron lines that are associated with multiply charged iron cations decreases as well from $L_{23}M_{23}M_{23}$, to $L_{23}M_{23}M_{45}$ and $L_{23}M_{45}M_{45}$. This behavior can be explained by the nature of the Auger-Meitner transitions that are the source of these signals. As the number of M_{45} electrons decreases with higher Fe charge states, so does the number of possible $L_{23}M_{23}M_{45}$ and $L_{23}M_{45}M_{45}$ transitions that give rise to the associated Auger-Meitner electron signals.

Comparing FIG. 35 to the measurement results for lower intensity, a strong similarity in previously identified features to FIG. 34 is visible, with much of the overall intensity being focused in the large swath of Auger-Meitner electron lines in the $L_{23}M_{23}M_{23}$ region. Overall signal intensity slightly increases when compared to FIG. 34.

At higher photon energies than the iron L-edge at 713 eV to 737 eV, the form of the total signal spectrum looks remarkably similar to that particular measurement, including the finer features like additional resonant behavior. Resembling FIG. 34 further is the spread of the additional lines and signal strength within the iron Auger-Meitner regions, with most of the $L_{23}M_{23}M_{23}$ region being drowned in resonant signal lines from 743 eV all the way to 830 eV. The consequent superposition of line signals is even more advanced in this measurement though, with not only the Fe $L_{23}M_{23}M_{23}$ line at 560 eV being barely identifiable, but even the CO O KVV lines mentioned in TABLE 9 being only traceable due to their strong profile at lower photon energies than the the iron L-edge resonance. This entails a shift to even lower kinetic energies for the responsible $L_{23}M_{23}M_{23}$ line, which in turn suggests an even higher iron cation charge state as the responsible source due to shifted energy levels or increased space
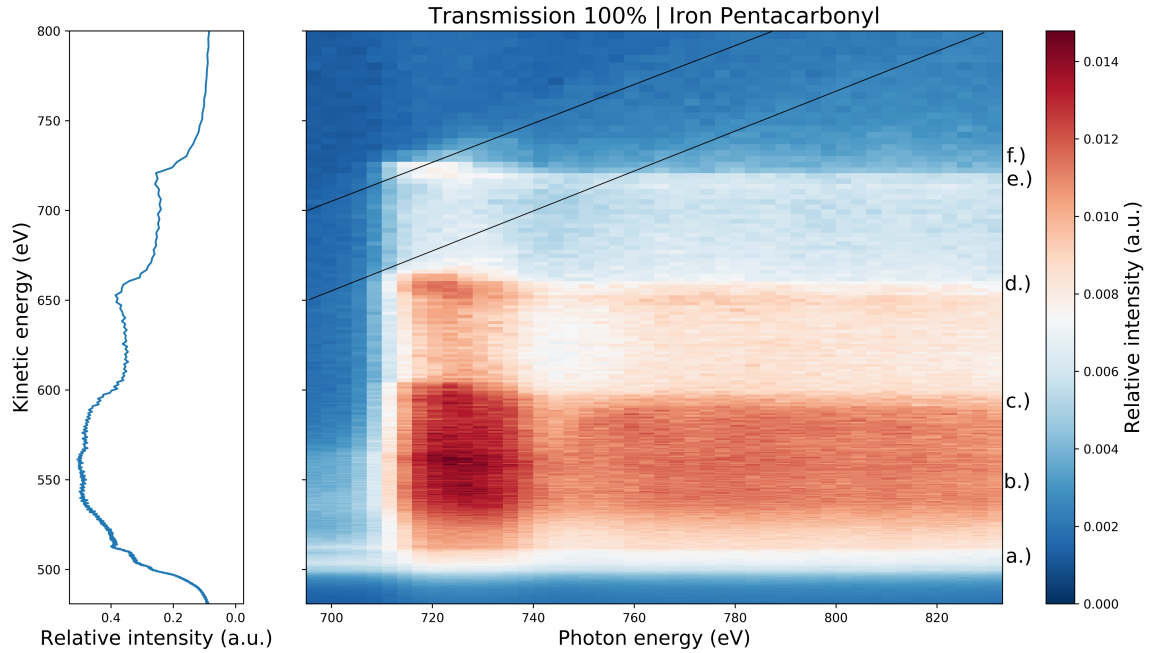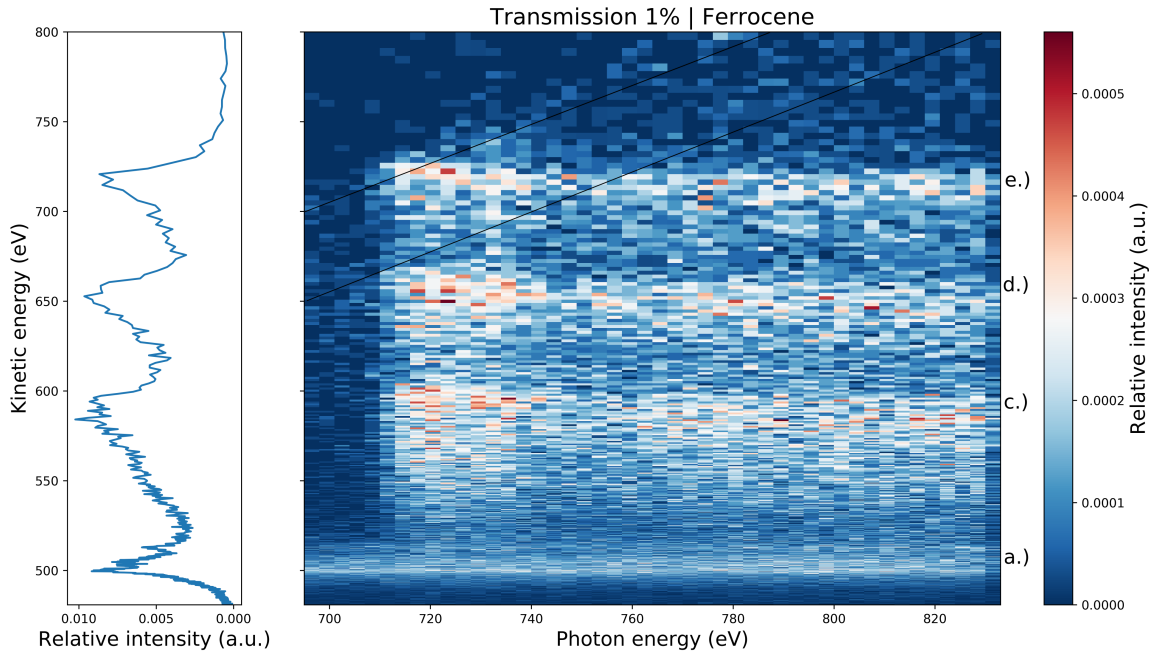
Figure 35: The collection of electron spectra taken of the sample Fe(CO)$_5$ for the photon energy range 695 eV to 830 eV, as recorded by the eToF spectrometer 1 with retardation voltages detailed in TABLE 4. Total signal with respect to the kinetic energy of the detected electrons is shown to the left. GATT transmitted intensity was 100% of maximum requested energy with pulse energies measured by SQS GMD ranging from approximately 3340 µJ to 3840 µJ. Two photoelectron lines are marked in black. Six Auger-Meitner electron regions are marked with letters $a.)$, $b.)$, $c.)$, $d.)$, $e.)$ and $f.)$.

charge effects.

Equally important, the additional resonances that were identified in FIG. 34 are also identified in FIG. 35 and the hypothesis regarding their source is further supported in these measurements. The observed resonance onsets occur at even lower photon energies, as early as 743 eV. Similarly to the discussion above, this is interpreted as the results of iron L-edge excitations occuring not only in the sample, but also the charged iron cations created after the Coulomb explosion within the first fs of the X-ray pulse.

When investigating the iron L-edge lines of FIG. 35 and FIG. 34 closely, the upper kinetic energy limit of the Auger-Meitner signal for each line appears less defined than in FIG. 32 and FIG. 33. This effect is most notable in the Fe $L_{23}M_{45}M_{45}$ Auger-Meitner region between 713 eV and 720 eV. This is the case, because both the $L_{23}M_{23}M_{23}$ line and the $L_{23}M_{23}M_{45}$ signal upper kinetic energy limit are somewhat affected by the additional $L_{23}M_{23}M_{45}$ and $L_{23}M_{45}M_{45}$ Auger-Meitner signals of highly charged iron cations, respectively. In fact, the $L_{23}M_{45}M_{45}$ region is host to an additional signal with a span of roughly 30 eV above the iron pentacarbonyl resonance cutoff that is not part of either photoelectron trace that crosses the region.
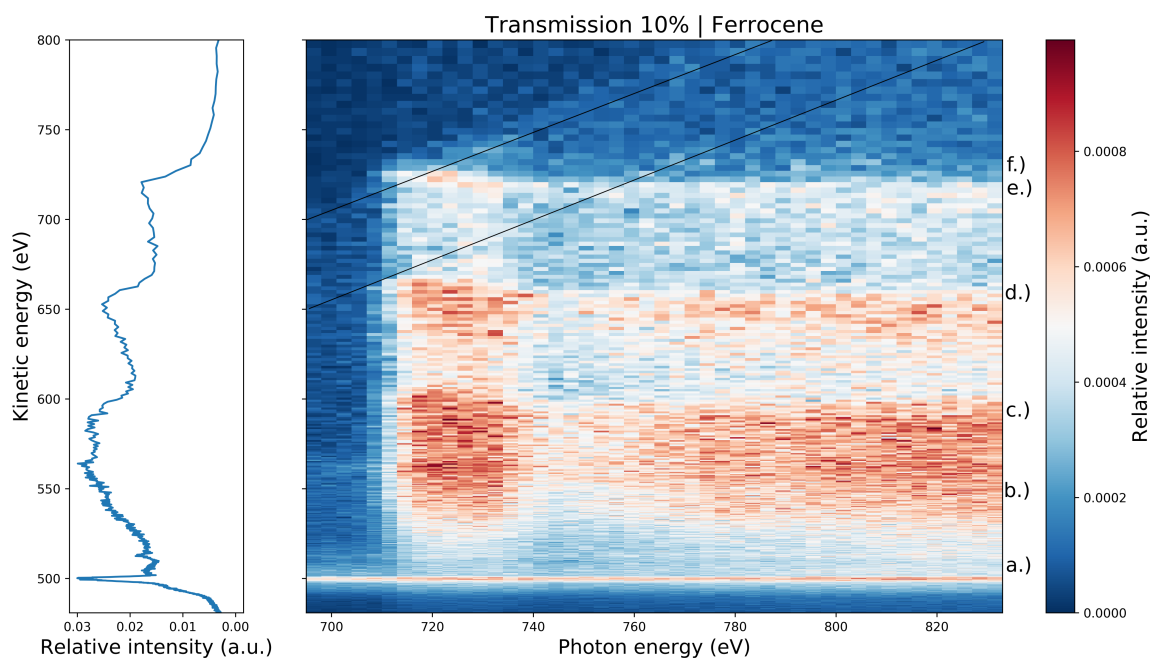
7.2 Electron Spectra of Ferrocene

Figure 36: The collection of electron spectra taken of the sample $Fe(C_5H_5)_2$ for the photon energy range 695 eV to 830 eV, as recorded by the eToF spectrometer 1 with retardation voltages detailed in TABLE 4. Total signal with respect to the kinetic energy of the detected electrons is shown to the left. GATT transmitted intensity was 1 % of maximum requested energy with pulse energies measured by SQS GMD ranging from approximately 60 µJ to 75 µJ. Two photoelectron lines are marked in black. Four Auger-Meitner electron regions are marked with letters *a.*), *c.*), *d.*) and *e.*).

As detailed in Section 4, the measurements on ferrocene were achieved by a different sample transportation method than those for iron pentacarbonyl. This resulted in a somewhat lower resolution, as the helium carrier gas accounted for a decent size of the overall pressure inside the chamber. Consequent lower target concentration in the photon-matter interaction region effects the measurement results presented here, accordingly.

FIG. 36 shows the results of the eToF spectroscopy measurements conducted on ferrocene in the kinetic energy window ranging from 480 eV to 800 eV and the photon energy range from 695 eV to 830 eV. This kinetic energy window enables identification of the iron L-edge Auger-Meitner electron traces as the most prominently displayed signal. Additionally to the four groups of traces of identifiable Auger-Meitner electrons with kinetic energies ranging from 560 eV to 720 eV, two traces of photoelectron lines can be identified by their linear rise with the exciting photon energy. In TABLE 10, they are assigned as the valence photo-lines of the molecule. TABLE 10 also assigns the Auger-Meitner lines of the measurement. The assignments match those for iron pentacarbonyl rather well, with the exception of the valence line and the altered shape of the *K* shell Auger-Meitner oxygen signal that now matches the

Kinetic Energy (eV)	Electronic Transition	Reference Energy (eV)	Literature
500	O_2 KVV	500.5	Caldwell et al. [15]
513.5	O_2 KVV	500.5	Caldwell et al. [15]
536.5	O_2 K^2VV		
559	O_2 K^2VV		
560	Fe $L_{23}M_{23}M_{23}$	560	Allen et al. [2]
590	Fe $L_{23}M_{23}M_{23}$	590	Allen et al. [2]
650	Fe $L_{23}M_{23}M_{45}$	650	Allen et al. [2]
720	Fe $L_{23}M_{45}M_{45}$	710	Allen et al. [2]
747.5	Fe $L_{23}^2M_{45}M_{45}$		
650	Fe M_{23}	648	
700	$Fe(C_5H_5)_2$ V	699	

Table 10: The Auger-Meitner- and photoelectron assignment of the traces identified in FIG. 36. The associated kinetic energies are in good agreement with previous works by Caldwell et al. and Allen et al. The literature used for the assignment of the particular trace are shown as a reference.

works of Caldwell et al. on molecular and atomic oxygen more than that of the CO molecule, due to its multi-peak features.

The aforementioned O Auger-Meitner electron lines are present at every photon energy. The electron signals associated with the Fe constituent, however, show strong resonant responses at photon energy ranges from 713 eV to 737 eV. This range is the same for all Auger-Meitner lines and matches the resonant regions in the iron pentacarbonyl measurement very well. The resonant behavior displayed here is quite strong and overlaps with the signal of both Fe photon lines. In a stark difference in the appearance of the electron signal, the Auger-Meitner trace at 560 eV is quite pronounced for ferrocene, whereas in measurements on iron pentacarbonyl it could barely be resolved in the total signal. In turn, the signal of the $L_{23}M_{23}M_{23}$ Auger-Meitner electron trace at 590 eV could be resolved less well, with the two peak structure that matches the work of Allen et al. less recognizable than in the other sample [2]. The same is not true for the $L_{23}M_{23}M_{45}$ signal at 650 eV, where the peak form presented by Allen et al. is recreated in this measurement almost identically.

Despite the lower overall intensity in the ferrocene measurement, the influence of onsetting Auger-Meitner relaxation product electrons for multiply charged Fe cations in the interaction region is present in FIG. 36 as well. For the Fe $L_{23}M_{23}M_{23}$ signal, the 560 eV electron line's more intensive presence is apparent. It is less pronounced for the Fe $L_{23}M_{23}M_{45}$ and Fe $L_{23}M_{45}M_{45}$ Auger-Meitner traces.

FIG. 37 shows the product electrons of ferrocene for pulse energies ranging from 470 μJ to 610 μJ. The line assignments presented in TABLE 10 can be easily found at the same kinetic energies as in FIG. 36. Overall, the signal appears similar to the lower pulse energy measurement, with resonant behavior of the features of interest that is in good agreement with previously detailed iron L-edge resonances.

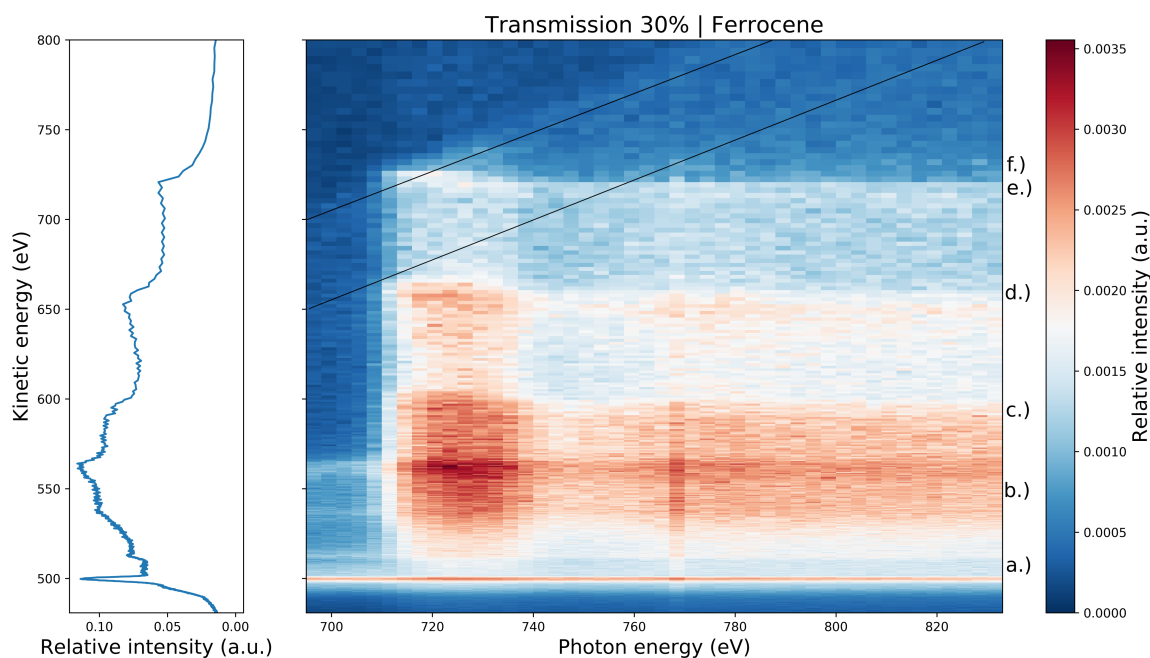There is, however, some additional resonant behavior of the Auger-Meitner electron *LMM*

Figure 37: The collection of electron spectra taken of the sample $Fe(C_5H_5)_2$ for the photon energy range $695\,eV$ to $830\,eV$, as recorded by the eToF spectrometer 1 with retardation voltages detailed in TABLE 4. Total signal with respect to the kinetic energy of the detected electrons is shown to the left. GATT transmitted intensity was $10\,\%$ of maximum requested energy with pulse energies measured by SQS GMD ranging from approximately $470\,\mu J$ to $610\,\mu J$. Two photoelectron lines are marked in black. Six Auger-Meitner electron regions are marked with letters $a.)$, $b.)$, $c.)$, $d.)$, $e.)$ and $f.)$.

lines that can be identified in the regions $740\,eV$ to $820\,eV$ range. This matches the observations made during the analysis of the iToF spectra analysis to some degree. These additional resonances are most easily observed in the Fe $L_{23}M_{23}M_{23}$ ($b.), c.)$) and the Fe $L_{23}M_{23}M_{45}$ ($d.)$) signals. Here, the shape of the additional resonant features can be seen as tending toward lower photon energies as the kinetic energy of the Auger-Meitner electrons increases. It is important to note, that this additional resonant response is not predicted by the expected SCH relaxation processes for $Fe(C_5H_5)_2$ and hints at the entire photon energy range being host to non-linear responses, even at 10% of maximum requested pulse energy. Similarly to the corresponding measurement on iron pentacarbonyl, the affected photon energy range matches that of the multiply charged iron cations in the iToF spectrum.

The Fe $L_{23}M_{23}M_{23}$ Auger-Meitner electron signal is much easier to identify in the sum signal representation than it is for iron pentacarbonyl and constitutes a local maxima in the spectrum. The additional increase in burden of such signals for the Fe $L_{23}M_{23}M_{23}$ signal at $590\,eV$ is noticeably higher than that of the Fe $L_{23}M_{23}M_{45}$ signal at $650\,eV$, which is in turn higher than that of the Fe $L_{23}M_{45}M_{45}$ line at $720\,eV$. This matches the features observed in iron pentacarbonyl for the 10% measurement.
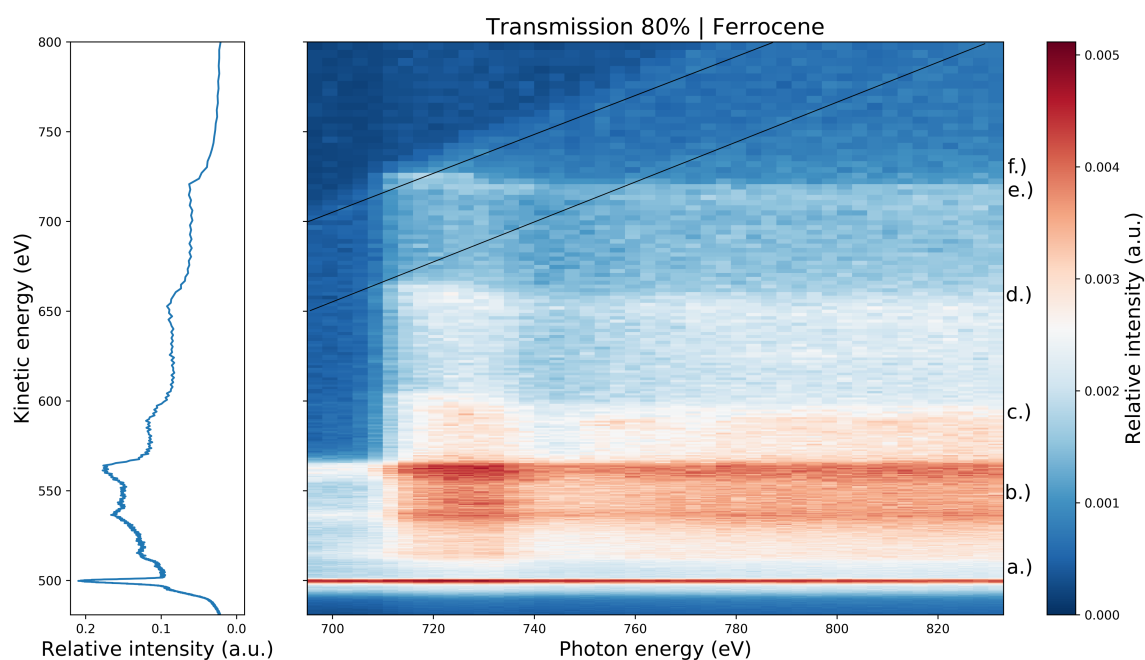
Figure 38: The collection of electron spectra taken of the sample $Fe(C_5H_5)_2$ for the photon energy range $695\,eV$ to $830\,eV$, as recorded by the eToF spectrometer 1 with retardation voltages detailed in TABLE 4. Total signal with respect to the kinetic energy of the detected electrons is shown to the left. GATT transmitted intensity was 30% of maximum requested energy with pulse energies measured by SQS GMD ranging from approximately $800\,\mu J$ to $1090\,\mu J$. Two photoelectron lines are marked in black. Six Auger-Meitner electron regions are marked with letters $a.$), $b.$), $c.$), $d.$), $e.$) and $f.$).

FIG. 38 shows the ferrocene electron spectrum in the iron L-edge region of interest for pulse energies ranging from $800\,\mu J$ to $1090\,\mu J$. In comparison to the measurements conducted with less X-ray pulse energy, the number of identifiable Auger-Meitner lines that appear before the iron L-edge resonance increases from one to four, with the three new traces falling within the kinetic energy region occupied by the signal partly attributed to multiply charged iron cations. Furthermore, the one with the highest kinetic energy neatly overlaps with the resonant Auger-Meitner signal maximum at $560\,eV$. The measurement reinforces the previous observations on the differences in the Auger-Meitner relaxation processes in the two samples with a clear local maximum at $560\,eV$ and the differences in the shape of the Fe $L_{23}M_{23}M_{23}$ features in general. Whereas good agreement in shape, position and form exists for both samples in the Fe $L_{23}M_{23}M_{45}$ and Fe $L_{23}M_{45}M_{45}$ region, here the local maxima are vastly different with electron signals of lower kinetic energy being favored as products of the relaxation processes.

In the observations regarding the additional resonant behavior at higher photon energies and the signal attributed to multiply charged iron cations, the measurement neatly adds to the existing observations and agrees rather well. Even additional resonance onsets trending towards higher photon energy with lower kinetic energy can be observed in the Fe $L_{23}M_{23}M_{23}$

response in this measurement.

There is, however, a part of the measurement that does not readily agree with the analysis as it stands so far. The Auger-Meitner signal assigned to the O K shell appears to show resonant behavior in both photon energy regions previously reserved for the iron L-edge responses of the sample molecule. This oddity can be explained as a mixture between the generally strong O KVV trace and contributions from multiply charged iron cations. The trace is thus no longer singly occupied and the resonant behavior explained as resonant behavior of highly charged iron cations.

Figure 39: The collection of electron spectra taken of the sample $Fe(C_5H_5)_2$ for the photon energy range 695 eV to 830 eV, as recorded by the eToF spectrometer 1 with retardation voltages detailed in TABLE 4. Total signal with respect to the kinetic energy of the detected electrons is shown to the left. GATT transmitted intensity was 80% of maximum requested energy with pulse energies measured by SQS GMD ranging from approximately 2470 µJ to 3130 µJ. Two photoelectron lines are marked in black. Six Auger-Meitner electron regions are marked with letters $a.)$, $b.)$, $c.)$, $d.)$, $e.)$ and $f.)$.

FIG. 39 shows the response of the sample to irradiation of X-ray pulses with pulse energies in the mJ regime. A first observation is the apparent lack of resonant behavior in the O KVV region for this measurement. The spectrum emphasizes the emergence of the three additionaly identifiable Auger-Meitner traces, each showing a strong resonance in the iron $L_{23}M_{23}M_{23}$ region. Excepting the Auger-Meitner trace associated with oxygen, these traces are the most intensive in the spectrum. While the $L_{23}M_{23}M_{45}$ region and the $L_{23}M_{45}M_{45}$ region continue to resemble the iron pentacarbonyl measurement rather well, the $L_{23}M_{23}M_{23}$ region thus continues to diverge in what electronic states are favored. As these additional

$L_{23}M_{23}M_{23}$ iron Auger-Meitner signals are found at lower kinetic energies than the ferrocene $L_{23}M_{23}M_{23}$ Auger-Meitner signals at lower pulse energies, they could be the result of photon-matter interactions in multiply charged iron cations. The overall lower amount of ferrocene in the interaction region emphasizes the measured effect of this contribution.

When comparing the signal of this measurement to lower pulse energy measurements, the increase in signal strength with respect to the L_2 XAS resonance becomes apparent in all Auger-Meitner lines associated with multiply charged iron cations. This behavior matches the observations made in iron pentacarbonyl. Furthermore, close inspection reveals a similar trend towards higher photon energies as resonance onsets with lower kinetic energies of the associated signal. The affected photon energy regions correspond to the XAS iron cation resonances of Fe^{10+} and higher, yet resolving power does not allow for associating certain signal lines to specific cationic partners in the region of interest.

Similarly to the corresponding measurement in iron pentacarbonyl, total signal of the iron Auger-Meitner signals decreases towards higher kinetic energies. The total signal of those iron Auger-Meitner electron lines that are associated with multiply charged iron cations decreases as well from $L_{23}M_{23}M_{23}$, to $L_{23}M_{23}M_{45}$ and $L_{23}M_{45}M_{45}$. The explanation for this behavior is the same as for iron pentacarbonyl: As the number of M_{45} electrons decreases with higher Fe charge states, so does the number of $L_{23}M_{23}M_{45}$ and $L_{23}M_{45}M_{45}$ transitions that give rise to the associated Auger-Meitner electron signals.

FIG. 40 shows measurements taken at even higher pulse energies than FIG. 39. The three additional Auger-Meitner traces in the $L_{23}M_{23}M_{23}$ region are the strongest resonances in this measurement in the total signal representation. The previously noted strong O KVV Auger-Meitner signal shows resonant behavior in the iron $L_{23}M_{23}M_{23}$ region. In this measurement, the iron Auger-Meitner traces that coopt the time-of-flight channel associated with this O KVV line are clearly identifiable on the upper and lower edges of the otherwise sharp oxygen signal. This increased visibility is partly due to its comparatively smaller intensity, as compared to the measurement in FIG. 39. Yet the clearly visible resonant behavior of the broad edge regions not only above, but also below the line suggest that the iron Auger-Meitner electron signal's shift toward lower kinetic energies is even larger in this measurement than in FIG. 39 or the measurements with even lower pulse energies.

This observation holds equally true for the iron $L_{23}M_{23}M_{45}$ region as well. Whereas additional resonances at higher photon energies are restricted to photon energies upward of 757 eV or higher in measurements with lower pulse energies, they start closer to 745 eV in this measurement and this region. Additionally, fewer individual additional traces are identifiable by their outline, as the region above the $L_{23}M_{23}M_{23}$ cutoff at around 610 eV is occupied by a swath of Auger-Meitner lines in the shape of the main $L_{23}M_{23}M_{45}$ resonance. These effects are less pronounced in the $L_{23}M_{45}M_{45}$ region, but nevertheless visible, particularly in comparison to measurements of lower pulse energies.

At higher pulse energies in FIG. 40, additional resonant behavior can be identified in regions above the kinetic energy cutoff of the $L_{23}M_{45}M_{45}$ resonance associated with the primariy ferrocene target. While they are present in FIG. 39, they are harder to differentiate from the photo-lines that cross the region. In FIG. 40, however, this additional signal can be traced to the photo energy region ranging from 740 eV to approximately 775 eV. In both photon energy region and kinetic energy region, this signal appears similar to the same effect observed in
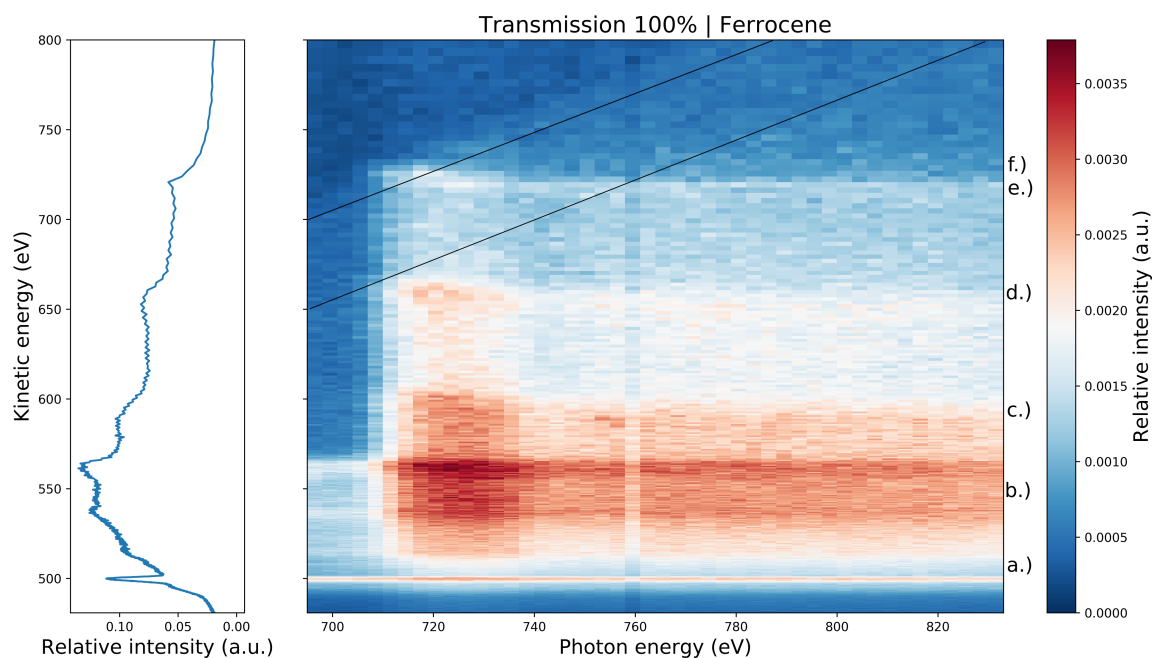
Figure 40: The collection of electron spectra taken of the sample $Fe(C_5H_5)_2$ for the photon energy range 695 eV to 830 eV, as recorded by the eToF spectrometer 1 with retardation voltages detailed in TABLE 4. Total signal with respect to the kinetic energy of the detected electrons is shown to the left. GATT transmitted intensity was 100% of maximum requested energy with pulse energies measured by SQS GMD ranging from approximately 3350 μJ to 3850 μJ. Two photoelectron lines are marked in black. Six Auger-Meitner electron regions are marked with letters $a.$), $b.$), $c.$), $d.$), $e.$) and $f.$).

the iron pentacarbonyl measurements of high pulse energies. In the photon energy region, this also overlaps with some of the additional resonances observed for lower kinetic energies than the corresponding ferrocene resonance. However, no higher kinetic energies than the $L_{23}M_{45}M_{45}$ resonance are expected for higher kinetic energies and iron cations according to FIG. 6. Furthermore, the photon energy region includes the area previously identified as a potential region of interest for DCH Auger-Meitner electrons in FIG. 7.

8 DCH Processes in Iron Pentacarbonyl and Ferrocene

The presented results in Section 5 and Section 7 offer evidence for DCH processes in the $3d$ iron complexes iron pentacarbonyl and ferrocene. In utilizing the calculations of Section 3 in addition to the collected ion- and electron-spectra, this evidence is combined. The electron results for both samples are evaluated within the identified regions with a strong focus on the *LMM* Auger-Meitner electrons of the iron center. In order to achieve a thorough perspective on the various ultra-fast processes occurring in the time frames of the experiment, starting at the most easily identifiable trace of DCH Auger-Meitner electrons is prudent. The results can be used to gauge the relative scales between SCH and DCH products in the experiment. Ion spectra and estimated SCH spectra are then used to test the more obscured DCH Auger-Meitner electron trace regions. To confirm the quadratic scaling expected of a double core-hole Auger-Meitner electron signal, additional pulse energy regions are considered in this testing procedure by using the SASE fluctuations. As these pulse energy bins can deviate in counts for each observable, the corresponding error margins may increase. This is shown, where appropriate, by the individual error bars of each data point.

Quadratic fits of the forms $y = ax^2 + bx + c$, $y = ax^2 + bx$ and $y = ax^2$ are used in this chapter to show non-linearity at several instances. These fits are conducted with an enforced condition of positive, non-zero coefficients. They employ a reduced chi square approach in evaluating goodness of fit. As a $y = ax^2$ fit is usual to show non-linear signal increase with pulse energy, both $y = ax^2 + bx$ and $y = ax^2$ are sometimes shown despite not conforming to the data well. This serves to reinforce the argument for a $y = ax^2 + bx + c$ fit treatment of the data in order to account for linear and constant backgrounds.

8.1 Double Core-Hole Electron Spectroscopy of the Oxygen K^2VV Auger-Meitner Lines for Ferrocene and Iron Pentacarbonyl

In Section 7, multiple Auger-Meitner electron lines were identified and assigned to a double core-hole in an oxygen containing molecule (CO, O) for both samples iron pentacarbonyl and ferrocene, respectively. The Auger-Meitner electron lines were easy to identify in the photon energy regions around 695 eV, as the electron spectrum is free of any single- or double-core-hole iron Auger-Meitner lines.

FIG. 41 shows the electron spectra taken at 695 eV photon energy of both samples. The kinetic energy region shaded in red corresponds to the Auger-Meitner electron signal of the DCH *KVV* transition for the carbon monoxide in iron pentacarbonyl and the suspected residual water that contaminated the AQS chamber in ferrocene and produces an atomic oxygen DCH signature. Both signals are observed to vanish at low pulse energies and exhibit a somewhat comparable feature form to the SCH Auger-Meitner electron signal associated with the oxygen lines in both samples. A shift of 15 eV in kinetic energy was observed between the slowest identifiable feature of the DCH signal and the fastest feature of the SCH signal.

The DCH-attributed features differ vastly between the measurements in both samples but show good congruity with measurements of differing pulse energies within the same sample. This strong difference between both samples is illustrated in FIG. 42. It can be explained by
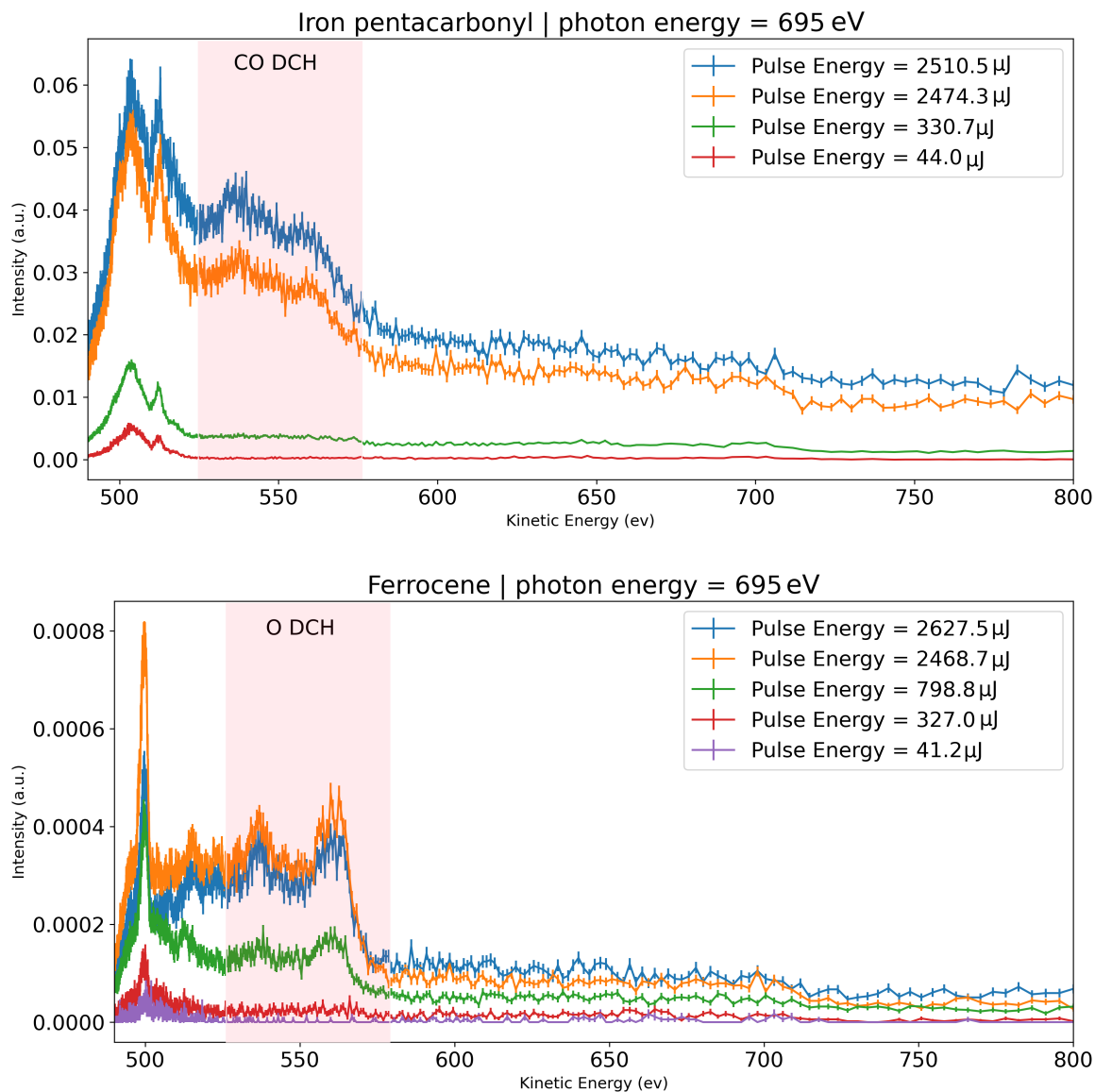
Figure 41: The electron spectra of iron pentacarbonyl and ferrocene for the photon energy 695 eV. The kinetic energy region assigned to the Auger-Meitner electron signal of the oxygen K^2VV is shaded red in both spectra and titled with the corresponding molecular fragment. The spectrum is mostly free of iron Auger-Meitner electron signal and reveals the strong differences in the oxygen Auger-Meitner form and strength in both samples.
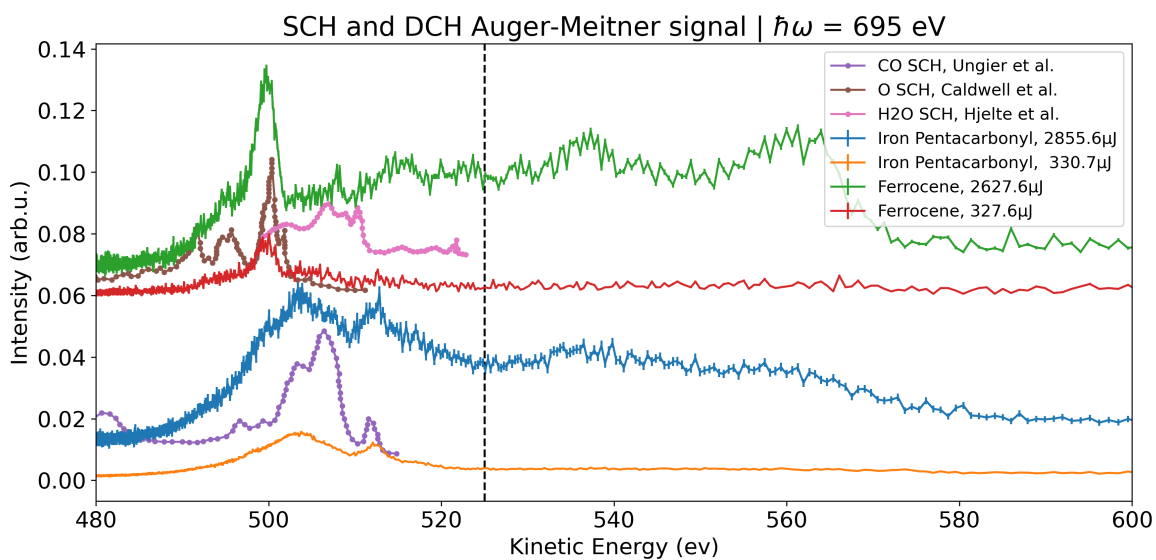
Figure 42: The electron spectra of iron pentacarbonyl (bottom) and ferrocene (top) for the photon energy 695 eV for two selected pulse energies. The spectra reported by Ungier et al. [94], Hjelte et al. [37] and Caldwell et al. [15] are shown as references for the CO, H_2O and O lines respectively. The CO line has been shifted by 1 eV to account for the molecular environment based on the findings of Stucky et al. [91]. A vertical line has been included as a guide to the eye to indicate the onset of DCH features. The DCH-attributed feature forms differ quite strongly between the two samples, which suggests CO to be the primary source of O DCH processes in iron pentacarbonyl and both O and H_2O to play a role in the O DCH processes in ferrocene.
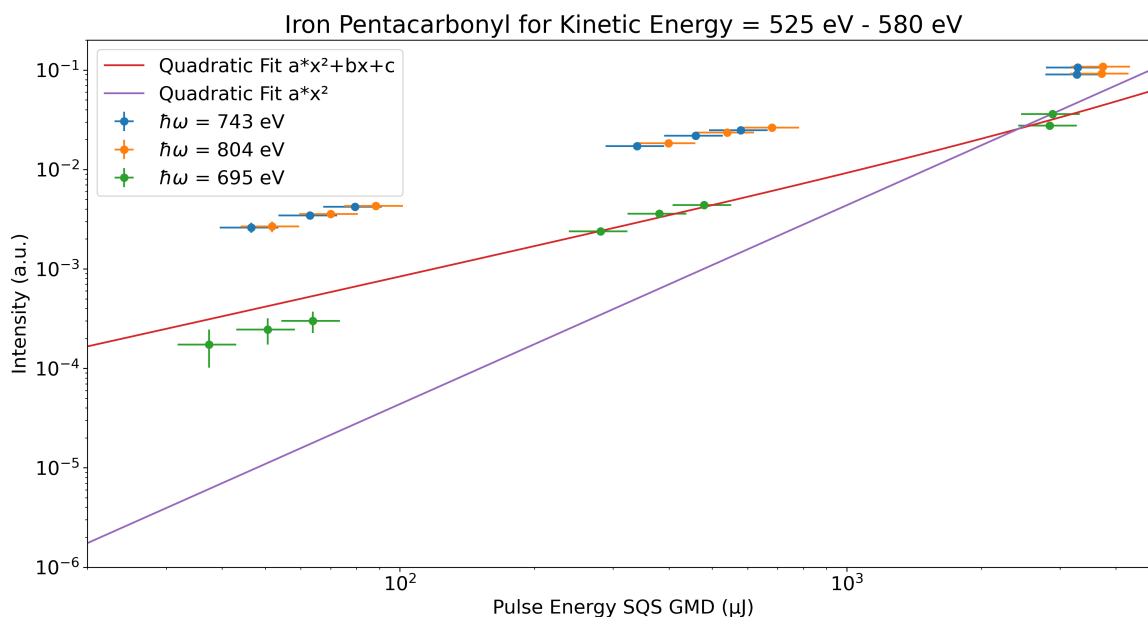
Figure 43: The Auger-Meitner electron signal mean for the kinetic energy region of interest from $525\,\text{eV}$ to $580\,\text{eV}$ for relaxation after the creation of a carbon monoxide K^2 hole at the oxygen site in the iron pentacarbonyl sample, displayed for the photon energies $695\,\text{eV}$, $743\,\text{eV}$ and $804\,\text{eV}$. Horizontal bars account for the pulse energy interval covered in each measurement, while vertical error bars account for signal intensity uncertainty. Quadratic fits to the $695\,\text{eV}$ measurement of the form $y = ax^2$ and $y = ax^2 + bx + c$ are also displayed as a guide for the eye.

the presence of oxygen in CO, which is a major part of the molecular makeup of the iron pentacarbonyl molecule. Oxygen is not present in the ferrocene chemical environment and is only present in the interaction region due to the choice of sample delivery and the presence of residual gas in the chamber. This is likely H_2O. With regard to this, what is observed is then the DCH Auger-Meitner electron signal of CO, H_2O and O after an oxygen K^2 double core-hole is created in the respective molecules. The presence of O in this interaction zone could be created by the ionization of H_2O and its dissociation after irradiation. The kinetic energy regions identified in this work, at least for the case of the ferrocene sample, match the results of the work by Marchenko et al. [54] and the references contained therein, in which they investigate the double core-hole formation and ultrafast processes in the water molecule. Unfortunately, at the time of this work, a closer investigation of the Auger-Meitner relaxation after double core-hole creation via two-photon absorption in other oxygen containing molecules, such as the carbon monoxide fragment, which is suspected to be responsible for the DCH signature in iron pentacarbonyl, has not been published yet. Despite not offering information on the ferrocene molecule itself, the DCH signature of oxygen in the corresponding measurements offer valuable insights to the intensity dependence of the signal on the pulse energy of the measurement.

FIG. 43 shows the mean of signal intensity for the kinetic energy region associated with

the DCH Auger-Meitner electron signal in relation to the associated pulse energy for three photon energies, 695 eV, 743 eV and 804 eV. The signal in the sample iron pentacarbonyl evolves along the implied rise of the shown quadratic fit, but aligns much better with the full quadratic fit than the $y = ax^2$ line on the log-log scale. Despite a good identification of DCH associated signal, the traditionally used fit $y = ax^2$ with respect to the pulse intensity does not conform well to the data. For the photon energy 695 eV, it was observed that measurements at the lower end of the pulse energy scale seem to deviate further from the fit than at the higher pulse energy measurement end. These deviations tend toward lower signal intensities. For the earlier data points on the energy scale, the purely quadratic rise of the $y = ax^2$ line seems to describe the non-linear relation to pulse energy better. While not presented with a corresponding fit in FIG. 43, the same observation cannot be made for both other displayed photon energies. For these two measurement series, at 743 eV and 804 eV photon energy, the lack of these deviations could be explained by the overlapping SCH Auger-Meitner electron signal from the Fe resonance in both samples, the $L_{23}M_{23}M_{23}$ region thoroughly overlapping with the kinetic energy region studied in FIG. 43 and increasing the linear contribution for low pulse energy measurements.

For the measurement series at the photon energy of 695 eV, SCH Auger-Meitner electron signal of Fe cannot explain the observed trend, as the measurement is conducted pre-iron resonance. The fit suggests that an accurate model for the evolution of the DCH Auger-Meitner electron signal intensity involves a linear contribution in these experimental conditions, as well as a potential background offset. Any deviations towards higher and lower signal intensities, respectively, correct the associated mix of linear and quadratic coefficients.

FIG. 44 shows the mean of signal intensity for the kinetic energy region associated with the DCH Auger-Meitner electron signal in relation to the associated pulse energy for three photon energies, 695 eV, 743 eV and 804 eV in the ferrocene sample. These measurements align in their results with the observations made for iron pentacarbonyl. For all photon energies, signal intensity evolves along the implied rise of the shown full quadratic fit with pulse energy, to a degree that strongly suggests a quadratic relation being the underlying model.

Contrary to what was observed in FIG. 43, low pulse energy measurements deviate towards lower signal intensities and high pulse energy measurements deviate towards higher signal intensities from the predictions of a full quadratic model. Whereas in iron pentacarbonyl, high pulse energy measurements suggested a good agreement with the fit in terms of signal scaling, FIG. 44 suggests some high pulse energy measurements deviate toward higher signal intensities than the fit implies. As in the iron pentacarbonyl, these observations suggest a stronger quadratic contribution in some pulse energy areas, than is accounted for by the overall coefficients of the fit.

One way to account for these observations in the fit without appealing to effects of the chemical environment of the sample is to increase the weights of low pulse energy measurements by arguing that the high pulse energy measurements are subject to higher space charge effects. This would effect a larger quadratic coefficient for the ferrocene sample, and a smaller quadratic coefficient for the iron pentacarbonyl sample. Due to the potential error being larger for low pulse energy measurements, high pulse energy data points influence the fit to a higher degree. This, however, does not account for potential saturation or depletion effects at high pulse energies that could affect signal intensity, which have been shown to play an increasingly
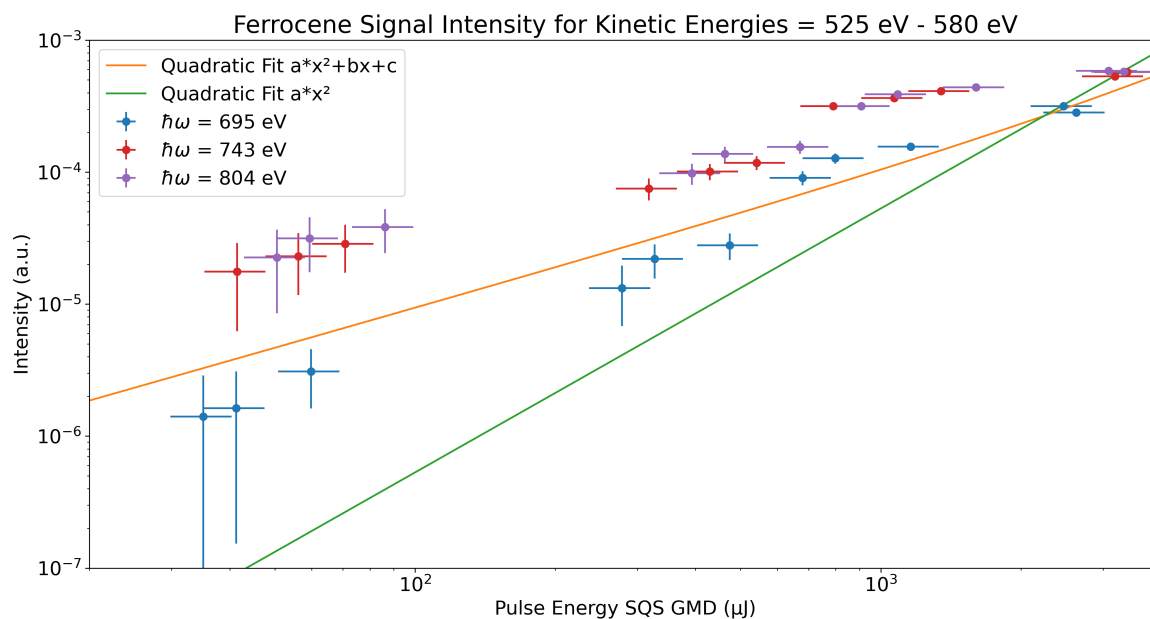
Figure 44: The ferrocene Auger-Meitner electron signal mean for the kinetic energy region of interest for relaxation after the creation of an atomic oxygen K^2 hole in a cationic product fragments of the background H_2O, displayed for the photon energies 695 eV, 743 eV and 804 eV. Horizontal bars account for the pulse energy interval covered in each measurement, while vertical error bars account for signal intensity uncertainty. Quadratic fits of the form $y = ax^2$ and $y = ax^2 + bx + c$ to the 695 eV measurement are also displayed.

important role at high pulse energies in Section 6.

8.2 Double Core-Hole Electron Spectroscopy of the $L_{23}M_{45}M_{45}$ Auger-Meitner Lines for Ferrocene and Iron Pentacarbonyl

Section 7 identified a region of significant interest in the Fe $L_{23}M_{45}M_{45}$ region of the obtained Auger-Meitner electron spectra in both samples. In the photon energy range, this region extends from 740 eV to 775 eV and in the kinetic energy range, this region extends from approximately 725 eV to 760 eV. This excludes photoelectron traces in the region.

FIG. 45 shows a comparison between three photon energies at high pulse energy for both samples. The $L_{23}M_{45}M_{45}$ region, between 725 eV and 760 eV kinetic energy, shows an additional broad signal range. An increase in signal and kinetic energy width is shown clearly for the photon energy 713 eV and the SCH Auger-Meitner electron signal peaks around 720 eV, 650 eV and 600 eV kinetic energy. This feature of on-resonance measurements at 713 eV photon energy is mirrored in the DCH resonant Auger-Meitner signal in the $L_{23}M_{45}M_{45}$ region, where the resonant photon energy signal outscales the others at the same pulse energy.

A self-consistency test is performed for all pulse energy settings and both samples. In subtracting the SCH resonance spectrum taken at 713 eV excitation energy from an exemplary spectrum within the region of interest, in this case the spectrum taken at 743 eV, the kinetic energy regions of the double core-hole Auger-Meitner signal becomes more apparent. Choosing exemplary photon energy lines to consider certain kinetic energy regions in more detail follows the approach of Dimitris Koulentianos, who used a similar approach in their work on $K^{-2}V$ double-core-hole states in C_4H_{10} [42]. FIG. 46 shows the results of comparing the SCH resonant electron spectrum (713 eV) to the DCH resonant electron spectrum (743 eV) in the previously defined region of interest. In both samples, the Auger-Meitner electron signal associated with the $L_{23}M_{45}M_{45}$ transition is more intense in the SCH resonant spectrum than in the DCH resonant spectrum. This difference is amplified significantly for higher pulse energies. The region of the SCH Auger-Meitner electron trace can be well resolved in this representation and occupies the kinetic energy region from 720 eV to 735 eV as the dip in signal intensity results from comparing a DCH resonant photon energy to an SCH resonant photon energy and the shifts in energy inherent in such a comparison.

The second feature of this representation is a pulse energy dependent increase in signal for the kinetic energy region between 737 eV and 765 eV. This region includes kinetic energies associated with the rising photoelectron traces identified in Section 7. They can be resolved with an onset at 760 eV. The remaining signal portion covers the predicted kinetic energy regions for $L_{23}M_{45}M_{45}$ Auger-Meitner electrons resulting from a DCH excitation in an isolated iron atom presented in FIG. 7. The kinetic energy region, extended by approximately 10 eV in comparison to the calculated spectrum and the kinetic energy shift of the feature onset can be attributed to the sample in this interpretation. This presents strong evidence for the assignment of the 735 eV to 760 eV kinetic energy region to the $L_{23}M_{45}M_{45}$ Auger-Meitner electrons of Fe for the on-resonance signal at the exemplary photon energy of 743 eV.

In a next step, FIG. 47 shows the results of first integrating the collective signal over this kinetic energy region for every step in the photon energy region 680 eV to 800 eV. Then

95
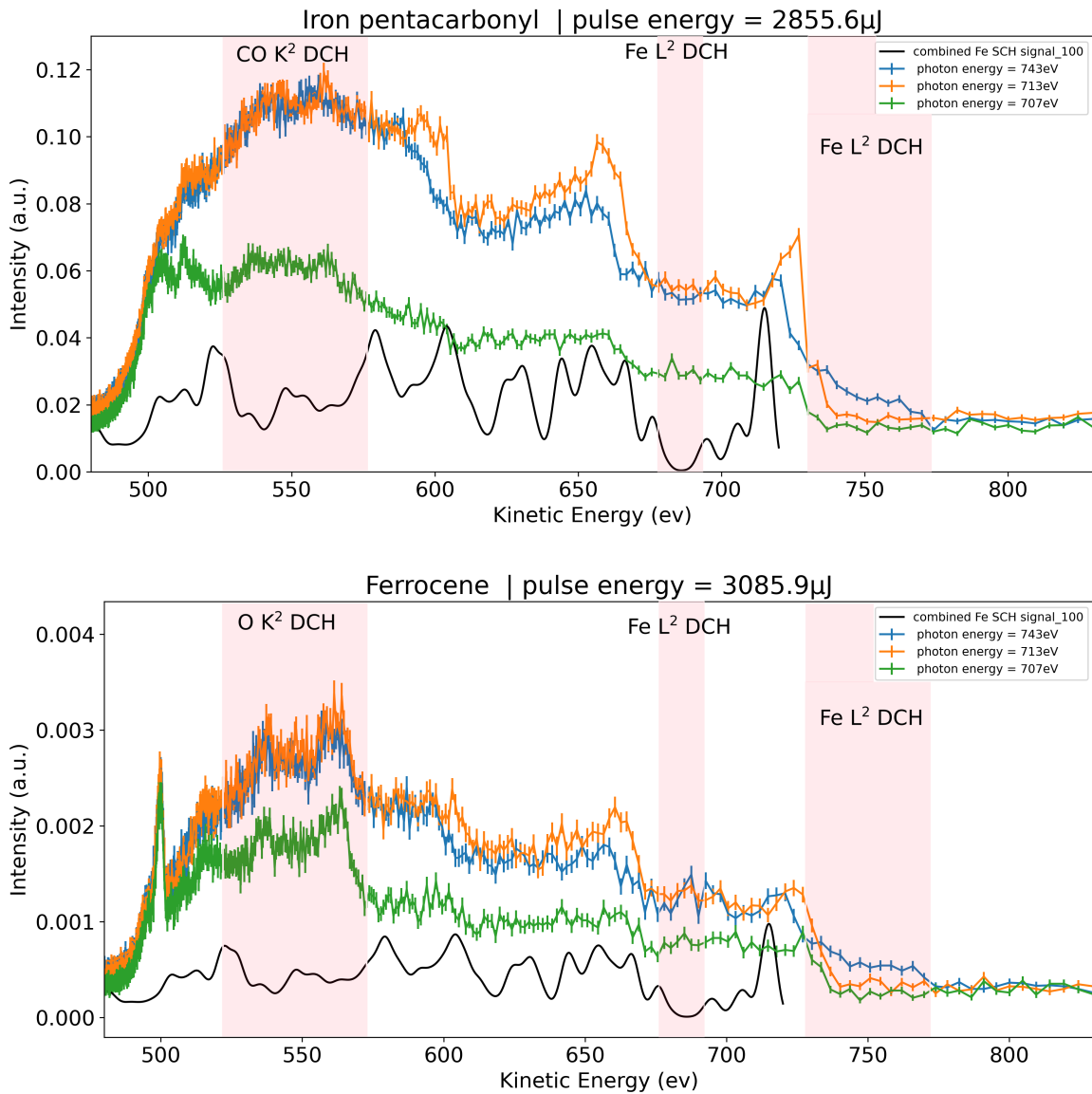
Figure 45: The electron spectra of iron pentacarbonyl and ferrocene for high pulse energy measurements and for various photon energies. The kinetic energy region assigned to the Auger-Meitner electron signal of the oxygen K^2VV, the Auger-Meitner electron signal of the DCH iron $L_{23}M_{23}M_{23}$, the Auger-Meitner electron signal of the DCH iron $L_{23}M_{23}M_{45}$ and the Auger-Meitner electron signal of the DCH iron $L_{23}M_{45}M_{45}$ are all shaded in red in both spectra and titled with the corresponding site and process. The spectra are a combination of iron Auger-Meitner and oxygen Auger-Meitner electron signal. It reveals the strong differences in the Auger-Meitner form and strength in the photon energy 743 eV for the kinetic energy region between 725 eV and 760 eV .

(a) Sample Fe(CO)$_5$

(b) Sample Fe(C$_5$H$_5$)$_2$
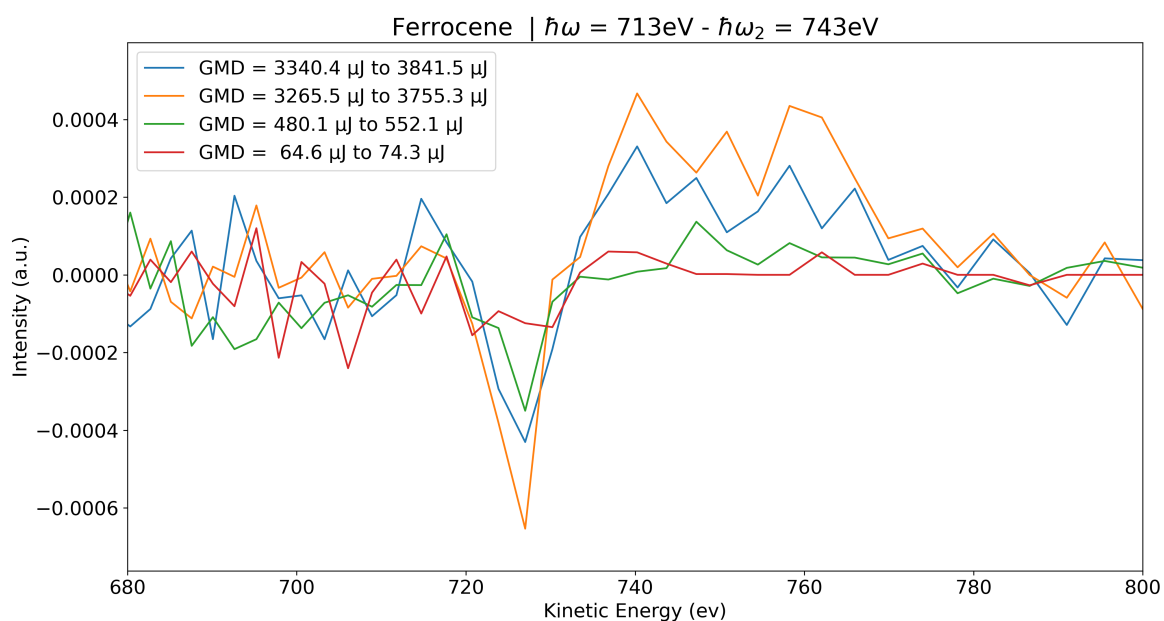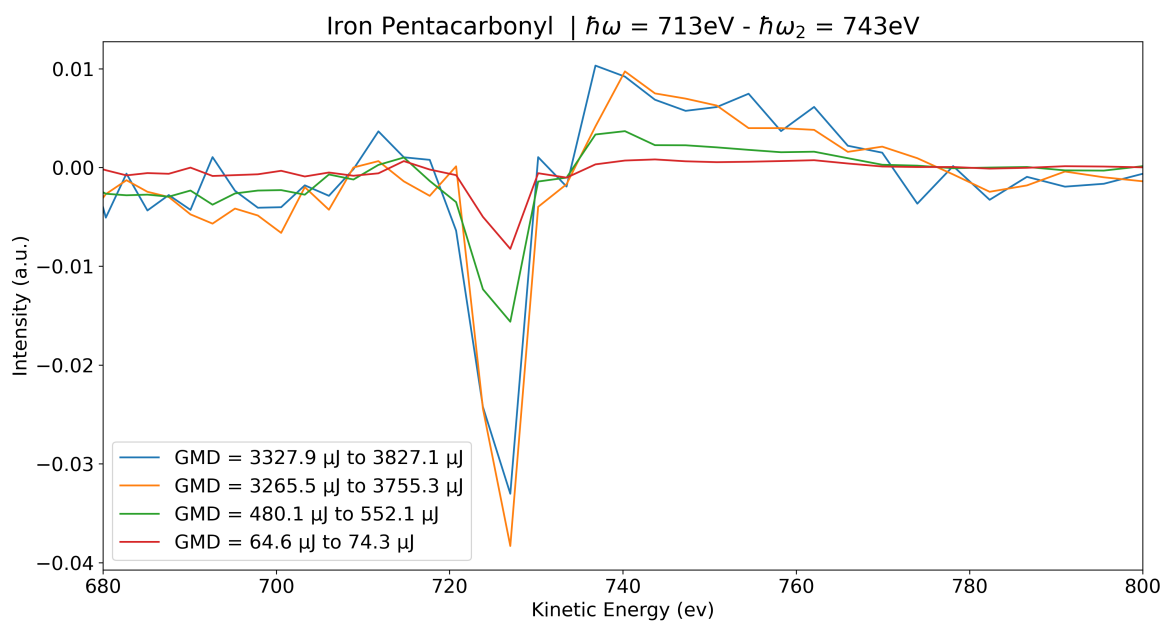
Figure 46: A comparison between the SCH resonant electron spectrum at 713 eV and the DCH resonant spectrum at 743 eV at different pulse energies for both samples in the $L_{23}M_{45}M_{45}$ kinetic energy region between 680 eV and 800 eV.
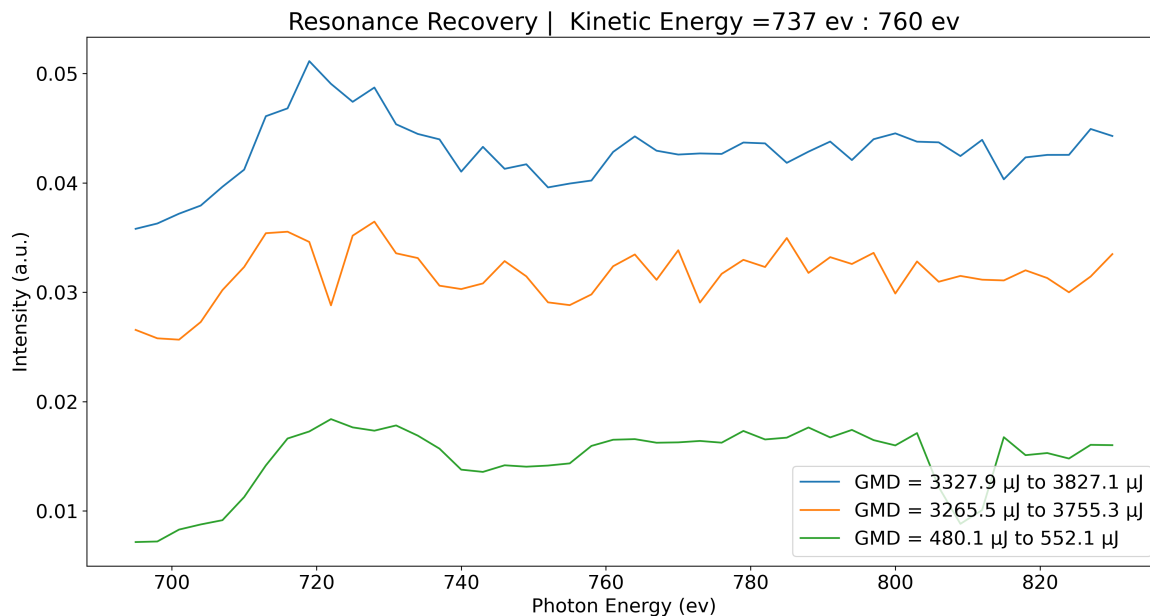
(a) Sample Fe(CO)$_5$
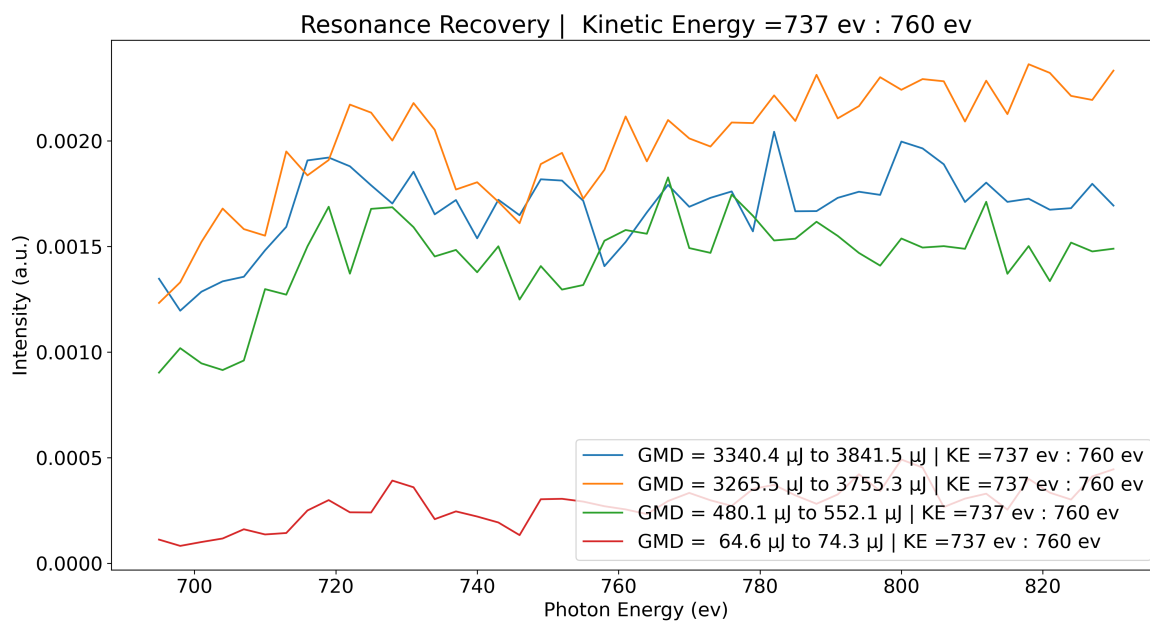
(b) Sample Fe(C$_5$H$_5$)$_2$

Figure 47: Comparing the integrated signal difference between higher pulse energy measurements and the lowest pulse energy measurement in iron pentacarbonyl and ferrocene. The subtracted signal stems from measurements with SQS GMD range of approximately $60\,\mu J$ to $70\,\mu J$. This comparison is performed in the kinetic energy range of the established DCH $L_{23}M_{45}M_{45}$ region from $737\,eV$ to $760\,eV$. In FIG. 47a, the two highest pulse energy measurements are divided by a factor of 2 in order to increase visibility.

the resulting yields of the lowest pulse energy measurements for each photon energy step are subtracted from each of the higher pulse energy measurements, respectively. In doing so, changes in the XAS spectrum depending on increasing pulse energy are revealed.

In FIG. 47a, a rising edge with onset around 758 eV is resolved for the two highest pulse energy measurements. In these two measurements, an additional resonance feature can be resolved that is neither associated with the roughly resolved resonance displayed in the region between 709 eV and 737 eV, nor the rising edge. This feature has an onset at approximately 740 eV and an almost 20 eV width.

Comparing FIG. 47a to FIG. 5 allows for the assignment of underlying processes to the recovered resonance features. The broadest feature at the lower end of the photon-energy region, for example, can be assigned to the iron center $2p$ SCH resonances. The measurement with pulse energy upper limit at approximately 3760 μJ even resolves the two-feature nature of this resonance rather well. The rising edge can be consequently assigned to the convolution of the SCH ionization edge and the DCH ionization edge. The middling feature falls neatly into the region of the $2p^2$ DCH resonance features. Recovering the $2p^2$ DCH resonance in this matter further credits the assignments based on FIG. 46a.

In FIG. 47b, the rising edge identified in iron pentacarbonyl can be matched with a similar onset around 758 eV. This edge is resolved for the three highest pulse energy measurements. In these three measurements, the additional resonance feature neither associated with the SCH resonances, nor the rising edge, is only partially resolved. In the ferrocene results, this feature has a matching onset at approximately 740 eV and an almost 20 eV width, similar to the results for iron pentacarbonyl.

Feature assignment for these recovered resonances is the same as for the corresponding measurement in iron pentacarbonyl. The broadest feature at the lower end of the photon-energy region can be assigned to the iron center $2p$ SCH resonances. The two-peak nature of this feature is only resolved in the measurement with pulse energy upper limit of 3760 μJ. The rising edge can be consequently assigned to the convolution of the SCH ionization edge and the DCH ionization edge. The feature in the photon energy range between 740 eV and 760 eV can be assigned to the $2p^2$ DCH resonance features in relative good agreement with the isolated iron model results shown in FIG. 5. Recovering the $2p^2$ DCH resonance in this matter further credits the assignments based on FIG. 46b.

Despite the carefully selected kinetic energy region that was used for FIG. 47 and was reasoned to be mostly free of SCH Auger-Meitner- or direct photoionization electron signal based on the results of Section 7 and FIG. 46, a significant dependence on the SCH resonance is revealed for summed signal and corresponding photon energies. This could suggest an SCH-responsive background for the kinetic energy region 737 eV to 760 eV.

FIG. 48 exemplifies this character of the results further by comparing the sum of the signal detected in the kinetic energy region 737 eV to 760 eV, the region associated with the DCH $L_{23}M_{45}M_{45}$ response between a photon energy region with no signal and the exemplary photon energy on resonance, that was used in previous treatment of this region. This comparison is carried out for the various pulse energies. The figure shows the dependence of signal to pulse energy, which is best approximated by adding a quadratic term to the approximation of the remaining linear background. In this, the quadratic dependency of signal intensity on pulse energy is recovered for this signal.
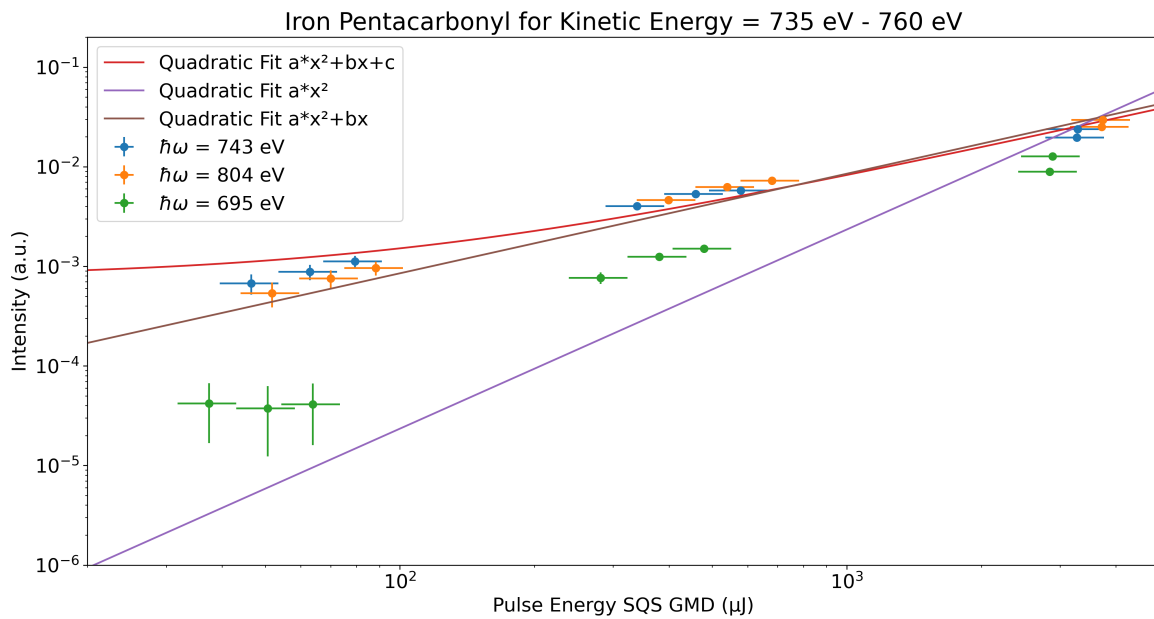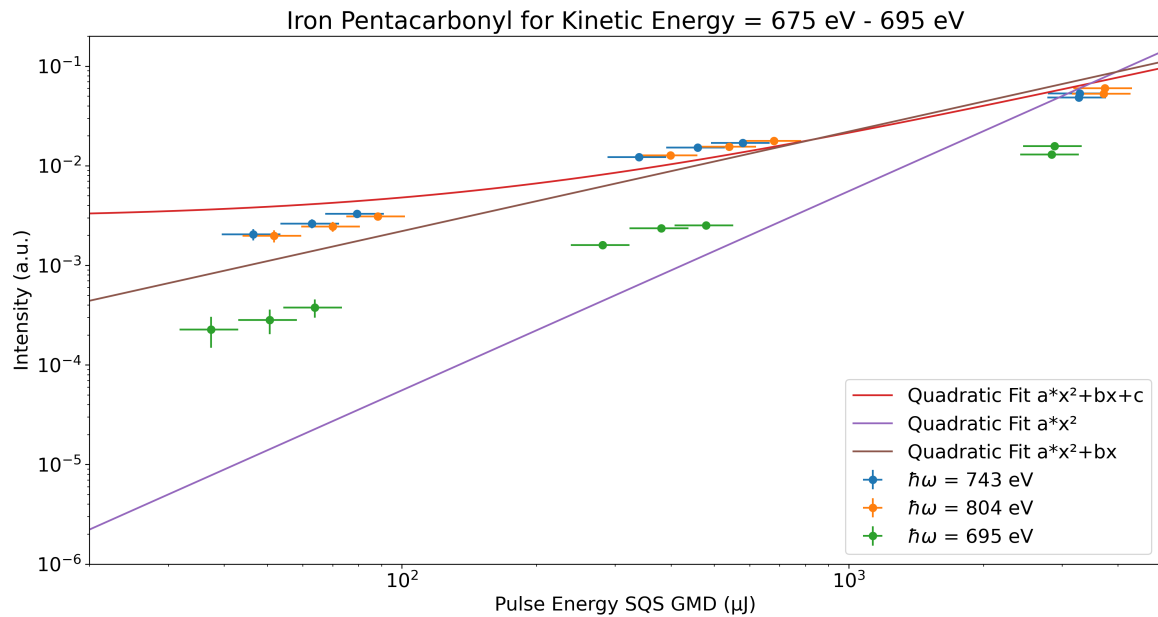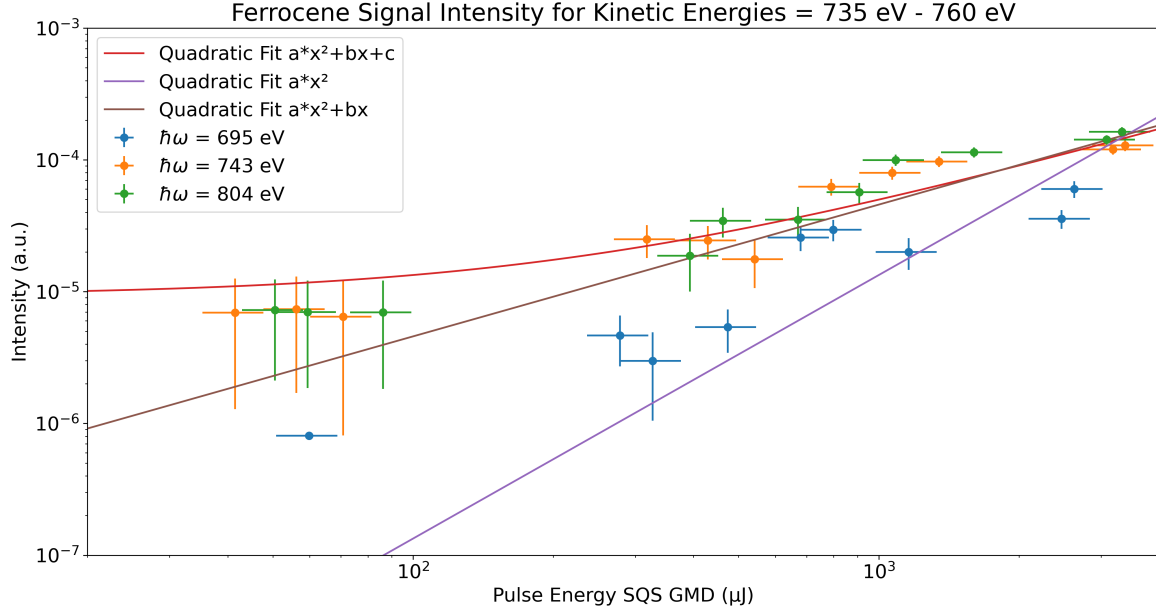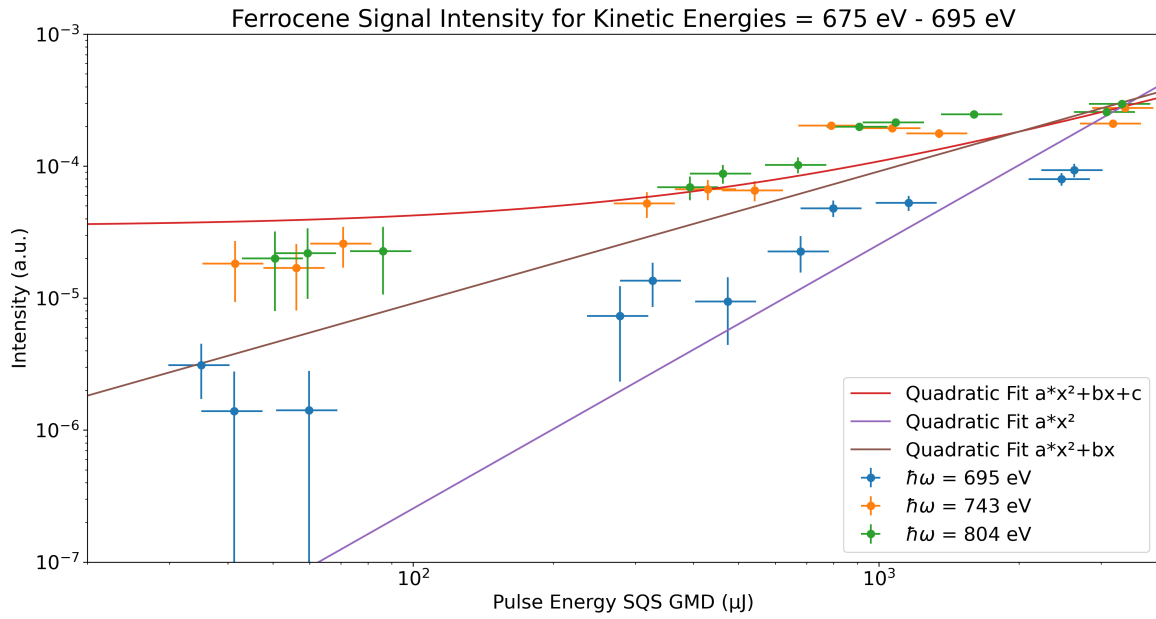
Figure 48: The Auger-Meitner electron signal intensities for the kinetic energy region of interest for possible $2p^2$ resonances in the kinetic energy range of $737\,\text{eV}$ to $760\,\text{eV}$ at the photon energies $695\,\text{eV}$, $743\,\text{eV}$ and $804\,\text{eV}$ and for the different pulse energy measurements in iron pentacarbonyl outlined in Section 7. Fits of the form $y = ax^2 + bx + c$, $y = ax^2 + bx$ and $y = ax^2$ to the $743\,\text{eV}$ measurement are shown. It can be seen that a linear addition to the quadratic term describes the data best.

Figure 49: The Auger-Meitner electron signal intensities for the kinetic energy region of interest for possible $2p^2$ resonances in the kinetic energy range of 675 eV to 695 eV at the photon energies 695 eV, 743 eV and 804 eV and for the different pulse energy measurements in iron pentacarbonyl outlined in Section 7. Fits of the form $y = ax^2 + bx + c$, $y = ax^2 + bx$ and $y = ax^2$ to the 743 eV measurement are shown. It can be seen that a linear addition to the quadratic term describes the data much better than a purely quadratic function.

Figure 50: The Auger-Meitner electron signal intensities for the two kinetic energy regions of interest for possible $2p^2$ resonances in the kinetic energy range of 735 eV to 760 eV at the photon energies 695 eV, 743 eV and 804 eV and for the different pulse energy measurements in $Fe(C_5H_5)_2$ outlined in Section 7. Fits of the form $y = ax^2 + bx + c$, $y = ax^2 + bx$ and $y = ax^2$ to the 743 eV measurement are shown. Uncertainties for measurements at the lower end of the pulse energy scale incorporate a larger uncertainty.

Attempting a similar method to recover the quadratic increase in signal intensity of the $L_{23}M_{23}M_{45}$ region that was predicted to out-scale the SCH contribution in this area in FIG. 7 does not yield a similar result. FIG. 49 shows the linear relationship between signal intensity and pulse energy for the kinetic energy region. This implies that the expected out-scaling does not take effect strongly enough to separate the DCH signal from the SCH contributions. The results show that the SCH signal in this region and the associated linear relationship with pulse energy dominate the kinetic energy region. The source of the occupying SCH signal is not revealed in FIG. 7, but FIG. 6 suggests the relevant kinetic energy region to be occupied with SCH Auger-Meitner electron signal stemming from a photon-matter interaction with iron cations as target, specifically singly to triply charged iron cations. This negative result for DCH electron signal enforces, however, the results for the $L_{23}M_{45}M_{45}$ region by providing a suitable counterexample. It also calls for a more refined approach to reveal the DCH contributions in the $L_{23}M_{23}M_{45}$- and $L_{23}M_{23}M_{23}$ region.

Recovering the quadratic relationship between signal intensity and pulse energy is also possible for ferrocene. FIG. 50 exemplifies the results on this sample further by comparing the sum of the signal detected in the kinetic energy region 737 eV to 760 eV, the region associated with the DCH $L_{23}M_{45}M_{45}$ response, for a photon energy region with no signal to the same sum of the signal for the exemplary photon energy on resonance, 743 eV, which was used in

Figure 51: The Auger-Meitner electron signal intensities for the two kinetic energy regions of interest for possible $2p^2$ resonances in the kinetic energy range of 675 eV to 695 eV at the photon energies 695 eV, 743 eV and 804 eV and for the different pulse energy measurements in $Fe(C_5H_5)_2$ outlined in Section 7. Fits of the form $y = ax^2 + bx + c$, $y = ax^2 + bx$ and $y = ax^2$ to the 743 eV measurement are shown. Similar to previous measurements, the isolated $y = ax^2$ term does not describe the data well.

previous treatment of this region. This comparison is carried out for the various pulse energies that were measured in this sample. The figure shows the increase in signal due to the resonant feature and increase in pulse energy is best approximated by adding a quadratic term to the approximation of the linear background, as was established before for the iron pentacarbonyl sample. In this, the quadratic dependency of signal intensity on pulse energy is recovered for this signal. It is worth to note that the quadratic relationship in the two samples follows a rather similar scaling.

When comparing the different pulse energy regions that were accounted for in FIG. 48 and FIG. 50, the data points at the high end of the pulse energy scale seem to deviate stronger from the quadratic fit for both samples. This is likely due to a saturation of accessible $L_{23}M_{45}M_{45}$ transitions within the Fe centers of the sample. In particular, a DCH Auger-Meitner electron in the $L_{23}M_{45}M_{45}$ region cannot occur when the corresponding M-shell energy levels have been depleted of electrons. With higher pulse energy, according to Eq. 3, more sequential ionizations of the Fe center and more DCH processes occur in both samples. Additionally, in Section 6, the increased occurrence of super-Coster-Kronig transitions in the M-shell energy level as a response to DCH excitation in the sample was discussed. Together, this can entail a depletion of the $3d$ subshell which results in a loss of signal from the $L_{23}M_{45}M_{45}$ region within the pulse energy scale of the measurements in both samples. In the measured spectra, this effect would lead to saturated intensity of $L_{23}M_{45}M_{45}$ Auger-Meitner electrons, similar to what is observed for FIG. 48 and FIG. 50.

8.3 Double Core-Hole Electron Spectroscopy of the $L_{23}M_{23}M_{45}$ Auger-Meitner Lines for Ferrocene and Iron Pentacarbonyl

In a next step, attempting a similar method to illustrate the quadratic increase in signal intensity of the $L_{23}M_{23}M_{45}$ region that was predicted to out-scale the SCH contribution in this area in FIG. 7 yields a similar negative result as the same attempt for iron pentacarbonyl. FIG. 51 shows the linear relationship between signal intensity and pulse energy for the kinetic energy region in question. This implies that the expected out-scaling does not take effect strongly enough to separate the DCH signal from the SCH contributions. The results show that the SCH signal in this region and the associated linear relationship with pulse energy dominates the kinetic energy region. These are virtually the same results as for iron pentacarbonyl and the source of the occupying signal seems to be the same: Singly to triply charged iron cations account for most of the SCH Auger-Meitner electron signal in this kinetic energy region. In a roundabout way, these findings reinforce the results for the unencumbered $L_{23}M_{45}M_{45}$ region by providing a suitable counterexample of a region too encumbered with SCH in which a linear relationship prevails, despite DCH signal being present. However, it also reaffirms calls for a more refined approach to reveal the DCH contributions in the $L_{23}M_{23}M_{45}$ and $L_{23}M_{23}M_{23}$ region for both samples.

The previous attempts at recovering the non-linear signal intensity relationship with the rising pulse energy for the $L_{23}M_{23}M_{45}$, outlined in FIG. 49 and FIG. 51, suggest that the SCH contribution to this electron kinetic energy region is much stronger than was previously assumed on the basis of FIG. 7. A contributing factor that is not incorporated in FIG. 7

is the contribution from SCH Auger-Meitner electrons from multiply ionized iron cations. Incorporating this contribution into a renewed evaluation of the electron spectrum assumes these ions to be present and available as targets within the duration of the ionizing pulse length, as was shown in Section 6. In order to gain an accurate sense of the distribution of Auger-Meitner electrons at the exemplary photon energy 743 eV in the $L_{23}M_{23}M_{45}$ region, the ion spectrum at the closest accessible photon energy can be used. This photon energy, due to the 3.5 eV step width of the iToF spectroscopy measurements and the bandwidth of the experiment, is 744 eV. As the molecular makeup of the two samples was shown to influence the product cation ratios and thereby, for the sake of this approximation, offers different Auger-Meitner electron source ratios for each sample, this procedure is carried out for both samples individually.

FIG. 52 shows the spectra that were used as a reference for the approximation of the possible sources of Auger-Meitner electrons in the target interaction zone. Both FIG. 52a and FIG. 52b contain mass-over-charge ratios that are host to multiple different cation species, particularly CO^+, O^{2+}, C^{3+} and O^{4+}. Where they cannot be differentiated, surrounding cation peak heights were used as a rough estimate of the cation contribution to the spectrum. From these considerations, and the results of the calculations displayed in FIG. 6, an approximation of the SCH Auger-Meitner electron spectra can be constructed that highlights the contributions of the iron cation species' contributions. This SCH contribution can be used to identify regions on the kinetic energy scale that are not associated with the SCH contributions of iron cations.
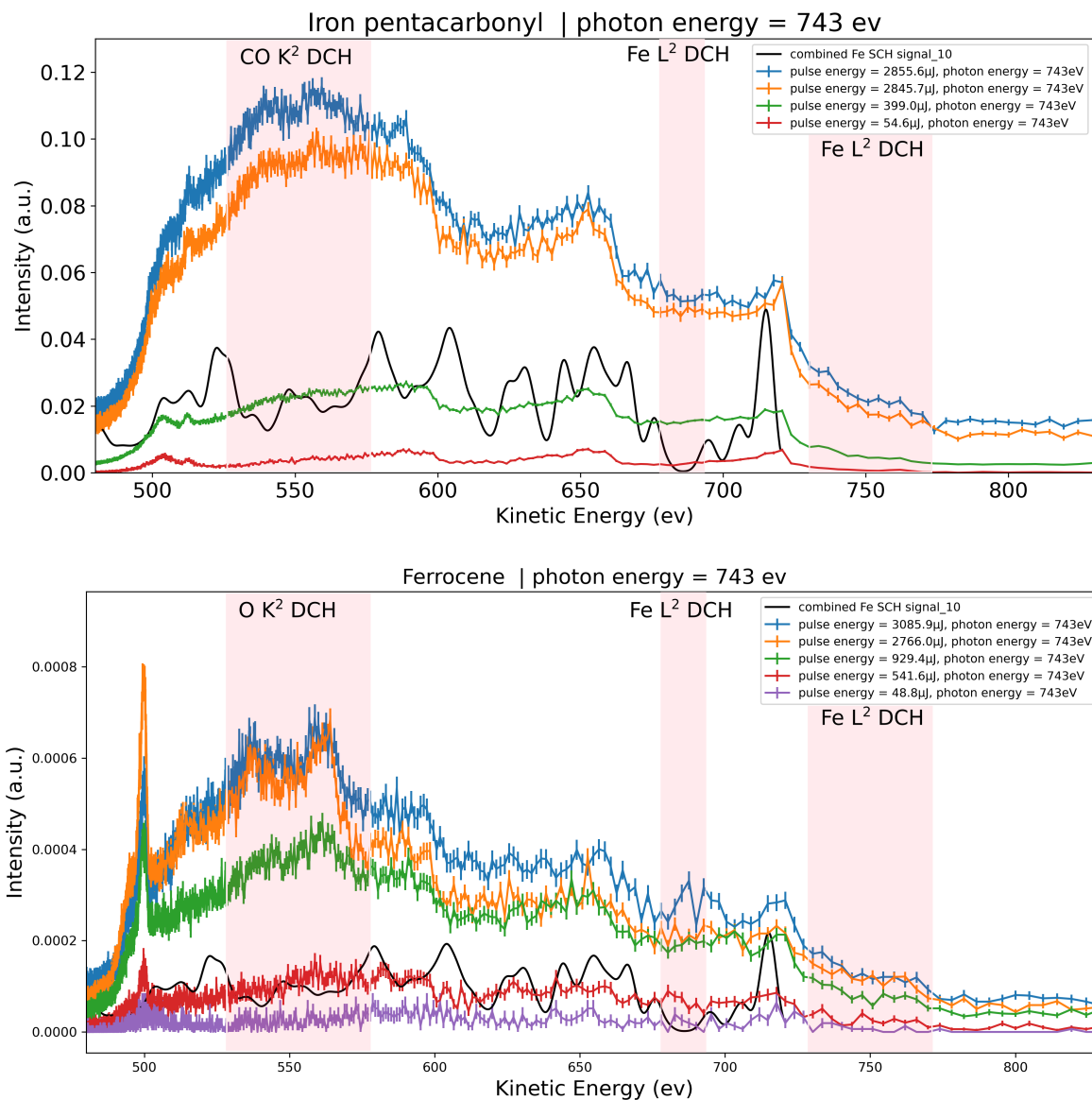
FIG. 53 shows the measured iron pentacarbonyl Auger-Meitner electron signal intensities for the photon energy 743 eV at various pulse energies compared to the approximate SCH Auger-Meitner electron contribution of iron cations, singly and multiply charged. This contribution approximation includes scaled Auger-Meitner electron spectra of isolated iron cations from Fe^+ to Fe^{13+}.

The figure again illustrates the issue of separating the DCH from SCH contribution in the $L_{23}M_{23}M_{45}$ region. The contribution approximation features conform to the recognizable features in the low- as well as high-intensity spectra of the measured Auger-Meitner electron spectra. The figure displays well the cause of the failure to identify the DCH Auger-Meitner electron contributions in the $L_{23}M_{23}M_{45}$ region of the kinetic energy scale, but also the $L_{23}M_{23}M_{23}$ region. Both are host to a number of SCH Auger-Meitner electron features. The only kinetic energy region that appears unencumbered according to FIG. 53 is the region between 680 eV and 690 eV.

FIG. 53 shows the measured ferrocene Auger-Meitner electron signal intensities for the photon energy 743 eV, at similar pulse energies as the iron pentacarbonyl measurements. The signal is compared to the approximate SCH Auger-Meitner electron contribution of iron cations, singly and multiply charged, as determined by FIG. 52. This contribution approximation includes scaled Auger-Meitner electron spectra of isolated iron cations from Fe^+ to Fe^{13+}.

The figure illustrates the issue of separating the DCH from SCH contribution in the $L_{23}M_{23}M_{45}$ region for the ferrocene measurements. The contribution approximation features conform to the recognizable features in the low- as well as high-intensity spectra of the measured ferrocene Auger-Meitner electron spectra. The figure displays well the cause of the initial failure to identify the DCH Auger-Meitner electron contributions in the ferrocene $L_{23}M_{23}M_{45}$ re-
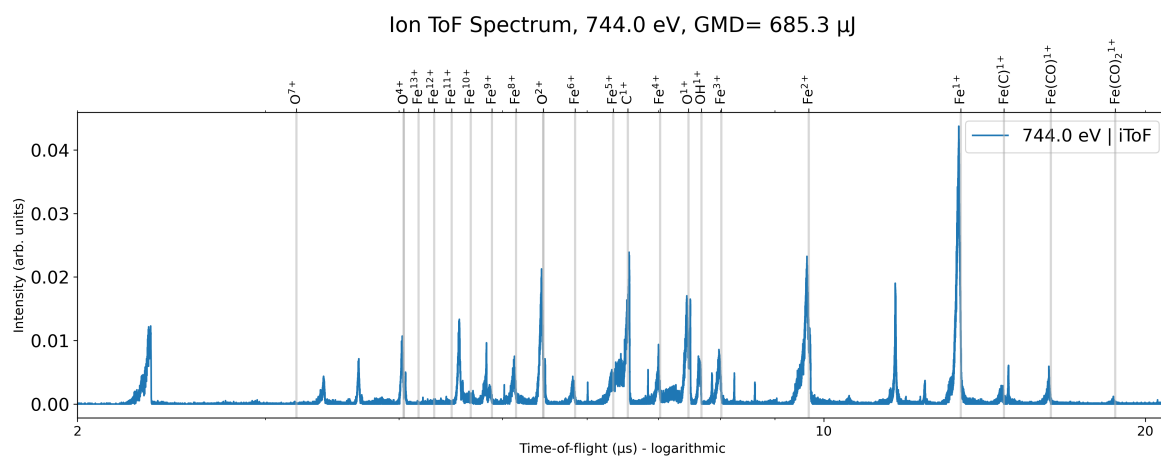
(a) Sample $Fe(CO)_5$: The ion spectrum of $Fe(CO)_5$ at the photon energy $744\,eV$ with an SQS GMD peak pulse energy of approximately $690\,\mu J$.
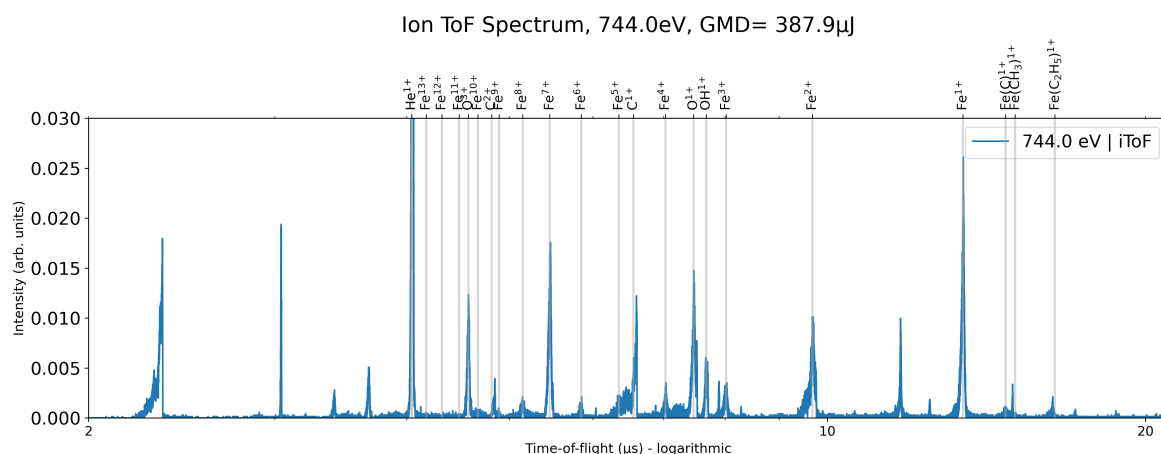
(b) Sample $Fe(C_5H_5)_2$: The ion spectrum of $Fe(C_5H_5)_2$ at the photon energy $744\,eV$ with an SQS GMD peak pulse energy of approximately $390\,\mu J$.

Figure 52: The ion spectra of both samples at the photon energy $744\,eV$, chosen for a low pulse energy measurement. The approximate ratios of iron cations not overlapping with other product fragment cations can be used to approximate the target makeup during irradiation. The relevant mass-over-charge ratios for the iron cation charge states have been identified on the logarithmic time-of-flight scale.

Figure 53: The measured iron pentacarbonyl and ferrocene Auger-Meitner electron signal intensities for the photon energy 743 eV at various pulse energies compared to the approximate SCH Auger-Meitner electron contribution of iron cations, singly and multiply charged, scaled by their contribution to the ion spectra at high pulse energy measurements. While most of the $L_{23}M_{23}M_{45}$ is occupied, the kinetic energy region 680 eV to 690 eV appears somewhat less encumbered.
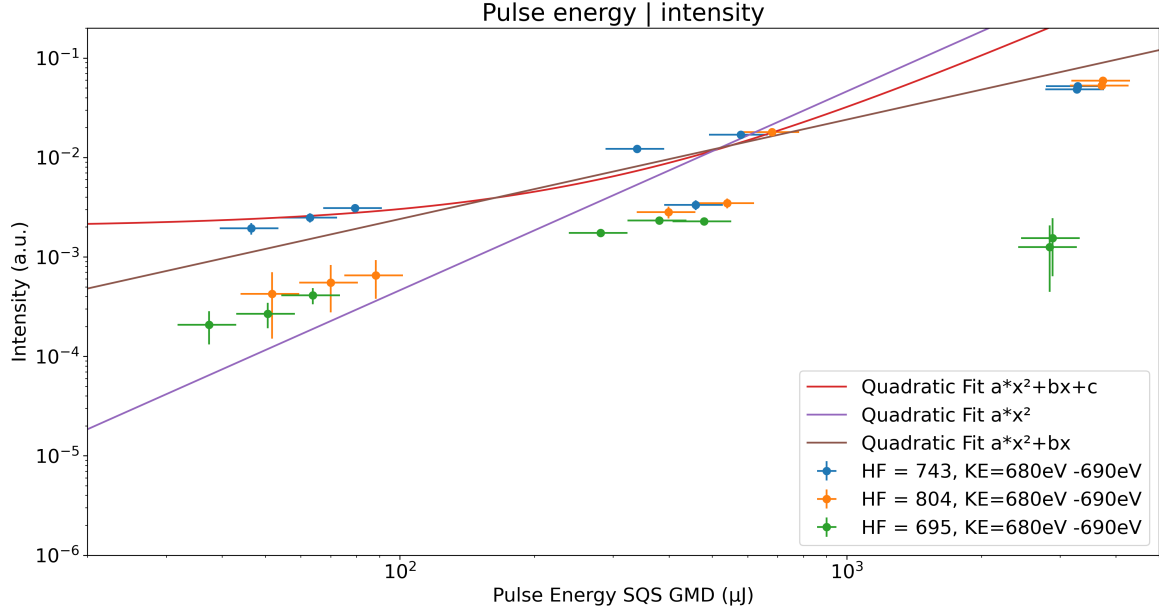
Figure 54: The Auger-Meitner electron signal intensities for the kinetic energy region of interest for possible $2p^2$ resonances in the kinetic energy range of 680 eV to 690 eV at the photon energies 743 eV and 804 eV and for the different pulse energy measurements in iron pentacarbonyl outlined in Section 7. Both linear fit and quadratic fit are shown as a guide to the eye.

gion of the kinetic energy scale, but also the $L_{23}M_{23}M_{23}$ region of the same measurements. Both are host to a number of SCH Auger-Meitner electron features, just as was observed for iron pentacarbonyl. The only kinetic energy region that appears unencumbered according to FIG. 53 is the region between 680 eV and 690 eV. This also matches the observations for iron pentacarbonyl, but FIG. 53 additionally shows that the global minimum of SCH contribution between 680 eV and 690 eV coincides with a small increase in signal across all pulse energy measurements.

The kinetic energy region that was found as the most likely to reveal the DCH contributions for the $L_{23}M_{23}M_{45}$ region was already covered in its entirety by figures FIG. 49 and FIG. 51, without offering conclusive evidence for the detection of DCH Auger-Meitner electrons.

FIG. 54 shows the results of restricting a pulse intensity to signal comparison to the kinetic energy region 680 eV to 690 eV outlined in FIG. 53. This representation does not alter the evidence or conclusions of FIG. 49 in a meaningful way. It shows, however, the differences between low- and high-pulse energy measurements in this experiment, as the electron signal increases less per step for higher pulse energy measurements than for low pulse energy measurements. These observations apply to both photon energy regions.

FIG. 55 shows the results of restricting a pulse intensity to signal comparison to the kinetic energy region 680 eV to 690 eV outlined in FIG. 53 for the ferrocene sample. This representation alters the conclusions drawn from FIG. 51 in a meaningful way, as it was observed for FIG. 51 that low pulse energy measurements conform less to the linear trend that was ascribed
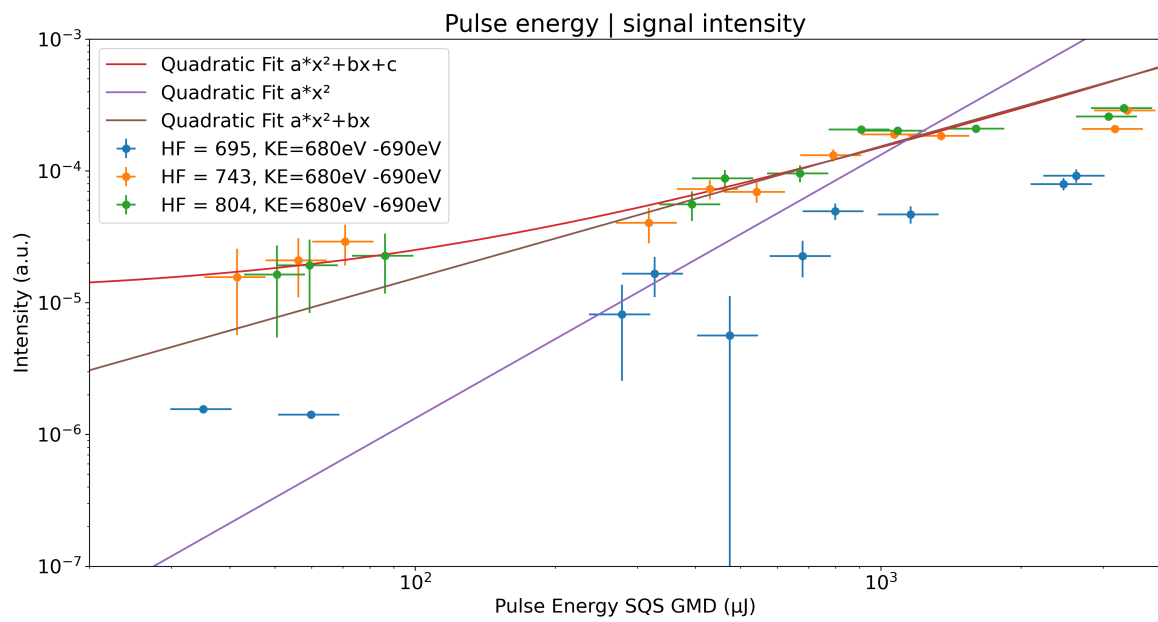
Figure 55: The Auger-Meitner electron signal intensities for the two kinetic energy regions of interest for possible $2p^2$ resonances in the kinetic energy range of $680\,\text{eV}$ to $690\,\text{eV}$. at the photon energies at the photon energies $743\,\text{eV}$ and $804\,\text{eV}$ and for the different pulse energy measurements in $\text{Fe}(\text{C}_5\text{H}_5)_2$ outlined in Section 6. Both linear fit and quadratic fit are shown as a guide to the eye.

to high pulse energy measurement data points. FIG. 55 shows that for both photon energies 743 eV, exemplifying the found DCH resonance, as well as for 804 eV, the pulse energy measurements between $100\,\mu J$ and $2000\,\mu J$ show a quadratic rise in signal with increasing pulse energy.

For this kinetic energy region, high pulse energy measurements above the $1\,mJ$ mark fell below the expected signal intensity values for pure quadratic signal dependency on irridiance for both iron pentacarbonyl as well as ferrocene. This deviation appears more significant than the one observed for the $L_{23}M_{45}M_{45}$ region. Depletion of the M_{45} electrons cannot account for this decrease in measured signal intensity in the $L_{23}M_{23}M_{45}$ region compared to the expected values.

Ultimately, limiting the kinetic energy region based on FIG. 53 led to a quadratic rise in signal intensity for much, if not all of the investigated pulse energy regions. The restriction of the kinetic energy region to $680\,eV$ to $690\,eV$ to illustrate a quadratic signal intensity to pulse energy relation hints at the accuracy of the collective SCH Auger-Meitner electron signal from multiply charged iron cations to be within a $10\,eV$ range and thereby comparable to the bandwidth ($7.4\,eV$ and $8.0\,eV$, respectively) of the experiment at these photon energy regions.

8.4 Quadratic Coefficient Mapping for Iron Pentacarbonyl and Ferrocene

The quadratic fitting of the rise in electron signal intensity with the increase in peak pulse energy, which was previously discussed in Section. 8.1, Section. 8.3 and Section. 8.2, can be used to illustrate the various regions of interest identified in the analysis of this photon energy range and kinetic energy region. By re-binning the kinetic energy region over the index k in steps of 5 eV and applying a quadratic fit $y_{p,k} = a_{p,k}x^2 + b_{p,k}x + c_{p,k}$ over the available pulse energy range for each kinetic energy bin k and each photon energy step p, the collected eToF data can be investigated. Using this technique for all measured photon energies, resolution of previously inaccessible DCH Auger-Meitner electron signal can be achieved. The resulting maps for the linear coefficient $b_{p,k}$ and the static coefficient $c_{p,k}$ are shown in Section 10, but the focus here will be on the quadratic coefficient $a_{p,k}$.

To establish non-linearity within the bounds of the 5 eV kinetic energy bins, a coefficient map of the quadratic coefficient $a_{p,k}$ in the collection of $y_{p,k} = a_{p,k}x^2 + b_{p,k}x + c_{p,k}$ fits reveals the photon energies and the kinetic energy regions in which the electron signal intensity shows particularly strong quadratic coefficients. Such a quadratic coefficient map was created by multiplying the coefficient with the signal intensity for each bin for the iron pentacarbonyl sample and the ferrocene sample.

FIG. 56 shows the coefficient map for the sample iron pentacarbonyl. All regions of Auger-Meitner electron signal associated with iron DCH excitations can be identified in this coefficient map by the strength of the quadratic contribution to the fit. Overall the quadratic contribution as measured by the coefficient $a_{p,k}$ increases from $L_{23}M_{23}M_{23}$ to $L_{23}M_{23}M_{45}$ and $L_{23}M_{45}M_{45}$, with the contribution being several orders of magnitude weaker in $L_{23}M_{23}M_{23}$ than in $L_{23}M_{45}M_{45}$. This observation can be made for both the resonant excitation photon energy region, as well as the direct ionization photon energy region, respectively.
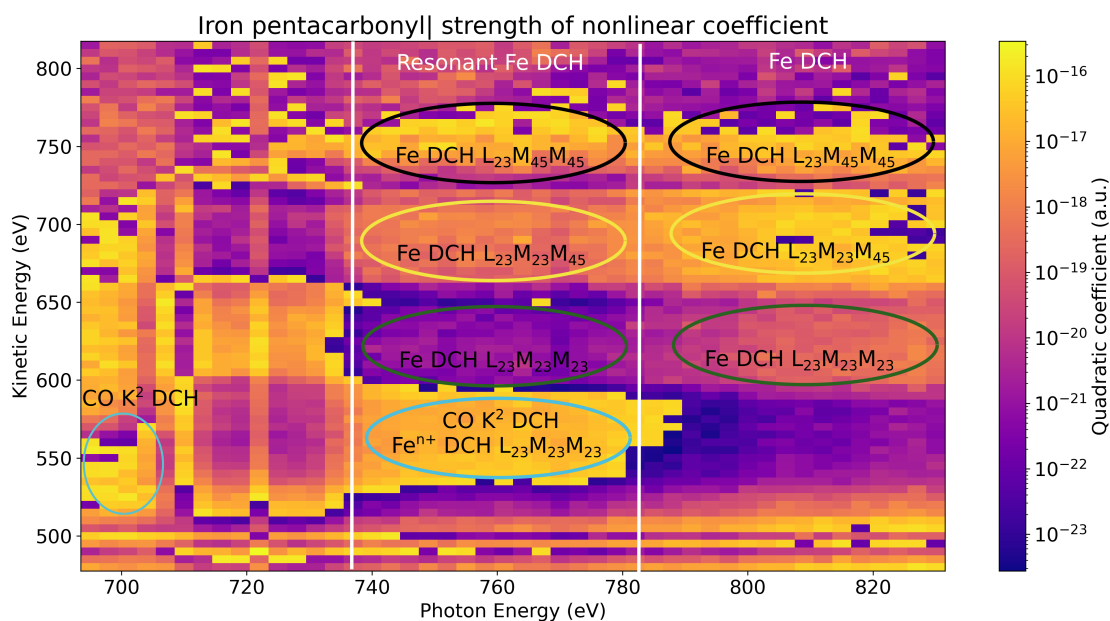
Figure 56: A coefficient map of the quadratic coefficient $a_{p,k}$ in the collection of $y_{p,k} = a_{p,k}x^2 + b_{p,k}x + c_{p,k}$ reduced chi square fits for the iron pentacarbonyl sample, conducted for the photon energy range (index p) of 695 eV to 830 eV in steps of 3.5 eV and the kinetic energy region (index k) of 480 eV to 820 eV in bins of 5 eV. The previously identified kinetic energy regions and photon energy regions associated with DCH processes in iron and oxygen have been outlined and labeled. Indicators for estimated photon energy limits between SCH, resonant DCH and direct DCH processes have been included in white.

The $L_{23}M_{23}M_{23}$ region (marked in green) is weakest in strength of $a_{p,k}$ coefficient for both resonant, as well as direct excitation. It is notable that $a_{p,k}$ increases over the course of the direct excitation energy region towards stronger quadratic contributions with higher photon energies. The $L_{23}M_{23}M_{45}$ Auger-Meitner region shows a much stronger quadratic coefficient, with the coefficient $a_{p,k}$ of the resonant excitation region on the same order of magnitude as the strongest quadratic contribution of the $L_{23}M_{23}M_{23}$ region. The $L_{23}M_{23}M_{45}$ Auger-Meitner region also displays a rise of quadratic contribution strength with increasing photon energy in the direct ionization regime, albeit several orders of magnitude stronger overall than what was observed for the $L_{23}M_{23}M_{23}$ region. This direct ionization region shows the strongest $a_{p,k}$ contribution of this specific Auger-Meitner region. The $L_{23}M_{45}M_{45}$ region does not show such a trend. Both resonant DCH excitation photon energy region, as well as DCH ionization photon energy region, show comparable quadratic coefficient strength, on the order of 10^{-16}, the largest coefficients measured.

There are other regions of high quadratic contribution found in this map. The quadratic contribution to the fit in the photon energy region pre iron resonance at 695 eV to 710 eV shows a strong quadratic contribution that identifies the CO K^2 direct ionization DCH process. This region overlaps at higher photon energies with the expected resonant DCH Auger-Meitner electron signal of multiply charged iron cations in the interaction region. This combination creates a region of very strong quadratic contribution coefficients $a_{p,k}$. As it is impossible to disentangle the two contributions further based on the currently available data, no estimate for the respective contributions of both processes can be given here. It should be noted, however, that the photon energy region associated with the direct DCH ionization of multiply charged iron cations hosts some of the lowest quadratic contributions.

Overall, the excellent signal-to-noise ratio of the iron pentacarbonyl measurement resulted in easily identifiable regions of DCH signal, outlined in the large differences in order of magnitude of the associated quadratic coefficient. From this coefficient map, a reconstruction of the DCH absorption of the molecule and a reconstruction of the associated DCH electron signal can be created.

FIG. 57 shows such a reconstruction of the measured iron pentacarbonyl absorption, including DCH absorption. For the four kinetic energy regions in which iron Auger-Meitner electron signal of DCH relaxation processes is expected, corresponding absorption coefficients are recovered, with the region of 625 eV showing the weakest resonance, but a rising direct DCH ionization. This rise in absorption in the photon energy region associated with direct DCH ionization is matched by the kinetic energy region of 680 eV. Here, the DCH resonance can be reconstruccted as well, though it is outscaled by the direct DCH absorption. In the kinetic energy region of 750 eV, both direct, as well as resonant DCH absorption, can be reconstructed, but are dominant enough to make a clear separation between the two difficult. Lastly, the kinetic energy region of 560 eV, which was associated with both CO DCH processes, as well as potential DCH Auger-Meitner electrons of multiply charged iron cations shows a strong resonance, confirming the influence of these cations in the composite signal.

FIG. 58 shows the reconstruction of an electron spectrum (in red) in the kinetic energy region from 480 eV to 850 eV for the photon energy 743 eV. The kinetic energy shift of the three distinctive regions identified in FIG. 56 with respect to the total expected Fe SCH signal can be seen in this depiction. Remarkable agreement exists in form and relative intensity between
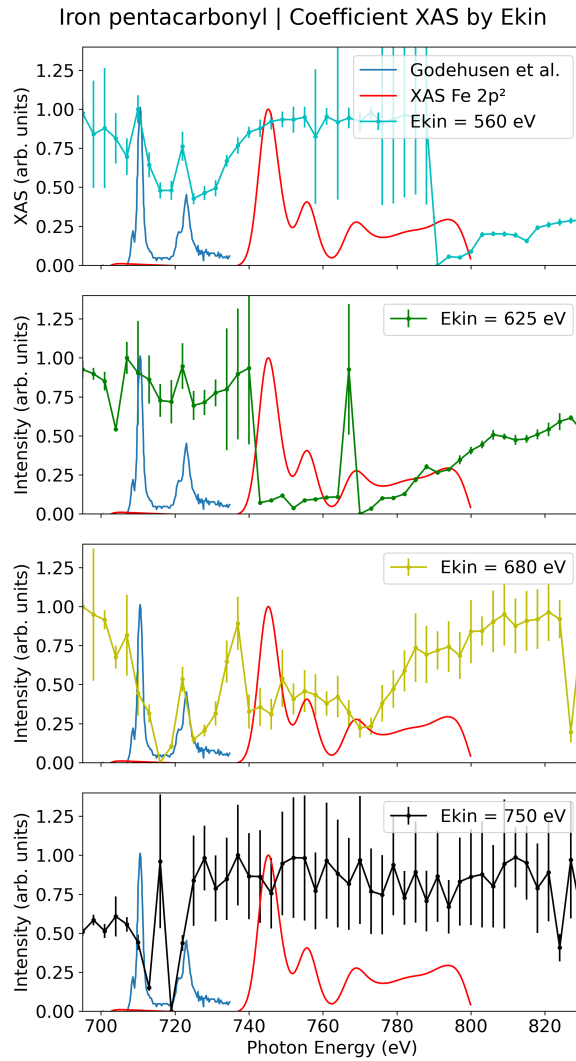
Figure 57: A reconstruction of the absorption in iron pentacarbonbyl for the photon energy range (index p) of 695 eV to 830 eV, including DCH absorption. The results are binned over adjacent kinetic energy bins, with errorbars depicting the associated standard deviation. Colors match the corresponding regions in FIG. 56 for better identification. The results of Gedhusen et al. [32] and the expected resonant DCH absorption cross-sections for the isolated iron atom are also depicted. Resonant DCH is much stronger and matching the expected photon energies for kinetic energy regions (680 eV and 750 eV), in which the electron orbital, into which the resonant excitation occurs, is a participator in the subsequent Auger-Meitner relaxation. The kinetic energy region 560 eV shows a strong match for the isolated iron DCH absorption cross-section, which hints at DCH Auger-Meitner electrons of multiply charged iron cations being detected.
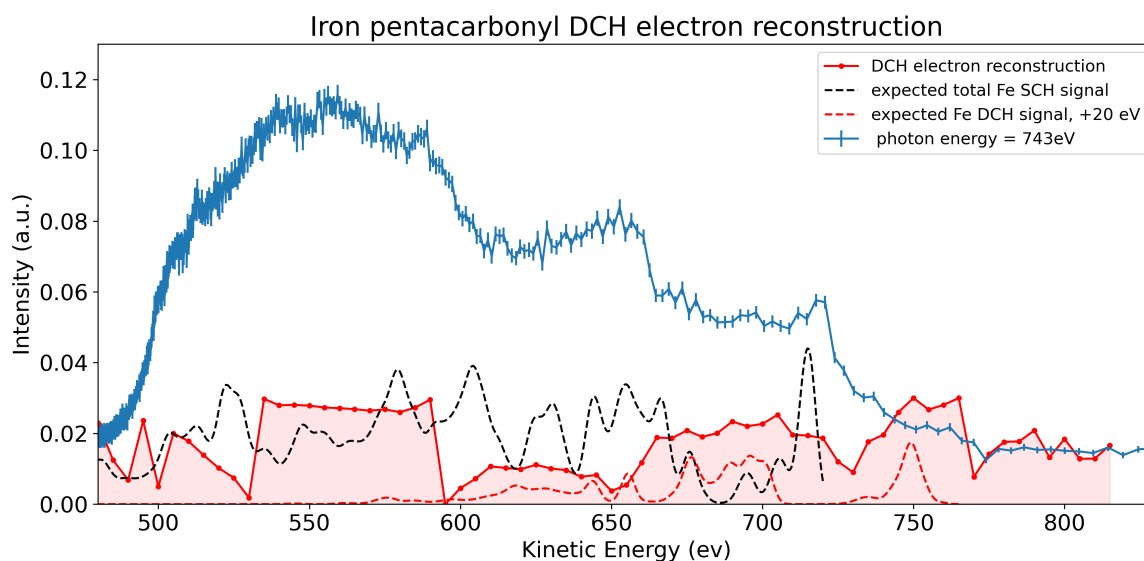
Figure 58: A reconstruction of the DCH Auger-Meitner electron spectrum from FIG. 56 in the kinetic energy region (index k) from 480 eV to 850 eV, compared to the detected electron spectrum at a photon energy (index p) of 743 eV, the expected total Fe SCH signal and the expected Fe DCH signal, shifted to 20 eV higher energies. There is remarkable agreement between the form of the expected DCH spectrum and the reconstructed DCH spectrum. The observed shift in kinetic energies between expected kinetic energies and measured ones can be attributed to the molecular environment of the sample.
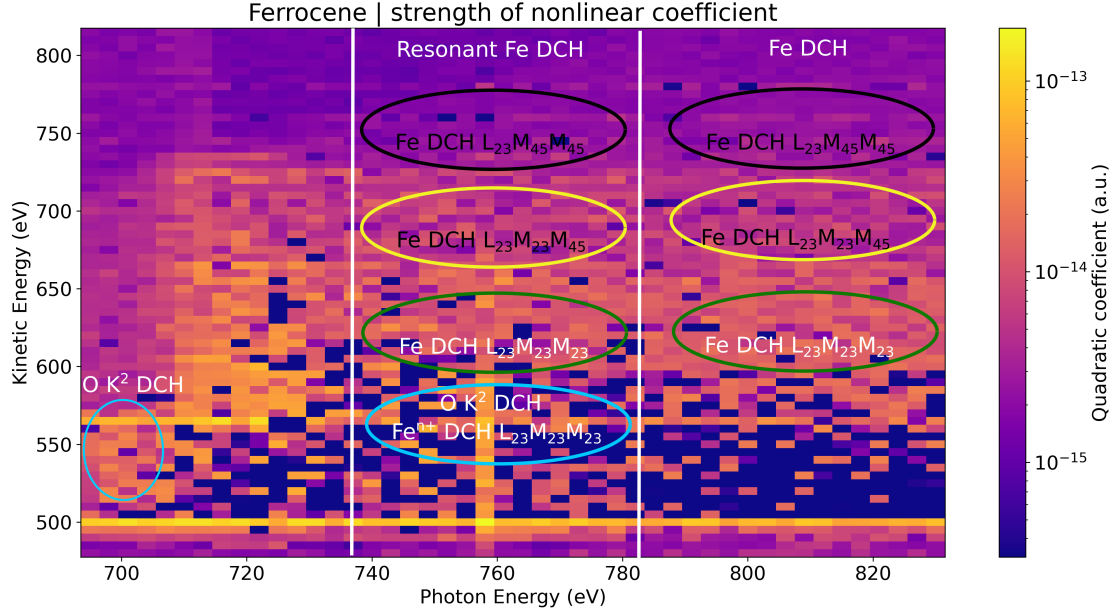
Figure 59: A coefficient map of the quadratic coefficient $a_{p,k}$ in the collection of $y_{p,k} = a_{p,k}x^2 + b_{p,k}x + c_{p,k}$ reduced chi square fits for the ferrocene sample, conducted for the photon energy range (index p) of 695 eV to 830 eV in steps of 3.5 eV and the kinetic energy region (index k) of 480 eV to 820 eV in bins of 5 eV. The previously identified kinetic energy regions and photon energy regions associated with DCH processes in iron and oxygen have been outlined and labeled. Indicators for estimated photon energy limits between SCH, resonant DCH and direct DCH processes have been included.

the reconstruction and the kinetic-energy-shifted expected DCH Fe signal (dotted red line). In particular, the Auger-Meitner electron signal extending above the kinetic energy threshold of the SCH $L_{23}M_{45}M_{45}$ region is encapsulated well and matches the expected additional resonance shape. DCH reconstructions similar to FIG. 58 and FIG. 57 are encompassed in FIG. 56 for all photon energies and all kinetic energy bins.

FIG. 59 shows the coefficient map for the sample ferrocene. All regions of Auger-Meitner electron signal associated with iron DCH excitations can be identified in this coefficient map by the strength of the quadratic contribution to the fit, yet the region of overlap between resonantly excited DCH Auger-Meitner electrons of multiply charged iron cations and those resulting from a direct DCH ionization of oxygen is almost entirely absent in this sample. Furthermore, the fits for this sample show a reverse of the coefficient scaling observed in iron pentacarbonyl. The $L_{23}M_{23}M_{23}$ region shows the strongest quadratic coefficient, with regions $L_{23}M_{23}M_{45}$ and $L_{23}M_{45}M_{45}$ showing successively weaker quadratic contributions. This observation holds true for both resonant DCH excitation photon energy range, as well as direct DCH ionization photon energy range. These scaling differences, however, occur over a much smaller range than what was observed for iron pentacarbonyl, where several orders of magnitude separated the coefficients of identifiable regions of interest from the surrounding signal.

The overall strength of the coefficients are in arbitrary units due to the fitting process involved and should therefore not be compared between samples. The relative shift in scaling, in turn, is likely a consequence of the signal ratios between pulse energy measurements. This is largely due to the differing sample delivery methods.

The $L_{23}M_{23}M_{23}$ region is very similar when comparing resonant excitation to direct ionization region in the DCH photon energy regions. The strength of the quadratic contribution is also comparable to the $L_{23}M_{23}M_{45}$ region for both resonant as well as direct excitation. For both, the $L_{23}M_{23}M_{23}$ and $L_{23}M_{23}M_{45}$ kinetic energy region, the coefficient map shows comparable strength in SCH and DCH regions. This is due to the scaling with signal intensity, which is much larger in the SCH resonance.

The same is not true for the $L_{23}M_{45}M_{45}$ region. Both directly ionized and resonantly excited quadratic coefficients are stronger than the respective SCH iron resonance region by an order of magnitude. The oxygen DCH quadratic coefficient is also large in the direct DCH ionization K^2 region. This matches the observations made for the iron pentacarbonyl sample. The region of overlap between the O K^2 and the DCH Auger-Meitner signal from multiply charged iron cations is much smaller than what is observed in iron pentacarbonyl. Additionally, the oxygen SCH Auger-Meitner line shows a particularly strong quadratic contribution in the fit, with the coefficient taking on the strongest measured value at 757 eV. This quadratic contribution is likely due to an overlap with Auger-Meitner electron signal from highly charge iron cations.

9 Conclusion and Outlook

Double core-hole spectroscopy was shown to be a new avenue for spectroscopic investigations of 3d metal complexes with a time resolution matching the lifetime of the iron core-hole of a few fs. DCH spectroscopy experiments were conducted using the 30 fs XFEL pulses of the European XFEL on complex 3d metal molecules. The two samples studied were iron pentacarbonyl (Fe(CO)$_5$) and ferrocene (Fe(C$_5$H$_5$)$_2$), which served as model systems to investigate iron L-edge double core-hole signatures. The two molecules differ both in chemical environment of the iron center, as well as molecular geometry. During measurements with varying pulse energies ranging from approximately 70 µJ to 3.5 mJ, three identifiable iron L-edge double core-hole Auger-Meitner electron signals were resolved, for the $L_{23}M_{23}M_{23}$, $L_{23}M_{23}M_{45}$ and $L_{23}M_{45}M_{45}$ region.

Both eToF and iToF spectra were measured for the photon energy ranges 695 eV to 800 eV and 695 eV to 830 eV, respectively. eToF photon energy scans were repeated for pulse energies between a few 10 µJ to a few mJ. iToF photon energy scans were repeated for pulse energies between a few 100 µJ to a few mJ.

The recorded iToF spectra show that besides the expected cation fragments, a collection of highly charged iron cations is created in the photon-matter interaction. This collection includes highly charged cations of up to Fe^{14+} for iron pentacarbonyl and Fe^{13+} for ferrocene. As the pulse duration is larger than the estimated life-time of the Auger-Meitner process at the iron L-edge, these cations are present in the interaction region and can be sequentially ionized within the duration of the pulse. The varying upper limits for accumulated charge of the two samples were suggested to be results of the fragmentation behavior in the intense X-Ray pulses, as determined by the chemical environment of the samples. It would be of some interest to compare these results to other molecules with Fe center, such as triiron dodecacarbonyl.

For both iron pentacarbonyl and ferrocene, the observed photon energy resonances match the predictions made with an adapted Cowan code Heartree-Fock approach for cation charge states. Charge transfer affected by chemical environment and sample geometry of the two samples are called on as explanation of the differences in observed XAS resonances in the Fe^{1+} product cation channel between this work and those conducted in the single photon regime (see Godehusen et al. [32]). For multiply charged iron cations, a depletion of ion yield was observed that represents very efficient pumping into higher charge states. This observation coincides with measurements of a shifting resonance peak that tends to lower photon energies with higher pulse energies in each charge state. The production pathways for these cations are not dominantly of the form Fe^{n+} $\xrightarrow{-e^{ph}}$ Fe$^{(n+1)+}$ and Fe^{n+} $\xrightarrow{-e^{ph}-e^{AM}}$ Fe$^{(n+2)+}$, but include significant contributions of the form Fe^{n+} $\xrightarrow{-e^{AM}-e^{SCK}-e^{SCK}-e^{AM}}$ Fe$^{(n+4)+}$ following a resonant-resonant DCH excitation and Fe^{n+} $\xrightarrow{-e^{AM}-e^{SCK}-e^{AM}}$ Fe$^{(n+3)+}$ for the photon energy regions corresponding to the resonant DCH L-edge excitation in iron. This mixed production pathway explanation of the observed phenomena is supported by the overlap of the 'bleaching' effect that affects high irradiance measurements in the respective source cations of the DCH production pathways in the corresponding photon energy regions with the relevant product cation resonances. Additional contributions by triple-, or quadruple- ionization were not found to be significant contributors in the two samples, but cannot be discarded as potential

sources of highly charged iron cations. Nevertheless, finding evidence for DCH processes in highly charged iron cations is novel, as it nourishes the interest towards understanding the impact such DCH contributions have on the production pathways in intensely irradiated iron. An analysis of DCH product cation spectra in tandem with DCH electron spectra is not the norm in research of this kind. The results obtained in the experiments conducted for this work may serve as encouragement to incorporate this tandem approach into the planning of further research, particularly where it concerns complex molecules.

The recorded eToF spectra were analyzed with a predominant focus on the iron L-edge Auger-Meitner electron signal. In addition to the traces corresponding to single core-hole excited Auger-Meitner processes in the two samples, Auger-Meitner electrons stemming from the $L_{23}M_{45}M_{45}$ transition in the resonantly double core-hole excited sample were detected. Their detection was facilitated by a Cowan code model of a double core-hole Auger-Meitner relaxation process and the postulation that while the Auger-Meitner electrons of multiply charged iron cations tend toward lower kinetic energies than those emitted by the neutral iron atom, the Auger-Meitner electrons of a double core-hole excited iron atom are found at higher kinetic energies than those of the neutral iron atom. The double core-hole characteristics of these Auger-Meitner electrons were confirmed by a quadratic fit conducted for the signal over the range of utilized pulse energies, which, with constant pulse duration, increases the irradiance of the sample, revealing the quadratic scaling of signal intensity with irradiance inherent in double core-hole processes. Using the $L_{23}M_{45}M_{45}$ DCH signal, the photon energy region of the double core-hole resonance was identified.

It was found that the expected DCH signatures of the $L_{23}M_{23}M_{23}$ and $L_{23}M_{23}M_{45}$ Auger-Meitner electrons are found at similar kinetic energy regions as the SCH and DCH electrons of multiply charged iron cations. The faster $L_{23}M_{23}M_{23}$ electrons emitted by the DCH excitations in the samples, for example, were detected at similar kinetic energies as the SCH $L_{23}M_{23}M_{45}$ Auger-Meitner electrons emitted by ionization of charge states Fe^{n+}, with $n = 4 : 6$. These superpositions of DCH and SCH Auger-Meitner electrons in the time-of-flight channels had to be disentangled to access DCH electron signatures in these kinetic regions.

By using the results of the iToF measurements as approximations of the interaction region conditions in terms of present iron cations, a disentanglement of the SCH and DCH contributions was conducted. These efforts were rooted in and compared to the results of SCH Auger-Meitner model results from the Cowan code Heartree Fock model, an adapted version capable of accurately modeling not only the expected photon energy region of DCH resonance, but also the energies of Auger-Meitner electrons emitted from neutral, as well as singly- and multiply-charged iron cations. They were used as reference and an approximate Auger-Meitner electron signal combination, corresponding to the cation charge states detected at each pulse energy, scaled by the relative prevalence of each cation signature in the iToF spectrum was created. This approximation was compared to the eToF signatures, which revealed a small section of the $L_{23}M_{23}M_{45}$ region that showed a predominantly DCH Auger-Meitner electron signature.

The disentanglement efforts yielded kinetic- and photon-energy regions of quadratic scaling with irradiance that can be matched to the $L_{23}M_{23}M_{23}$, $L_{23}M_{23}M_{45}$ and $L_{23}M_{45}M_{45}$ signatures of both resonant, as well as direct ionization in both samples. In the two samples studied here, the three Auger-Meitner electron regions showed vastly different DCH impact, with the $L_{23}M_{45}M_{45}$ region being favored in the DCH relaxation of iron pentacarbonyl and the

$L_{23}M_{23}M_{23}$ region appearing stronger for DCH relaxation in ferrocene. These differing results show that L-edge double core-hole spectroscopy offers a multitude of perspectives from which to study the fs dynamics of $3d$ metal complexes.

One such perspective was investigated in the DCH signatures of direct ionization in carbon monoxide and atomic oxygen. For iron pentacarbonyl, the chemical environment included carbon monoxide ligands, whose KVV DCH Auger-Meitner electron signature could be identified and measured with a comparable scaling to what was found for the iron L-edge Auger-Meitner electrons. In ferrocene, ambient water pressure in the chamber provided enough signal to trace the KVV DCH Auger-Meitner electron signal as well and a match to the kinetic energy of K^2 DCH ionized water was found. The two DCH features were directly compared and showed different kinetic energies, as well as vastly different feature form. For the study of $3d$ metal complexes, this entails that oxygen ligands in the chemical environment can be investigated in tandem to the metal centers. This DCH sensitivity to the chemical environment enables access to the same time frame of a few fs that was achieved for the iron center of the $3d$ metal complexes studied here. Further experiments using this method will likely contribute much to the understanding of charge migration between oxygen ligands and metal centers in other complex molecules of biochemical interest.

This thesis shows the power of L-edge DCH spectroscopy to provide the aspired fs timescale access to the investigation of $3d$ metal complexes in resolving the DCH Auger-Meitner electron signal of both samples. Achieving this with the 30 fs pulse duration provided for the experiments of this thesis and not only disentangling the SCH from DCH contributions, but rather incorporating this data into the understanding of the photon-matter interaction between intense X-Rays and $3d$ metal complexes, opens up further possibilities in DCH spectroscopic studies. With the first attosecond pulses having been announced at the European XFEL during the writing of this work, DCH spectroscopic pump-probe studies with an attosecond time-resolution are realistic future prospects for such projects. Furthermore, the complexity of the molecules investigated with this technique implies that different and perhaps larger $3d$ metal complexes are accessible for DCH spectroscopy. With the ever-shortening pulse duration that can be provided at facilities such as the European XFEL, this could entail future attosecond pump-probe DCH spectroscopy on these systems.

10 List of Papers

During my PhD time I played a significant role in preparing and conducting the experiments as well as taking part in the data analysis and interpretation for the following papers:

- Martins, M., Reinwardt, S., Schunck, J. O., Schwarz, J., Baev, K., Müller, A., Buhr, T., Perry-Sassmannshausen, A., Klumpp, S., Schippers, S. *Disentangling the Photodissociation Dynamics of the HF$^+$ Molecular Radical via Kinetic-Energy-Release-Resolved F 1s Core Excitation and Ionization*, The Journal of Physical Chemistry Letters, 12, 1390, doi: 10.1021/acs.jpclett.0c03, 2021

- Junghoefer, T., Calzolari, A., Baev, I., Glaser, M., Ciccullo, F., Giangrisostomi, E., Ovsyannikov, R., Kielgast, F., Nissen, M., Schwarz, J., Gallagher N. M., Rajca, A., Martins, M., Casu, M. B. *Magnetic behavior in metal-free radical thin films*, Chem, 8, 801, doi: 10.1016/j.chempr.2021.11., 2022

- Schwarz, J., Kielgast, F., Baev, I., Reinwardt, S., Trinter, F., Klumpp, S., Perry-Sassmannshausen, A., Buhr, T., Schippers, S., Müller, A., Bari, S., Mondes, V., Flesch, R., Rühl, E., Martins, M. *X-Ray absorption spectroscopy of H_3O^+*, Phys. Chem. Chem. Phys., 24, 23119, doi: 10.1039/D2CP02383K, 2022

Acknowledgement

Appendix

This appendix includes the coefficient maps of the $y_{p,k} = a_{p,k}x^2 + b_{p,k}x + c_{p,k}$ reduced chi square fits coefficients $b_{p,k}$ and $c_{p,k}$ for the samples ferrocene and iron pentacarbonyl. These coefficient maps were created in the manner detailed in Section 8, by re-binning the kinetic energy region over the index k in steps of $5\,\text{eV}$ and applying a quadratic fit $y_{p,k} = a_{p,k}x^2 + b_{p,k}x + c_{p,k}$ over the available pulse energy range for each kinetic energy bin k and each photon energy step p, resulting in coefficients for each p-k-bin.
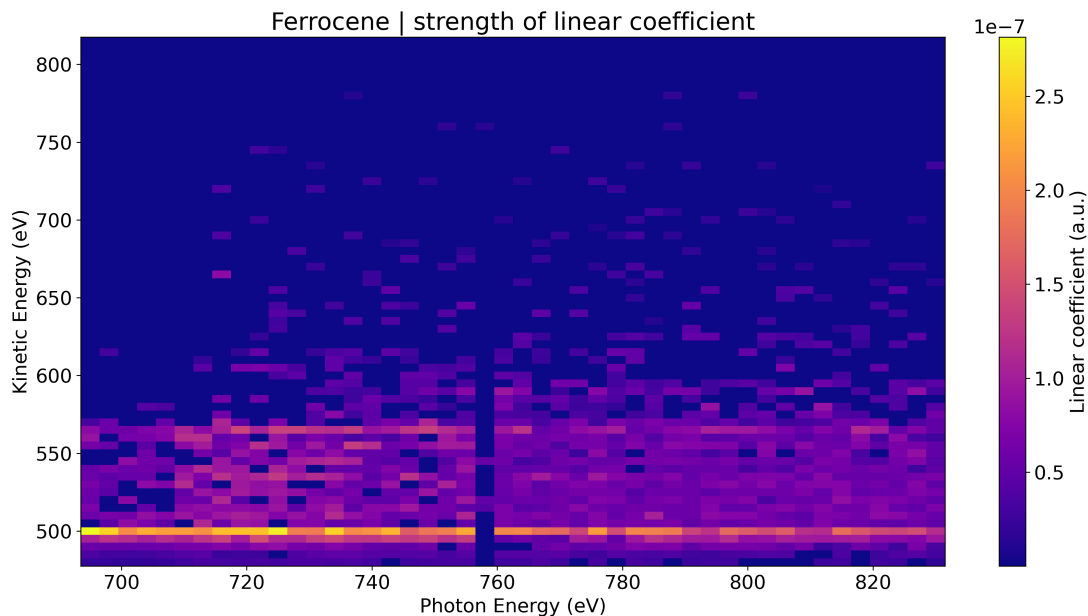
Figure 60: A coefficient map of the linear coefficient $b_{p,k}$ in the collection of $y_{p,k} = a_{p,k}x^2 + b_{p,k}x + c_{p,k}$ reduced chi square fits for the ferrocene sample, conducted for the photon energy range (index p) of 695 eV to 830 eV in steps of 3.5 eV and the kinetic energy region (index k) of 480 eV to 820 eV in bins of 5 eV.
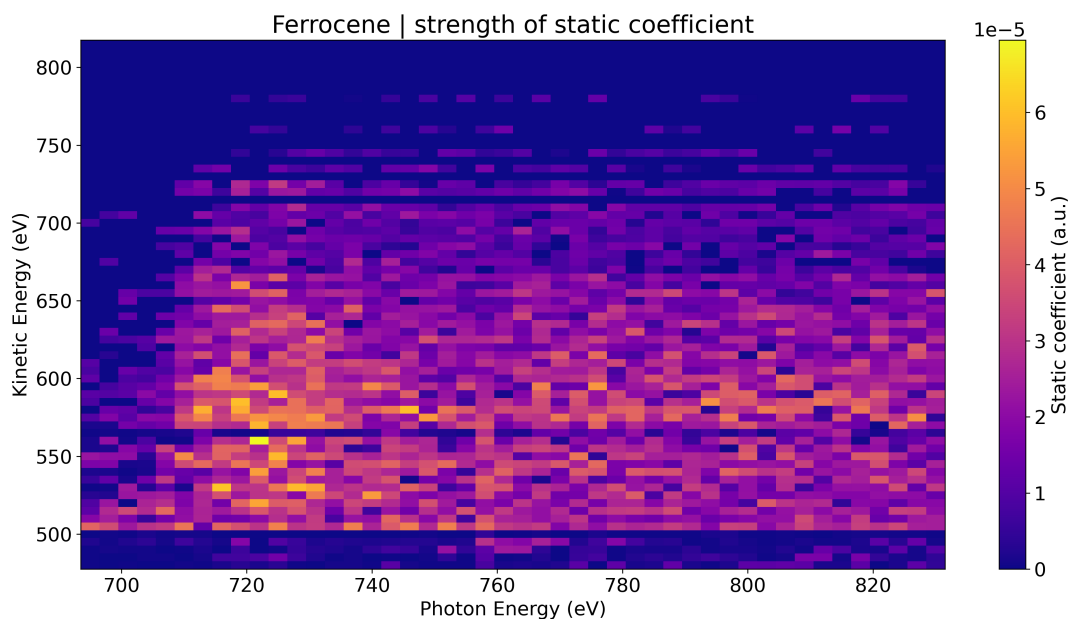

Figure 61: A coefficient map of the static coefficient $c_{p,k}$ in the collection of $y_{p,k} = a_{p,k}x^2 + b_{p,k}x + c_{p,k}$ reduced chi square fits for the ferrocene sample, conducted for the photon energy range (index p) of 695 eV to 830 eV in steps of 3.5 eV and the kinetic energy region (index k) of 480 eV to 820 eV in bins of 5 eV.
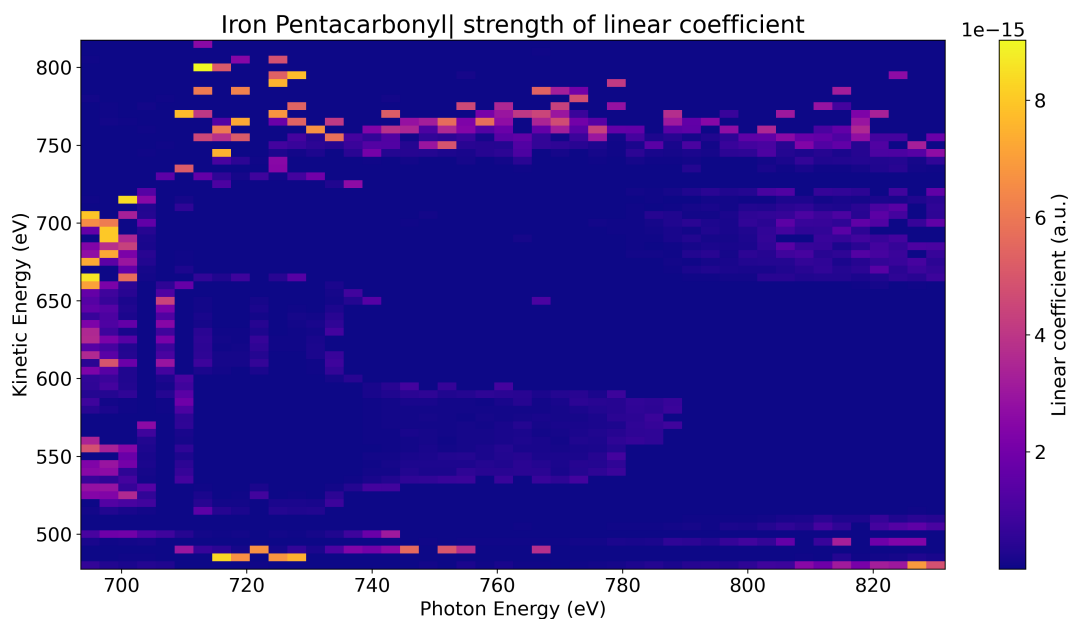
Figure 62: A coefficient map of the linear coefficient $b_{p,k}$ in the collection of $y_{p,k} = a_{p,k}x^2 + b_{p,k}x + c_{p,k}$ reduced chi square fits for the iron pentacarbonyl sample, conducted for the photon energy range (index p) of 695 eV to 830 eV in steps of 3.5 eV and the kinetic energy region (index k) of 480 eV to 820 eV in bins of 5 eV.
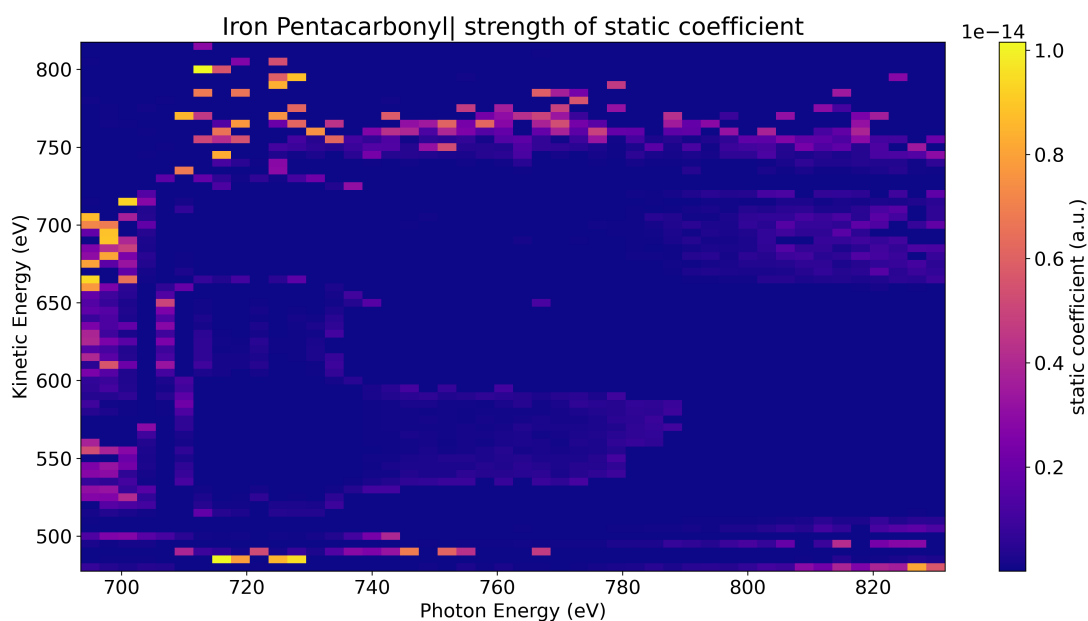

Figure 63: A coefficient map of the static coefficient $c_{p,k}$ in the collection of $y_{p,k} = a_{p,k}x^2 + b_{p,k}x + c_{p,k}$ reduced chi square fits for the iron pentacarbonyl sample, conducted for the photon energy range (index p) of 695 eV to 830 eV in steps of 3.5 eV and the kinetic energy region (index k) of 480 eV to 820 eV in bins of 5 eV.

126

Eidesstattliche Versicherung / Declaration on oath

Hiermit versichere ich an Eides statt, die vorliegende Dissertationsschrift selbst verfasst und keine anderen als die angegebenen Hilfsmittel und Quellen benutzt zu haben.

Sofern im Zuge der Erstellung der vorliegenden Dissertationsschrift generative Künstliche Intelligenz (gKI) basierte elektronische Hilfsmittel verwendet wurden, versichere ich, dass meine eigene Leistung im Vordergrund stand und dass eine vollständige Dokumentation aller verwendeten Hilfsmittel gemäß der Guten wissenschaftlichen Praxis vorliegt. Ich trage die Verantwortung für eventuell durch die gKI generierte fehlerhafte oder verzerrte Inhalte, fehlerhafte Referenzen, Verstöße gegen das Datenschutz- und Urheberrecht oder Plagiate.

Hamburg, den ___06-06-2024___

Unterschrift der Doktorandin / des Doktoranden

References

[1] Ackermann, W., Asova, G., Ayvazyan, V., et al. 2007, 1, 336, doi: `10.1038/nphoton.2007.76`

[2] Allen, G. C., Tucker, P. M., & Wild, R. K. 1977, Surface Science, 68, 469, doi: `10.1016/0039-6028(77)90240-0`

[3] Almbladh, C.-O., Morales, A. L., & Grossmann, G. 1989, Physical Review B, 39, 3489, doi: `10.1103/PhysRevB.39.3489`

[4] Antonio Bonucci. 2018, XFEL: Third light source generates first X-ray light. `https://www.xfel.eu/news_and_events/news/index_eng.html?openDirectAnchor=1536`

[5] Auger, P. 1925, Journal de Physique et le Radium, 6, 205, doi: `10.1051/jphysrad:0192500606020500`

[6] Barca, G. M. J., Bertoni, C., Carrington, L., et al. 2020, The Journal of Chemical Physics, 152, 154102, doi: `10.1063/5.0005188`

[7] Bartlett, R. J., & Stanton, J. F. 1994, in Reviews in Computational Chemistry, 1st edn., ed. K. B. Lipkowitz & D. B. Boyd, Vol. 5 (Wiley), 65–169, doi: `10.1002/9780470125823.ch2`

[8] Baumann, T. M., Boll, R., De Fanis, A., et al. 2023, Journal of Synchrotron Radiation, 30, 662, doi: `10.1107/S1600577523003090`

[9] Beerwerth, R., Buhr, T., Perry-Sassmannshausen, A., et al. 2019, The Astrophysical Journal, 887, 189, doi: `10.3847/1538-4357/ab5118`

[10] Blancard, C., Cubaynes, D., Guilbaud, S., & Bizau, J.-M. 2018, The Astrophysical Journal, 853, 32, doi: `10.3847/1538-4357/aa9ff7`

[11] Bohn, R. K., & Haaland, A. 1966, 5, 470, doi: `10.1016/S0022-328X(00)82382-7`

[12] Bonch-Bruevich, A. M., & Khodovoǐ, V. A. 1965, Soviet Physics Uspekhi, 8, 1, doi: `10.1070/PU1965v008n01ABEH003060`

[13] Brais, C. J., Ibañez, J. O., Schwartz, A. J., & Ray, S. J. 2021, Mass Spectrometry Reviews, 40, 647, doi: `10.1002/mas.21650`

[14] Bressler, C., & Chergui, M. 2004, Chemical Reviews, 104, 1781, doi: `10.1021/cr0206667`

[15] Caldwell, C. D., & Krause, M. O. 1993, Physical Review A, 47, R759, doi: `10.1103/PhysRevA.47.R759`

[16] Cardona, M., & Ley, L., eds. 1978, Topics in Applied Physics, Vol. 26, Photoemission in Solids I (Berlin, Heidelberg: Springer), doi: `10.1007/3-540-08685-4`

[17] Cederbaum, L. S., Tarantelli, F., Sgamellotti, A., & Schirmer, J. 1986, The Journal of Chemical Physics, 85, 6513, doi: 10.1063/1.451432

[18] Coriani, S., Haaland, A., Helgaker, T., & Jørgensen, P. 2006, ChemPhysChem, 7, 245, doi: 10.1002/cphc.200500339

[19] Coster, D., & L. Kronig, R. D. 1935, Physica, 2, 13, doi: 10.1016/S0031-8914(35)90060-X

[20] Cowan, R. D. 1981, The Theory of Atomic Structure and Spectra, 1st edn. No. 3 (Berkeley: University of California Press). https://www.ucpress.edu/book/9780520038219/the-theory-of-atomic-structure-and-spectra

[21] Czwalinna, M., Boll, R., Kirkwood, H., et al. 2021, Proceedings of the 12th International Particle Accelerator Conference, IPAC2021, 6 pages, 0.921 MB, doi: 10.18429/JACOW-IPAC2021-THXB02

[22] De Fanis, A., Ilchen, M., Achner, A., et al. 2022, Journal of Synchrotron Radiation, 29, 755, doi: 10.1107/S1600577522002284

[23] Dirac, P. A. M., & Fowler, R. H. 1997, Proceedings of the Royal Society of London. Series A, Containing Papers of a Mathematical and Physical Character, 114, 710, doi: 10.1098/rspa.1927.0071

[24] —. 1997, Proceedings of the Royal Society of London. Series A, Containing Papers of a Mathematical and Physical Character, 117, 610, doi: 10.1098/rspa.1928.0023

[25] —. 1997, Proceedings of the Royal Society of London. Series A, Containing Papers of a Mathematical and Physical Character, 113, 621, doi: 10.1098/rspa.1927.0012

[26] Dommach, M., Di Felice, M., Dickert, B., et al. 2021, Journal of Synchrotron Radiation, 28, 1229, doi: 10.1107/S1600577521005154

[27] European X-Ray Free-Electron Laser Facility GmbH. 2023, AQS end station. https://www.xfel.eu/facility/instruments/sqs/instrument/aqs_end_station/index_eng.html

[28] Fang, L., Hoener, M., Gessner, O., et al. 2010, Physical Review Letters, 105, 083005, doi: 10.1103/PhysRevLett.105.083005

[29] Fangohr, H., Beg, M., Bondar, V., et al. 2017. https://eprints.soton.ac.uk/425097/

[30] Fortes, A. D., & Parker, S. F. 2022, 144, 17376, doi: 10.1021/jacs.2c01469

[31] Gerken, N., Klumpp, S., Sorokin, A., et al. 2014, Physical Review Letters, 112, 213002, doi: 10.1103/PhysRevLett.112.213002

[32] Godehusen, K., Richter, T., Zimmermann, P., & Wernet, P. 2017, The Journal of Physical Chemistry A, 121, 66, doi: `10.1021/acs.jpca.6b10399`

[33] Grychtol, P., Rivas, D. E., Baumann, T. M., et al. 2021, Optics Express, 29, 37429, doi: `10.1364/OE.440718`

[34] Guerrero, R. V., ed. 2014, The Gas Attenuator Instrument for SASE3 Soft X-Ray Beamline at the European XFEL. `https://xfel.tind.io/record/1763`

[35] Hartree, D. R. 1928, Mathematical Proceedings of the Cambridge Philosophical Society, 24, 89, doi: `10.1017/S0305004100011919`

[36] Hemmers, O., Whitfield, S. B., Glans, P., et al. 1998, Review of Scientific Instruments, 69, 3809, doi: `10.1063/1.1149183`

[37] Hjelte, I., Piancastelli, M., Fink, R., et al. 2001, Chemical Physics Letters, 334, 151, doi: `https://doi.org/10.1016/S0009-2614(00)01434-2`

[38] J. Atkins, A., Bauer, M., & R. Jacob, C. 2015, Physical Chemistry Chemical Physics, 17, 13937, doi: `10.1039/C5CP01045D`

[39] Kessissoglou, D. P., ed. 1995, Bioinorganic Chemistry (Dordrecht: Springer Netherlands), doi: `10.1007/978-94-011-0255-1`

[40] Khubbutdinov, R., Gerasimova, N., Mercurio, G., et al. 2021, Structural Dynamics, 8, 044305, doi: `10.1063/4.0000127`

[41] Koel, B. E., White, J. M., & Loubriel, G. M. 1982, The Journal of Chemical Physics, 77, 2665, doi: `10.1063/1.444092`

[42] Koulentianos, D. 2019, Double Inner-Shell Vacancies in Molecules. `https://gupea.ub.gu.se/handle/2077/59862`

[43] Koulentianos, D., Fouda, A. E. A., Southworth, S. H., et al. 2020, Journal of Physics B: Atomic, Molecular and Optical Physics, 53, 244005, doi: `10.1088/1361-6455/abc183`

[44] Koulentianos, D., Carravetta, V., Couto, R. C., et al. 2022, The Journal of Chemical Physics, 157, 044306, doi: `10.1063/1.5135388`

[45] Kramida, A. 2019, Atoms, 7, 64, doi: `10.3390/atoms7030064`

[46] Kraus, P. M., Zürch, M., Cushing, S. K., Neumark, D. M., & Leone, S. R. 2018, Nature Reviews Chemistry, 2, 82, doi: `10.1038/s41570-018-0008-8`

[47] Krausz, F. 2001, Physics World, 14, 41, doi: `10.1088/2058-7058/14/9/31`

[48] Kubin, M., Guo, M., Kroll, T., et al. 2018, Chemical Science, 9, 6813, doi: `10.1039/C8SC00550H`

[49] Kučas, S., Drabužinskis, P., & Jonauskas, V. 2020, Atomic Data and Nuclear Data Tables, 135-136, 101357, doi: 10.1016/j.adt.2020.101357

[50] Lablanquie, P., Andric, L., Palaudoux, J., et al. 2007, Journal of Electron Spectroscopy and Related Phenomena, 156-158, 51, doi: 10.1016/j.elspec.2006.11.062

[51] LaForge, A. C., Son, S.-K., Mishra, D., et al. 2021, Physical Review Letters, 127, 213202, doi: 10.1103/PhysRevLett.127.213202

[52] Linusson, P., Takahashi, O., Ueda, K., Eland, J. H. D., & Feifel, R. 2011, Physical Review A, 83, 022506, doi: 10.1103/PhysRevA.83.022506

[53] Maltezopoulos, T., Dietrich, F., Freund, W., et al. 2019, Journal of Synchrotron Radiation, 26, 1045, doi: 10.1107/S1600577519003795

[54] Marchenko, T., Inhester, L., Goldsztejn, G., et al. 2018, Physical Review A, 98, 063403, doi: 10.1103/PhysRevA.98.063403

[55] Martins, M. 2001, Journal of Physics B: Atomic, Molecular and Optical Physics, 34, 1321, doi: 10.1088/0953-4075/34/7/313

[56] —. 2002, Journal of Physics B: Atomic, Molecular and Optical Physics, 35, L223, doi: 10.1088/0953-4075/35/11/101

[57] Martins, M., Godehusen, K., Richter, T., Wernet, P., & Zimmermann, P. 2006, Journal of Physics B: Atomic, Molecular and Optical Physics, 39, R79, doi: 10.1088/0953-4075/39/5/R01

[58] Mazza, T., Signorato, R., Meyer, M., et al. 2014, in Adaptive X-Ray Optics III, Vol. 9208 (SPIE), 9–23, doi: 10.1117/12.2060859

[59] Mazza, T., Zhang, H., & Meyer, M. 2012, doi: 10.3204/XFEL.EU/TR-2012-007

[60] Mazza, T., Ilchen, M., Kiselev, M., et al. 2020, Physical Review X, 10, 041056, doi: 10.1103/PhysRevX.10.041056

[61] Mazza, T., Baumann, T. M., Boll, R., et al. 2023, Journal of Synchrotron Radiation, 30, 457, doi: 10.1107/S1600577522012085

[62] McGuinness, C., Martins, M., Wernet, P., et al. 1999, Journal of Physics B: Atomic, Molecular and Optical Physics, 32, L583, doi: 10.1088/0953-4075/32/20/103

[63] McGuire, E. J. 1972, Physical Review A, 5, 1043, doi: 10.1103/PhysRevA.5.1043

[64] Meitner, L. 1922, Zeitschrift für Physik, 9, 131, doi: 10.1007/BF01326962

[65] Mertens, K. 2020, Ultrafast electron redistribution in small iodine containing molecules, dissertation universität hamburg edn. (Hamburg: Verlag Dr. Hut)

[66] Meyer, M., Baumann, T. M., Achner, A., et al. 2020, Journal of Physics: Conference Series, 1412, 112005, doi: 10.1088/1742-6596/1412/11/112005

[67] Moreschini, L., Ghiringhelli, G., Larsson, K., Veit, U., & Brookes, N. B. 2008, Review of Scientific Instruments, 79, 033905, doi: 10.1063/1.2868781

[68] Mucke, M., Zhaunerchyk, V., Frasinski, L. J., et al. 2015, New Journal of Physics, 17, 073002, doi: 10.1088/1367-2630/17/7/073002

[69] Mårtensson, N., Baltzer, P., Brühwiler, P. A., et al. 1994, Journal of Electron Spectroscopy and Related Phenomena, 70, 117, doi: 10.1016/0368-2048(94)02224-N

[70] Nagler, B., Zastrau, U., Fäustlin, R. R., et al. 2009, Nature Physics, 5, 693, doi: 10.1038/nphys1341

[71] Nyholm, R., Martensson, N., Lebugle, A., & Axelsson, U. 1981, Journal of Physics F: Metal Physics, 11, 1727, doi: 10.1088/0305-4608/11/8/025

[72] Oberli, S. 2019, PhD thesis. https://theses.hal.science/tel-02078799

[73] Piancastelli, M. N. 2013, The European Physical Journal Special Topics, 222, 2035, doi: 10.1140/epjst/e2013-01985-9

[74] Robinson, H., & Rutherford, E. 1997, Proceedings of the Royal Society of London. Series A, Containing Papers of a Mathematical and Physical Character, 104, 455, doi: 10.1098/rspa.1923.0121

[75] Rudek, B., Son, S.-K., Foucar, L., et al. 2012, Nature Photonics, 6, 858, doi: 10.1038/nphoton.2012.261

[76] Rörig, A., Son, S.-K., Mazza, T., et al. 2023, Nature Communications, 14, 5738, doi: 10.1038/s41467-023-41505-1

[77] Saldin, E. L., Schneidmiller, E. A., & Yurkov, M. V. 2000, The Physics of Free Electron Lasers (Berlin, Heidelberg: Springer Berlin Heidelberg)

[78] Salzner, U. 2013, Journal of Chemical Theory and Computation, 9, 4064, doi: 10.1021/ct400322v

[79] Santra, R., Kryzhevoi, N. V., & Cederbaum, L. S. 2009, Physical Review Letters, 103, 013002, doi: 10.1103/PhysRevLett.103.013002

[80] Schippers, S., Martins, M., Beerwerth, R., et al. 2017, The Astrophysical Journal, 849, 5, doi: 10.3847/1538-4357/aa8fcc

[81] Schippers, S., Beerwerth, R., Bari, S., et al. 2021, The Astrophysical Journal, 908, 52, doi: 10.3847/1538-4357/abcc64

[82] Serkez, S., Decking, W., Fröhlich, L., et al. 2019, Proceedings of the 39th Free Electron Laser Conference, FEL2019, 4 pages, 0.528 MB, doi: `10.18429/JACOW-FEL2019-TUP062`

[83] Sherrill, C. D. 2000, An Introduction to Hartree-Fock Molecular Orbital Theory, Georgia Institute of Technology. `http://vergil.chemistry.gatech.edu/notes/hf-intro/hf-intro.pdf`

[84] Siegbahn, K. 1985, Journal of Electron Spectroscopy and Related Phenomena, 36, 113, doi: `10.1016/0368-2048(85)80013-X`

[85] Sigma-Aldrich. 2023, Eisen(0)-pentacarbonyl >99.99% trace metals basis | Sigma-Aldrich. `http://www.sigmaaldrich.com/`

[86] —. 2023, Ferrocen 98% | Sigma-Aldrich. `http://www.sigmaaldrich.com/`

[87] Singer, W., Singer, X., Brinkmann, A., et al. 2015, Superconductor Science and Technology, 28, 085014, doi: `10.1088/0953-2048/28/8/085014`

[88] Slater, J. C. 1928, Physical Review, 32, 339, doi: `10.1103/PhysRev.32.339`

[89] Sorokin, A. A., Bobashev, S. V., Feigl, T., et al. 2007, Physical Review Letters, 99, 213002, doi: `10.1103/PhysRevLett.99.213002`

[90] Sorokin, A. A., Bican, Y., Bonfigt, S., et al. 2019, Journal of Synchrotron Radiation, 26, 1092, doi: `10.1107/S1600577519005174`

[91] Stucky, G. D., Rye, R. R., Jennison, D. R., & Kelber, J. A. 1982, Journal of the American Chemical Society, 104, 5951–5959, doi: `10.1021/ja00386a020`

[92] Tschentscher, T., Bressler, C., Grünert, J., et al. 2017, Applied Sciences, 7, 592, doi: `10.3390/app7060592`

[93] Ueda, K. 2018, Applied Sciences, 8, 879, doi: `10.3390/app8060879`

[94] Ungier, L., & Thomas, T. D. 1985, The Journal of Chemical Physics, 82, 3146, doi: `10.1063/1.448212`

[95] Walker, D. J., Barty, C. P. J., Yin, G. Y., Young, J. F., & Harris, S. E. 1987, Optics Letters, 12, 894, doi: `10.1364/OL.12.000894`

[96] Weise, H., & Decking, W. 2018, Proceedings of the 38th Int. Free Electron Laser Conf., FEL2017, 5 pages, 1.953 MB, doi: `10.18429/JACOW-FEL2017-MOC03`

[97] Wiesli, R. A., Beard, B. L., Braterman, P. S., et al. 2007, Talanta, 71, 90, doi: `10.1016/j.talanta.2006.03.026`

[98] Wiley, W. C., & McLaren, I. H. 2004, Review of Scientific Instruments, 26, 1150, doi: `10.1063/1.1715212`

[99] Wolff, M. M., & Stephens, W. E. 2004, Review of Scientific Instruments, 24, 616, doi: 10.1063/1.1770801

[100] Wrackmeyer, B., Tok, O. L., & Herberhold, M. 2001, Organometallics, 20, 5774, doi: 10.1021/om010756m

[101] Yeh, J. J., & Lindau, I. 1985, Atomic Data and Nuclear Data Tables, 32, 1, doi: 10.1016/0092-640X(85)90016-6

[102] Young, L., Ueda, K., Gühr, M., et al. 2018, Journal of Physics B: Atomic, Molecular and Optical Physics, 51, 032003, doi: 10.1088/1361-6455/aa9735

[103] Zewail, A. H. 2000, The Journal of Physical Chemistry A, 104, 5660, doi: 10.1021/jp001460h

[104] —. 2001, Angewandte Chemie, 113, 4501, doi: 10.1002/1521-3757(20011203)113:23<4501::AID-ANGE4501>3.0.CO;2-1

[105] Zhaunerchyk, V., Kamińska, M., Mucke, M., et al. 2015, Journal of Physics B: Atomic, Molecular and Optical Physics, 48, 244003, doi: 10.1088/0953-4075/48/24/244003